Department of Physics and Astronomy

Heidelberg University

Master thesis

in Physics

submitted by

Moto Togawa

born in Düsseldorf

2021

Investigation of the M-shell unresolved transition array of aluminium-like iron using monochromatic soft x-ray synchrotron radiation

This Master thesis has been carried out by Moto Togawa

at the

Max Planck Institute for Nuclear Physics

under the supervision of

Apl. Prof. Dr. José R. Crespo López-Urrutia

Second examiner:

Prof. Dr. Klaus Blaum

Abstract

In various astrophysical observations, the $n = 2 \rightarrow 3$ transitions of highly charged iron appear in the soft x-ray region as an unresolved transition array (UTA). The structure of the UTA is directly related to the ionization balance of the plasma and is therefore of high astrophysical interest. The models used to analyse the astrophysical spectra are highly sensitive to the input atomic data, which is mainly based on theoretical calculations. Therefore high precision laboratory measurements are needed for benchmarking theory.

Within this thesis, a systematic measurement over the whole UTA energy range has been conducted to determine the transition energies and rates for the thirteen-fold ionized iron (Fe^{13+}), an important constituent of the UTA. The ions of interest were produced by an electron beam ion trap and resonantly excited by the synchrotron radiation of PETRA III. By utilizing an ion-extraction beamline, the radiative as well as the autoionization decay channels have been observed in parallel. 31 hitherto unexplored transitions of the UTA have been resolved with a relative accuracy on the level of 40 parts-per million, serveral orders of magnitude higher than the accuracy obtained in the astrophysical observations. An additional high resolution measurement lead to the extraction of the natural linewidth, which has been used to determine the absolute radiative and autoionization rates of two prominent lines of the UTA. A comparison with state-of-the-art theory revealed a significant $80(7)\,\mathrm{meV}$ offset in transition energies as well as a three to four-fold smaller natural linewidth, leading to the question how reliable the astrophysical models are.

Kurzzusammenfassung

In verschiedenen astrophysikalischen Beobachtungen erscheinen die $n = 2 \rightarrow 3$ Übergänge von hochgeladenem Eisen im weichen Röntgenbereich als unaufgelöstes Übergangsfeld (engl. unresolved transition array, UTA). Die Struktur des UTA steht in direktem Zusammenhang mit der Ionisationsstruktur des Plasmas und ist daher astrophysikalisch von hohem Interesse. Da die Modelle, die zur Analyse der astrophysikalischen Spektren verwendet werden, sehr empfindlich auf die Atomstrukturdaten , welche hauptsächlich aus theoretischen Berechnungen bestehen, reagieren, sind hochpräzise Labormessungen zur Überprüfung der Theorie erforderlich.

Im Rahmen dieser Arbeit wurde eine systematische Messung über den gesamten UTA-Energiebereich durchgeführt, um die Übergangsenergien und Übergangsraten für das dreizehnfach ionisierte Fe^{13+}, einen wichtigen Bestandteil des UTA, zu bestimmen. Die Ionen wurden von einer Elektronenstrahl-Ionenfalle produziert und durch die Synchrotronstrahlung von PETRA III resonant angeregt. Durch die Verwendung einer Ionen-Extraktionsstrahlführung wurden sowohl die Radiativen- als auch die Autoionisationszerfallskanäle parallel beobachtet. 31 Übergänge der UTA wurden mit einer relativen Genauigkeit von 40 ppm aufgelöst, mehrere Größenordnungen besser als die Genauigkeit der astrophysikalischen Beobachtungen. Eine zusätzliche hochauflösende Messung ermöglichte die Bestimmung der natürlichen Linienbreite, die zur Bestimmung der absoluten Radiativen- und Autoionisationsraten von zwei starken Linien des UTA verwendet wurde. Ein Vergleich mit der aktuellen Theorie ergab einen signifikanten $80(7)\,\mathrm{meV}$-Offset der Übergangsenergien sowie eine drei- bis viermal kleinere natürliche Linienbreite, wodurch die Zuverlässigkeit der astrophysikalischen Modelle in Frage gestellt wird.

Contents

1 Introduction

Spectroscopy is the analysis of the interaction between electromagnetic waves and matter such as atoms or ions. It is the most important way to study the interaction of light and matter. Each element exhibits an unique spectroscopic fingerprint and thus enables insights into the internal structure of atoms by observation of the specific emitted or absorbed wavelengths.

One of the most historically educational experiments is the observation of the spectrum of the sun. In general it can be modelled as a continuous black body spectrum with an effective temperature of $5780\,\mathrm{K}$. Detailed analysis of the solar spectrum however reveals distinct dark lines in the aforementioned continuous spectrum. First systematic studies were conducted by Joseph von Fraunhofer in 1814 . In his analysis, more than 570 lines were identified, now known as the Fraunhofer lines [1]. The most principal lines were labelled with capital letters A to K. The origin of the Fraunhofer lines remained unexplained until half a century later Kirchhoff and Bunsen discovered that the characteristic features in the sun's spectrum coincide with emission lines of various elements. They concluded that for example the nowadays well known „D-line"in the solar spectrum is caused by the absorption of light by sodium [2].

Just like that spectroscopy has proven countless times in history to be a fundamental tool for the analysis of matter. The Fraunhofer lines are assigned to the optical region of the electromagnetic spectrum. These lines originate, just like the D-line, from lowly ionized elements residing in the relatively cold outer sphere of the sun. Due to the much higher inner temperature of the sun, most lighter elements are stripped all of their bound electrons and are thus unable to emit or absorb light. Heavier elements can keep some of their inner electrons because of the quadratic scaling law of the binding energy. These systems are called highly charged ions [3]. The absorption lines of intershell transitions produced by highly charged ions are usually in the soft x-ray regime or even higher in energy.

Unfortunately the absorption properties of the atmosphere make earth based observations of radiation outside the optical spectral region inaccessible. However with the advent of satellite-based space observatories equipped with spectrometers combined with charged-coupled-devices, the hence unavailable spectral region has become accessible for studies. NASA's flagship mission CHANDRA and ESA's XMM-Newton, which have been launched in the late 90s, are still providing valuable spectra today [4, 5, 6].

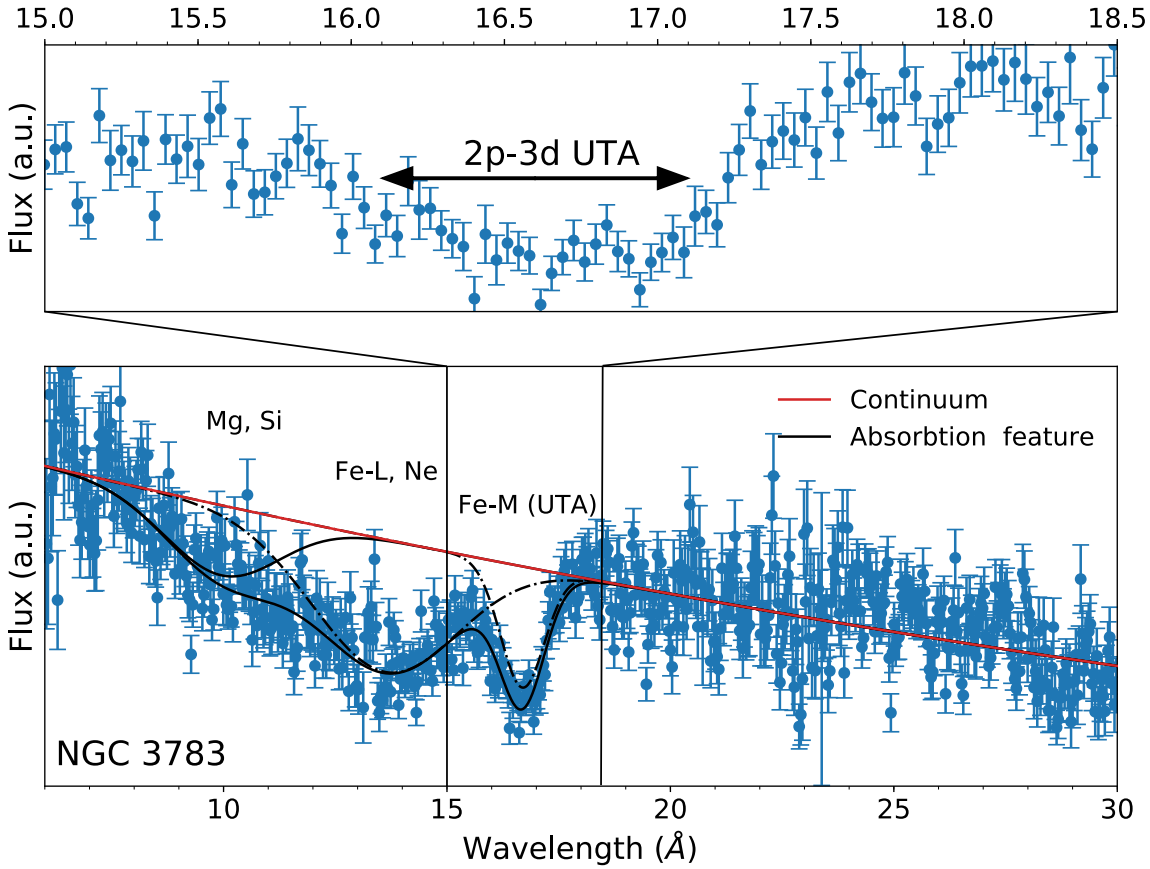

Figure 1: Absorption spectra obtained with the RGS of XMM-Newton (blue dots), with the modeled power-law continuum (red) and power-law plus absorption feature superimposed (black solid). The absorption feature in the center of the spectrum belongs to the M-shell UTA of iron. Signatures of other elements such as Mg and Si can also be seen. A more detailed analysis can be found here [7]. Raw data from [8].

One of the astrophysically most relevant elements is iron. It is a highly abundant element in the universe and therefore often found in extraterrestrial plasma [9]. Due to its relatively high atomic number, iron is present in several charge states in low as well as in high temperature plasma. Prominent spectral lines like K_α and K_β or the controversial $3C$ and $3D$ lines can be used as diagnostics [10, 11, 12]. The $3C$ and $3D$-lines are $n = 2 \longrightarrow 3$ transitions and originate from the Ne-like iron ion Fe^{16+}. Since the involved electrons are valence electrons, $3C$ and $3D$ fall into the category of valence transitions of L-shell (Fe^{16+} to Fe^{23+}) ions. If the L-shell is fully occupied, valence transitions become inner-shell transitions in Fe^{15+} to Fe^{0+} ions. Following the nomenclature of Behar

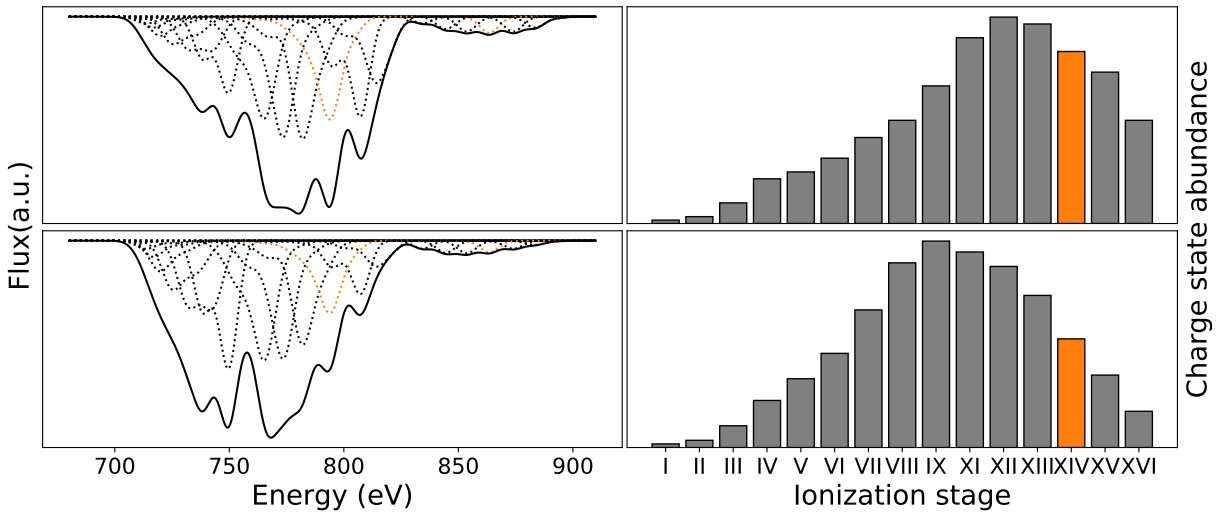

Figure 2: A simulated UTA absorbtion spectrum. The relative abundance of the ions is varied between the upper and lower spectra. As a result the structure, but also the center of gravity of the spectra change accordingly. Raw data adopted from [17].

et al.[13], they are from now on referred as Fe M-shell ions. The first astrophysical observation of absorbtion features caused by M-shell ions has been detected by Sako et al. [14]. Using the Reflection Grating Spectrometer (RGS) of XMM-Newton, 2p–3d absorption features produced by M-shell iron ions have been observed in the form of an unresolved transition array (UTA), a cluster of overlapping lines, which ca not be resolved. Similar absorption features have been observed in the soft x-ray spectrum of the Seyfert 1 galaxy NGC 3783 [15] (fig. 1), also obtained with the RGS. Since the structure and shape of the UTA depend on the involved ionization stages (fig. 2), one can use the UTA as a diagnostic tool. By properly modeling the observational data, the ionization structure, column density, and outflow kinematics of the absorbing materials can be determined.

So far these models were relying on *ab initio* atomic structure calculations since only few experimental laboratory measurements have been done. As mentioned by Gu et al. slight shifts in the calculated wavelengths can lead to drastic changes in the results of the model [16].

In order to increase the confidence of the theories applied for modeling the astrophysical plasma, theoretical results must be benchmarked by high precision experimental measurements. With the upcoming launches of next generation observatories like XRISM, which are equipped with modern microcalorimeter detectors, more precise laboratory

measurements are urgently needed [18].
To experimentally measure spectral lines, laserspectroscopy is one of the the most accessible and reliable methods. There are many table-top laser sources available, however most of them lack in the necessary flux or photon energy. Nowadays synchrotron radiation sources or free electron lasers are the only facilities able to provide such high photon energies with also high flux. The inherent broadband spectrum of synchrotron radiation, coming from an undulator, can be further narrowed down by utilizing a monochromator. Using such monoenergetic synchrotron radiation one is able to excite the transitions of interest in HCIs without contamination by other processes [19, 20]. Also in contrast to relying on energy resolving x-ray detectors like space observatories, modern synchrotron beamlines provide a resolving power of more than 10^{-5}, which allows most UTA features to be resolved.
The goal of this thesis is to benchmark theoretical calculations with experimentally determined transition energies and rates of the M-shell ion Fe^{13+}. For that purpose the PETRA III synchrotron radiation facility has been used to resonantly excite the highly charged iron ions produced by a compact electron beam ion trap. Using an ion extraction beamline the abundance of each charge state of iron inside the trap can be observed nearly simultaneously to the observed fluorescence. This technique allows also the observation of transitions, which are too weak in their radiative decay channel, since the competing auger channel can be observed in the change of the ion charge-state distribution.
The first chapter will introduce all theoretical concepts necessary for this thesis. The following chapter will give a detailed description of the experimental set-up and equipment. Here the emphasis will lie on the compact electron beam ion trap PolarX, which has been completely reassembled and equipped with the above mentioned extraction beamline. Basic components of the photon beamline of PETRA III will be briefly discussed. Following that, a broad overview of the experimental data will be presented. High attention will be given to one specific measurement containing two lines of the UTA. Utilizing a higher photon beam resolution the natural linewidth has been determined for those two lines. Since the natural linewidth of a line can give large insight to the absolute rate of a transition, effort has been put into determining the absolute transition rates.

2 Theory

An atom that has a significant amount of electrons stripped away is called an highly charged ion (HCI). These unique type of ions differ significantly from neutral or lowly charged ions in both experimental but also theoretical aspects [3]. High efforts and specialized set-ups are required to produce HCIs in the laboratory. Also from a theoretical perspective HCIs must be approached in a different way than neutral or lowly ionized atoms. Various effects like the finestructure and Lamb-shift are significantly enhanced in HCIs and must be included in the theoretical treatment.
Regarding the nomenclature, it is common to refer the charge state of a (highly charged) ion by the element with the same number of electrons in its neutral state. For example a neon atom with eight electrons removed would be called He-like neon. Another common practice in spectroscopy is to use roman numerals. Starting with the neutral state as I. Thus He-like neon can also be represented by NeIX.
In this chapter, theoretical and experimental concepts necessary for the understanding of spectra produced by HCIs will be discussed. Starting with a brief repetition of atomic structure theory of many-electron systems, followed by an overview of electronic and photonic processes. Finally a detour to astrophysics will take place with an emphasis on transition arrays, which is the main topic of this work.

2.1 Atomic structure

In the classical picture the spectral lines, which are of interest in this work, are produced by bound electrons changing their residing orbital due to an external influence. With the development of quantum mechanics in the 20th century it was for the first time possible to theoretically reconstruct these spectral lines. Centerpiece of this seminal theory is the Schroedinger equation, which applies wavefunction to describe all involved electrons along with the coupling structure of their internal and external angular momenta. The dynamics of the atomic system are contained in the Hamiltonian. Only if the Hamiltonian and the necessary wavefunctions are known, energy levels and transition rates can be determined.

2.1.1 The Schroedinger equation

The Schroedinger equation in its general form is an equation of motion, which describes the temporal evolution of a wavefunction ψ. It is given by

$$\hat{H}\psi(r,t) = i\delta_t\psi(r,t). \tag{1}$$

$\hat{H}$ is called the Hamiltonian operator or energy operator. It is usually given as a sum of a kinetic term, potential term and an interaction term, which describes the interaction of electrons with an external field. If one is only interested in stationary systems, the space and time-dependency of the wavefunction can be separated

$$\psi(r,t) = \psi(r) \cdot e^{-iE/\hbar}. \tag{2}$$

The time dependent Schroedinger equation can then be reduced to the time-independent Schroedinger equation

$$\hat{H}\psi = E\psi. \tag{3}$$

The time-independent Schroedinger equation can be seen as an eigenwert equation, with the energy E corresponding to the eigenvalue of the Hamilton operator for a given wavefunction.

2.1.2 The Hamiltonian

The most fundamental system discussed in atomic physics is the hydrogen atom. It consists of only two bodies. A nucleus (one proton and possibly neutrons) and an electron. For further simplification the discussion takes place in the rest frame of the nucleus. The Hamiltonian is then given by

$$\hat{H} = \hat{H}_{kin} + \hat{H}_{pot} = -\frac{1}{2m_e}\overrightarrow{\nabla}^2 - e^2\frac{1}{r} \tag{4}$$

with electron mass m_e, electron charge e and the distance of the electron to the nucleus given by r. Atoms and ions, which are discussed in this thesis, have multiple bound electrons. To generalize the above Hamiltonian, the respective kinetic and potential terms for all involved electrons have to be added. Additionally a term for the mutual electrostatic repulsion between electrons, which depend on the distance $r_{ij} = |r_i - r_j|$, needs to be taken into account. The generalized Hamiltonian is then given by

$$\hat{H} = \sum_{i=1}^{N}\left(-\frac{1}{2m_e}\overrightarrow{\nabla}^2 - e^2\frac{Z}{r}\right) + \sum_{\substack{i,j=1\\ i<j}}^{N}\frac{c^2}{r_{ij}}. \tag{5}$$

2.1.3 Spin-orbit interaction

Besides the electrostatic interaction between the electrons, an additional effect has been neglected in the discussion so far, namely, the interaction between spin and orbital angular momenta. This effect can be taken into account by adding an additional term to the Hamiltonian. It is given by

$$\hat{H}_{s-o} = \sum_{i=1}^{N} \frac{1}{2mr_{ij}} \frac{dV(r_i)}{dr_i} \hat{\vec{l}}_i \cdot \hat{\vec{s}}_i. \tag{6}$$

It describes for the i-th electron the interaction between the orbital angular momentum l_i and its spin angular momentum s_i. The total Hamiltonian can finally be given as

$$\hat{H} = \hat{H}_0 + \hat{H}_{elec-elec} + \hat{H}_{s-o}, \tag{7}$$

with H_0 as the sum of all single electron Hamiltonians and $H_{elec-elec}$ the electrostatic interaction term (eq. 5).

2.1.4 Coupling schemes

How the angular momenta of each electron are coupled together depends highly on the relation between $\hat{H}_{elec-elec}$ and $\hat{H}_{s-o}$. The relative strength influences the order in which the angular momenta are added to each other and as a result the energy eigenvalues shift correspondingly. For accurate theoretical treatment of multi-electron systems the right coupling scheme must be chosen. Figure 3 visualizes the gradual change in energy levels of Be-like ions for varying Z. For heavier ions jj-coupling replaces the LS-coupling, which has been valid for low Z.

LS-coupling. If spin-orbit effects are negligible relative to electrostatic effects ($\hat{H}_{elec-elec} >> \hat{H}_{s-o}$), $\hat{H}_{elec-elec}$ remains as the only perturbing term in the Schroedinger equation. In such a case the single electron angular momenta couple to form vectorial sums given by

$$\vec{L} = \sum_{i=1}^{N} \vec{l_i}, \ \vec{S} = \sum_{i=1}^{N} \vec{s_i}. \tag{8}$$

Both the total orbital angular momentum $\vec{L}$ and total spin angular momentum $\vec{S}$ couple to a total angular momentum $\vec{J}$. Any state can then be given by a set of quantum numbers

$$S\,, L\,, J\,, m_J. \tag{9}$$

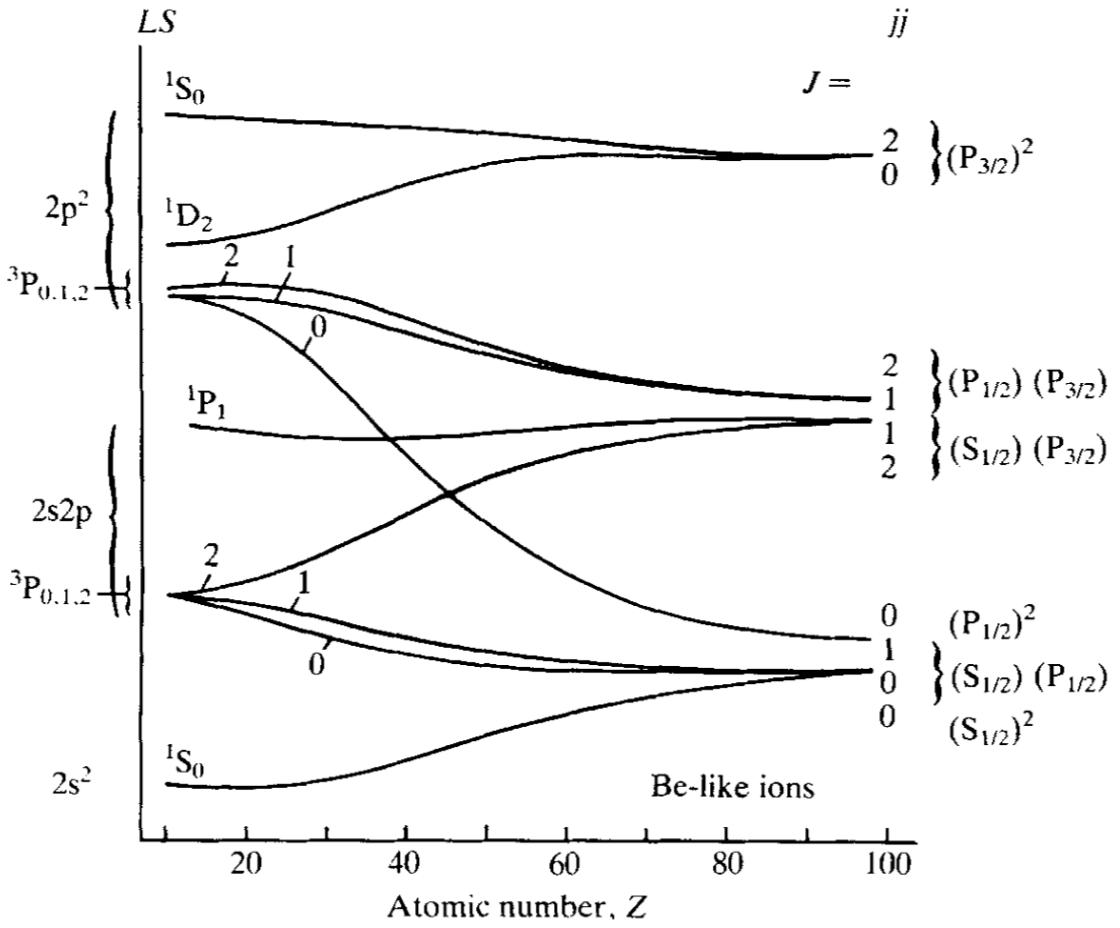

Figure 3: Visualization of the transition from LS to jj-coupling for varying Z. Figure adopted from [21].

Commonly the above quantum numbers are bundled as a term symbol

$$^{2S+1}L_J. \tag{10}$$

While the usage of term symbols can give quick insight, it has the downside that it is not unique. In complex atoms many combinations of angular momenta for a given electron configuration lead to the same term symbol. To uniquely identify and label a state or level one needs to include the so called parental history of its coupling structure, where term symbols are written successively for each electron starting from the most inner one.

$$(\dots (n_1 l_1^{x_1} (^{2S_1+1}L_1)\ n_2 l_2^{x_2} (^{2S_2+1}L_2))\ ^{2S_{1\&2}+1}L_{1\&2}) \dots n_m l_m^{x_m} (^{2S_m+1}L_m))\ ^{S+1}L_J. \tag{11}$$

jj-coupling. If electrons are affected by a strong coulomb field the single electron terms like $\vec{l_i} \cdot \vec{s_i}$ become more dominant and can even outweigh the contribution by the inter-

electronic repulsion (see fig. 3). In such a case the angular momenta are added in jj-coupling scheme, where the single electron angular momenta $\vec{l_i}$ and $\vec{s_i}$ couple to a total single electron angular momentua $\vec{j_i}$, which then are vectorially add up to the total angular momentum $\vec{J}$ of the whole system.

$$\left(... \left([n_1 l_1 \pm]_{j_1}^{x_1} \; [n_2 l_2 \pm]_{j_2}^{x_2}\right)_{j_{1\&2}} \; ... \; [n_k l_k \pm]_{j_k}^{x_k}\right)_J \tag{12}$$

Intermediate coupling. If the electrostatic repulsion term is comparable in strength to the spin-orbit term, the full Hamiltonian matrix is not diagonal in the jj- or LS-coupling scheme. The eigenvalues of the Hamiltonian must then be determined by a numerical diagonalization.

2.1.5 Multi-electron wavefunction

An appropriate multi-electron wavefunction must contain information regarding all spin and orbital angular momenta for each electron inside the atom. A common way to construct such multi-electron wavefunction Ψ is to simply take the n-fold product of one-electron wavefunctions ψ, also known as the Hartree-product

$$\Psi = \psi_1(r_1)\psi_2(r_2)\psi_3(r_3)\cdots\psi_n(r_n). \tag{13}$$

Here each subscript is an abbreviation for the one-electron quantum numbers n, l, m_l, m_s. While the Hartree-product satisfies the necessary orthonormality condition, it does not satisfy the Pauli principle. For the electron-interchanged wavefunctions $\Psi_a = \psi_1(r_1)\psi_2(r_2)$ and $\Psi_b = \psi_1(r_2)\psi_2(r_1)$ the Pauli principle states that, due to the physical indistinguishability of electrons, the probability density $|\Psi_i|^2$ must be the same for the two wavefunctions Ψ_a and Ψ_b. A direct consequence of this principle is the antisymmetry property of the wavefunction under exchange of electrons

$$\Psi_a = -\Psi_b. \tag{14}$$

An antisymmetrized wavefunction can be obtained by representing the Hartree product in the form of a determinant, which is referred to as a Slater determinant

$$\Psi = \frac{1}{\sqrt{N!}} \begin{vmatrix} \psi_1(r_1) & \psi_2(r_1) & \psi_3(r_1) & \cdots & \psi_n(r_1) \\ \psi_1(r_2) & \psi_2(r_2) & \psi_3(r_2) & \cdots & \psi_n(r_2) \\ \vdots & \vdots & \vdots & \ddots & \vdots \\ \psi_1(r_n) & \psi_2(r_n) & \psi_3(r_n) & \cdots & \psi_n(r_n) \end{vmatrix}. \tag{15}$$

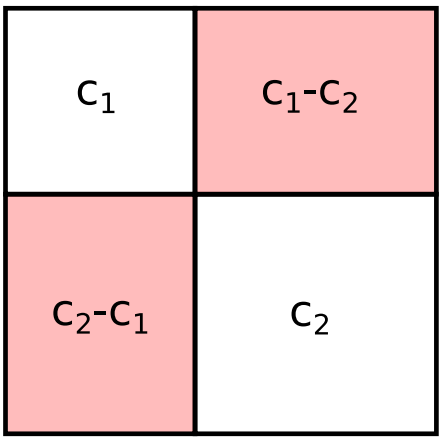

Figure 4: The general form of the Hamiltonian for two involved configurations. The Hamiltonian has been divided in four sub-matrices. c_1, c_2: energy matrix for one configuration basis functions. c_1, c_2 : configuration interaction matrices.

2.1.6 Hartree-Fock method

Using Slater determinants as wavefunctions the Hartree-Fock method solves the time-independent Schroedinger equation using a so called „self-consistent field method“. Beginning with a trial wavefunction, the Schroedinger equation is interatively solved by modifying the input wavefunction until the solution converges.
The Hartree-Fock method was developed in 1935 and is an revised version of the original Hartree method, which does not consider antisymmetry of the wavefunction. This procedure is $ab\ initio$. It uses no empirical data and solves the Schroedinger equation only using fundamental physical principles.
There are improved versions of the Hartree-Fock method which are often called post-Hartree-Fock methods. While small differences may exist, all include additionally the electron correlation, which is neglected in the central-field approximation of its predecessor. Modern methods also add relativistic effects into the equation or use the Dirac equation instead of the Schroedinger equation.

2.1.7 Configuration interaction

In the theoretical approaches discussed in the previous chapter the wavefunction for an atomic state k has been expanded by a set of single-electron basis functions ψ all from a single configuration. By disbanding this restriction and including basis functions of more than one configuration, a significant improvement in accuracy for the

total wavefunction Ψ can be obtained. This effect is caused by the interaction between configurations (CI). The most simple case, where CI can happen, is by including basis functions of two configurations. In that case the hamiltonian matrix can be thought of as being divided into several submatrix elements (fig. 4). The two matrices located on the diagnonal c_1 and c_2 are the energy matrices. Both are the same as when considered separately. However off-diagonal "configuration interaction" matrices, which are in general rectangular, appear inside the matrix. Mathematically the CI matrices are calculated the same as for the energy matrices, except that the initial and final wavefunctions come from different configurations. It can be seen that the existence of off-diagonal matrices have an non-negligible influence on the eigenvalues of the matrix.
As a result, to gain accurate energy eigenvalues, one needs to implement all possible configurations into the wavefunction, which is practically impossible to solve. However, most elements of the CI-matrices are negligibly small. This is due to selection rules, which allow a heuristical approach in choosing the set of configurations involved in the calculations.
First of all the Hamiltonian operator has even parity. As a result, the initial and final functions must have the same parity to obtain a non-zero eigenvalue. Since the parity of a wavefunction is given by its configuration, one must only consider additional configurations with the same parity as the configuration of primary interest. Another selection rule arises from the fact that only one or two-electron operators (repulsion and and spin-orbit term) are involved in the Hamiltonian. Only configurations, which differ by two orbitals at most lead to non-zero CI-elements.
A last qualitative selection rule can be formulated regarding the strength of CI. It has been shown that CI effects tend to be largest for configurations with similar center-of-gravity energies, since various wavefunctions tend to have large overlap under this condition.
The accuracy of all CI based atomic structure codes (e.g. FAC) highly depends on the input configurations. To save computational time for own calculations it is helpful to grasp the underlying concepts and choose the set of configurations efficiently.

2.1.8 Terminology: Configuration, term, level and state

The word „state“is often interchangeably used with other terminologies like „term“or „level“, which all have different physical definitions. To reduce possible confusion, brief explanations will be given below. A schematic explanation is given in figure 5.

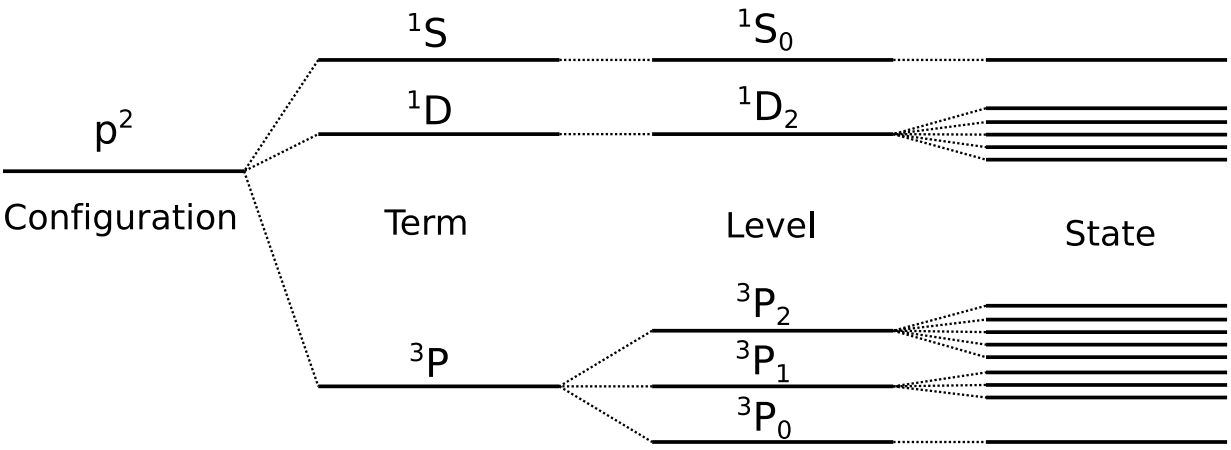

Figure 5: Simplified diagram of the relation between "configuration", "term", "level" and "state".

Configuration. An atom or ion consists of a nucleus and a given number of electrons. All electrons can be labelled with a principal quantum number n and an orbital quantum number l. The configuration determines the occupancy of orbitals for each electron, e.g. the configuration for the groundstate of an lithium atom can be given as $1s^2 2s^1$.
Term. As mentioned above, if the electrostatic repulsion term is included in the Hamiltonian additional „good“quantum numbers are introduced to define the system. The total orbital angular momentum L and total spin angular momentum S. The combination of L and S is called a term. The term is usually given as a term symbol in the form ${}^M L$. With the multiplicity $M = 2S + 1$.
Level. The degeneracy in L is resolved by considering spin-orbit interaction. Including the total angular momentum J to the term one obtains a level given by ${}^M L_J$.
State. It is known that each level has an additional degeneracy given by its statistical weight $g = 2J + 1$. To spectroscopically reveal this splitting a strong magnetic field (Zeeman effect) or electric field is necessary (Stark effect). The state is fully defined by the magnetic quantum number m_J and its corresponding level ${}^M L_J$.

2.2 Electronic and photonic processes

2.2.1 Photoexcitation

A bound electron in an energy level 1 can be excited to an energetically higher level 2 by absorbing a photon with an energy matching the difference in energy between the

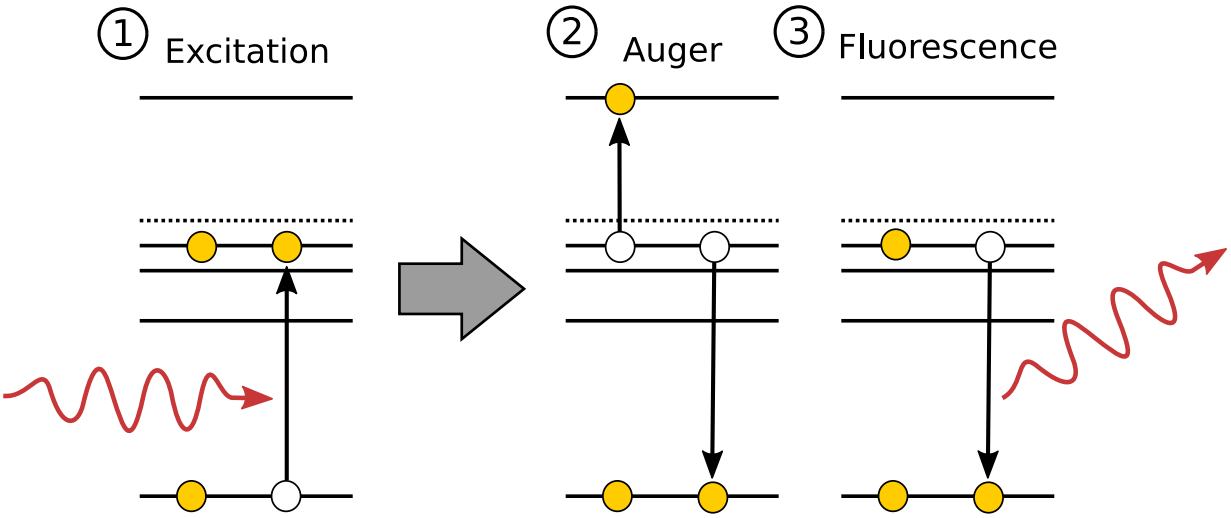

Figure 6: Schematic representation of the decay processes following initial photoexcitation (1). (2): An excited electron relaxes to the groundstate while its energy is transferred to a secondary electron, which as a result is excited to a continuum state. (3): The electron relaxes to the groundstate by emission of a photon.

two levels of interest (see fig.6).

$$X^{q+} + \gamma \rightarrow X^{q+*},\ E_\gamma = E_2 - E_1 \tag{16}$$

Due to its resonant nature this process allows a selective excitation of energy levels. The transition rate is proportional to the energy density ρ_ω and is given by

$$W_{12} = B_{12}\rho_\omega \tag{17}$$

with the Einstein-coefficient for absorption B_{12} [22].

2.2.2 Auger decay

If an ion resides in a doubly excited state it can decay to an energetically lower state by an Auger process (see fig.6) [23]. It is a non-radiative decay, where the released energy is transferred to an bound electron. The electron is then emitted with a kinetic energy $E_{kin} = E_{21} - E_B$. With the binding energy E_B of the emitted electron.

$$X^{q+*} \rightarrow X^{(q+1)*} + e^-. \tag{18}$$

The Auger process can only happen if the excitation energy of the doubly excited state is higher than the ionisation energy of the ion in its groundstate.

2.2.3 Spontaneous emission

An ion in an excited state can decay back to a lower energetic state by spontaneously emitting a photon (see fig.6)

$$X^{q+*} \rightarrow X^{q+} + \gamma. \tag{19}$$

The transition rate for this process is given by the Einstein-coefficient A_{21} [22], which can be given as a function of the transition matrix-element M_{12} by

$$A_{12} = \frac{16\pi^3\nu^3}{3g_2\epsilon_0 hc^3}|M_{12}|^2 \tag{20}$$

with the statistical weight g_2, vacuum permitivity ϵ_0 and the planck constant h. The above mentioned matrix element is a measure for the strength of a transition. In the dipole approximation, it can is given as

$$M_{12} = \int \Psi_1 r \Psi_2^* d^3r. \tag{21}$$

Several selection rules can be deduced based on symmetry considerations.

$$\Delta L = \pm 1 \tag{22}$$

$$\Delta M = 0 \text{ (for linear polarisation)} \tag{23}$$

$$\Delta M = \pm 1 \text{ (for circular polarisation)} \tag{24}$$

$$\Delta J = 0,\ \pm 1 \text{ (J_1 = 0 to J_2 = 0 is excluded)} \tag{25}$$

2.2.4 Transition arrays

In the 1970s the investigation of emission spectra of heavy, highly charged ions was a fast moving research field. Various plasma, produced by tokamaks, vacuum sparks and laser has been investigated since then [24, 25, 26]. The recorded spectra were highly complex due to the superposition of many lines emitted by various charge states. Another reason which enhanced the complexity of the spectra were the usually large quantum numbers of the outermost occupied subshells of the involved configurations (frequently 3d, 4d or 4f). Those high angular momenta lead to large number of levels and therefore to a even larger number of lines. For that reason many lines (broadened by Doppler, Stark and collisional effects and the limited resolution of the instrumental resolving power) were recorded in a given energy band, which were in general unresolved and coalesce into a broad line structures. To describe the totality of lines resulting

between two configurations Condon and Shortley defined the term „transition array“. To interpret these transition arrays many attempts have been done to analyse the experimental transition arrays by detailed computational methods. Since often times thousands of lines are involved in a single array, the calculations were time consuming and still ended up in inconclusive results due to the nearly structureless experimental data ([27]). In the late 1970 a new model has been introduced ([28]), which considered the transition-array structure as a statistical distribution of intensities, where mean wavelengths, spectral widths and asymmetry were used to characterize the array. This model of unresolved transition arrays emerged as a convenient tool to describe low resolution x-ray spectra emitted by hot plasmas ([29]).

2.2.5 Unresolved transition arrays in astrophysical observations

Unresolved transition arrays have been observed not only in laboratory experiments, but also in astrophysical plasma. For example by viewing at an active galactic nuclei (AGN) directly towards the source a rich absorption spectrum can be obtained. The absorption lines observed are in general slightly shifted to shorter wavelengths, which is due to the outflowing wind. By determining the energetic shift of the absorption line the velocity of the wind can be extracted[15]. One distinctive feature of the absorption spectrum are the $2p \longrightarrow 3d$ inner-shell absorption lines of several iron charge states. Initially it has been observed in the x-ray spectrum of IRAS 13349+2438 obtained with the Reflection Grating Spectrometer on board of XMM-Newton [30]. Many other discoveries of M-shell UTAs have been claimed thereafter. An detailed analysis of such UTA absorption spectrum by Holczer et al.[15] using the atomic data provided by Behar et al. [13] concluded that the low ionization stages of iron, which produce the UTA absorption feature, is contrarily to the initial assumption in fact not outflowing with the same velocity as the rest of the wind. As stated by Holzer et al. the results of the analysis were highly sensitive to the atomic data provided by Behar et al., which were calculated using the configuration interaction based HULLAC [31] code. Indeed a reanalysis of Gu et al. using relativistic many body perturbation (MBPT) calculations showed an systematic deviation of $15 - 45\mathrm{m\AA}$ $(\approx 1.5\,\mathrm{eV})$ to the HULLAC calculations [16].The theory of Gu et al. has been checked for accuracy using one single laboratory measurement of Fe xvi lines of Brown et al.[32].

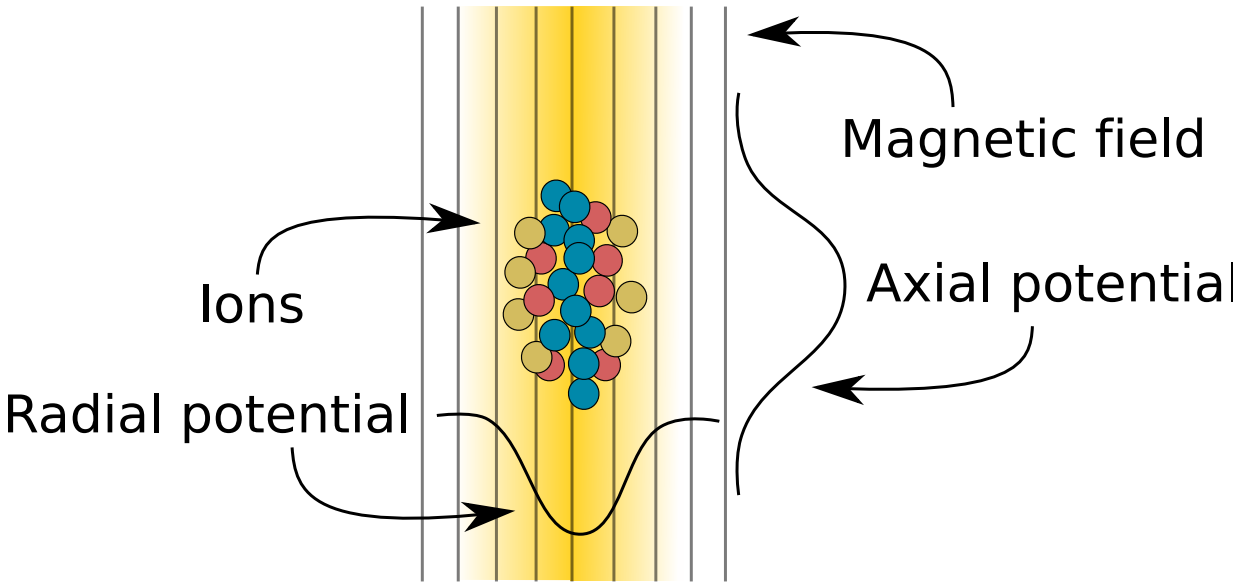

Figure 7: Working principle of the Electron Beam Ion Trap. Inside an homogeneous magnetic field (vertical lines) ions are trapped in radial direction by the negative space charge of the dense electron beam (yellow) and axially by a potential well produced by a set of electrodes (not drawn) with voltages applied.

2.3 The Electron Beam Ion Trap

The first Electron Beam Ion Trap (EBIT) has been designed and build in the 1980s at the Lawrence Livermore National Laboratory ([33]). Similarly to an Electron Beam Ion Source (EBIS) it produces highly charged ions by electron impacts. The ions are sequentially stripped off their electrons until the energy of the electron beam is insufficient to produce higher charge states. To efficiently ionize the electrons the electron beam is compressed by a high magnetic field, usually produced by a pair of (superconducting) Helmholz coils. Guided by electrostatic lenses the electron beam reaches its highest compression at the interaction zone with the ions. There the ions are axially trapped by an electrostatic potential well and radially by the space charge of the electron beam. Compared to other sources of HCIs (e.g. storage rings) the EBIT produces ions with a mean velocity of zero. Further cooling is possible by evaporative methods, which makes use of an EBIT for spectroscopy feasible. 40 years after its invention EBITs have been build around the world. E.g. the Tokyo-EBIT, which can generate an electron beam of up to $340\,\mathrm{keV}$ while maintaining a current of $250\,\mathrm{mA}$. Such high specifications make even the production of hydrogen-like uranium feasible [34].

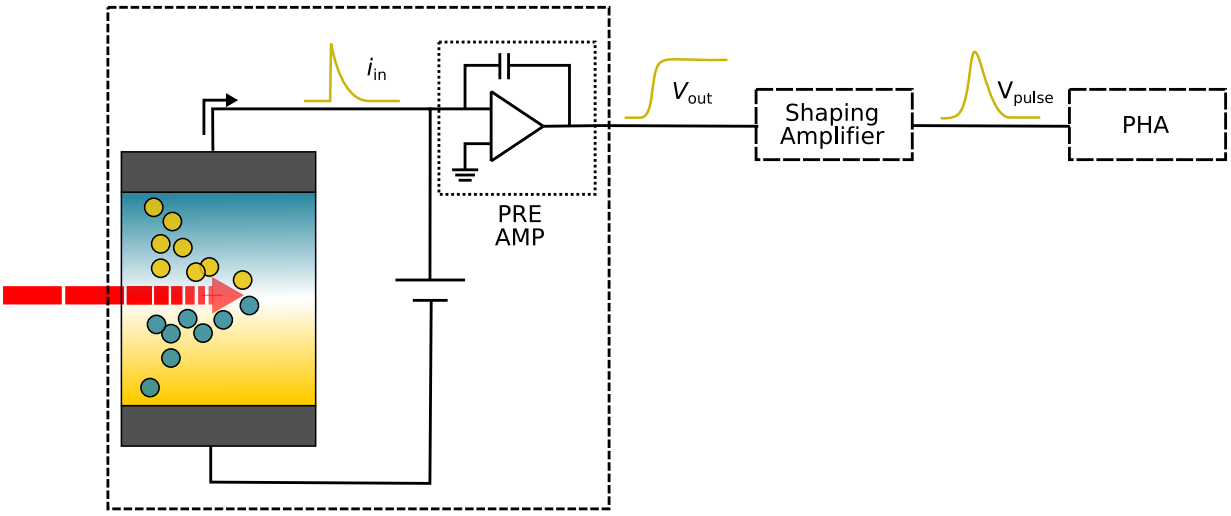

Figure 8: Principle of a semiconductor detector. Incident radiation produces a cascade of electrons. The electrons are collected due to an applied voltage. The current pulse enters a charge sensitive amplifier (preamplifier), which converts the current pulse to a measurable voltage step. Finally a shaping amplifier produces a voltage pulse, whose height is proportional to the height of the step function. Since the height is related to the energy of the incident photon, pulse height analysis yields information regarding the energy.

2.4 Semiconductor detectors

The principle of the semiconductor detector is very similar to that of the ionization chamber. Instead of the gas cell a rectifying p-n junction is used, where a voltage is applied to capture the electrons liberated by the incident ionizing radiation. Due to the applied electric field, the electrons drift towards the electrodes and form a current pulse. The current pulse is integrated and usually post-processed by a shaping amplifier. Due to the high number of initially released electrons, the height of the produced pulse can be determined accurately. The pulse height is directly related to the energy of the incident photon energy (fig. 8).

2.4.1 Poissonian statistics and limited resolution

It is experimentally known that on average $w = 3.62\,\mathrm{eV}$ [35] (at room temperature) are necessary to produce an electron-hole pair in a solid state silicon wafer. The deviation of this value from the band gap energy of approximately $1\,\mathrm{eV}$ indicates that most energy

results in excitation of phonons. For an incident photon energy E the mean number of electron-hole pairs can then be given as $\bar{N} = E/w$ [36]. Even if all external parameters are kept constant $\bar{N}$ is subjected to a fluctuations. The amount of fluctuation or the variance

$$\sigma^2 = F \cdot \bar{N} \tag{26}$$

is of high interest since it does give an upper limit to the theoretically achievable resolution of the experiment. The so called Fano parameter F [37] [38] is a material dependent parameter. It is equal to one if the number of ionizations is fully governed by a poissonian statistic and zero if there is no fluctuation in N for given incident photon energy. For silicon and germanium F is approximately equal to 0.1. Calculating the energy resolution for a silicon detector leads to

$$\frac{\Delta\bar{N}}{\bar{N}} = \frac{\sqrt{F \cdot \bar{N}}}{\bar{N}} = \frac{\Delta E}{E} \tag{27}$$

$$\Delta E = \sqrt{w \cdot F} \cdot \sqrt{E} \approx 0.6 \cdot \sqrt{E}. \tag{28}$$

For example the theoretical limit for the He-like oxygen K_α line at $574\,\mathrm{eV}$ would be a FWHM of $33\,\mathrm{eV}$ at room temperature. Modern Silicon drift detectors reach an experimental resolution very close to the theoretical limit of $\approx 60\,\mathrm{eV}$.

2.5 Q/m determination: Time of flight

Many charge states of different elements can exist inside a plasma. The charge-to-mass ratio q/m of an ion is a parameter, which is often used to label a given charge state of an element. A very effective diagnostic tool for the identification of charge-to-mass ratios is a time-of-flight mass spectrometer (fig. 9). The principle of such measurement is explained below. A more indepth discussion can be found in various textbooks, e.g. [39].

By accelerating a small volume of ions, whose mass is to be determined, to a kinetic energy E_{kin} the sample achieves a velocity, which is given by

$$v = \sqrt{\frac{2 \cdot E_{kin}}{m}}. \tag{29}$$

The kinetic energy is given by the acceleration voltage U and the charge state of the ion q. The ions drift with constant speed through space and hit a detector placed at a

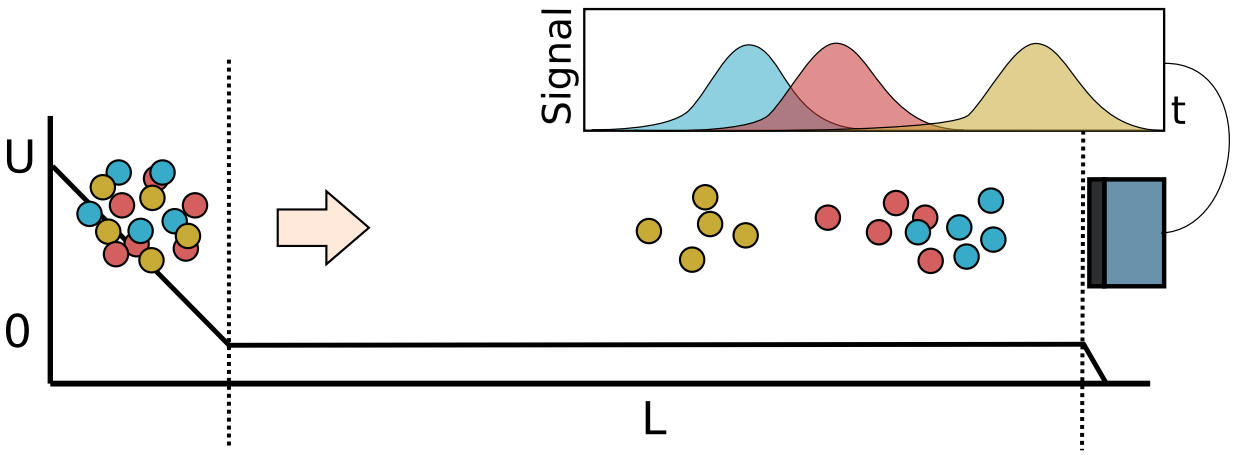

Figure 9: A mixture of ions with varying mass and charge accelerated towards an detector. The time at which a ion species hits the detector depends on its mass and charge.

distance L. The time at which an ion hits the detector is given by

$$\Delta t = L \cdot \sqrt{\frac{m}{2E_{kin}}} = L \cdot \sqrt{\frac{m}{2qU}}. \tag{30}$$

By reformulating above equation one yields an equation for q/m, which only depends on the experimental parameters U, L and the time of flight Δt

$$\frac{q}{m} = \frac{L^2}{2\Delta t U}. \tag{31}$$

2.6 Angular distribution of fluorescence photons

If a two-step process is considered, starting with a photo-excitation of an initial state to a intermediate state by a polarized light source ending with a radiative decay of the intermediate state to a final state, the usual assumption of isotropic emission of photons is in general not valid. In fact there is a strong dependency of the intensity of emission on the direction of observation [40]. Within the dipole approximation one can quantify the preference of emission as a function of the total angular momenta of the involved states and the polarisation of the incident photon beam. A general equation for the distribution of emitted photons can be given as

$$W(\theta, \phi) = \frac{W_0}{4\pi}\left[1 - 3\sqrt{\frac{2\pi}{15}}\beta \sum_q \rho_{2q}^{\gamma_0} Y_{2q}(\theta, \phi)\right] \tag{32}$$

Table 1: The elements of the statistical tensor ρ are given in two different frames to simplify further calculations.

ρ^{γ}_{kq}	S	S′
ρ^{γ}_{00}	$\frac{1}{\sqrt{3}}$	$\frac{1}{\sqrt{3}}$
ρ^{γ}_{10}	$\frac{P_3}{\sqrt{2}}$	0
$\rho^{\gamma}_{1\pm1}$	0	$\mp P_3$
ρ^{γ}_{20}	$\frac{1}{\sqrt{6}}$	$\frac{-(1+3P_1)}{2\sqrt{6}}$
$\rho^{\gamma}_{2\pm1}$	0	$\frac{iP_2}{2}$
$\rho^{\gamma}_{2\pm2}$	$-\frac{(P_1\mp iP_2)}{2}$	$\frac{(1-P_1)}{4}$

with the spherical harmonics Y_{lm} and the anisotropy parameter β defined as:

$$\beta = 3(-1)^{1+J_0-J_f}(2J+1)\begin{Bmatrix} 1 & 1 & 2 \\ J & J & J_f \end{Bmatrix}\begin{Bmatrix} 1 & 1 & 2 \\ J & J & J_0. \end{Bmatrix} \tag{33}$$

The terms in the large curly brackets are the so called 6-J symbols. To circumvent tedious calculations of the symbols, one can use the handy web-application of Anthony Stone [41]. Notice that β only depends on the angular momenta of the involved states, not the polarisation of the photon. The influence of the polarisation is included in the statistical tensor ρ.

2.6.1 Linear polarisation

To simplify calculations a frame S′, varying from the usual laboratory frame, is chosen. The relation of S′ to the laboratory frame is illustrated in figure 10. The advantage of choosing this frame can be seen here: For linear polarisation the Stokes parameters are $P_1 = 1, P_2 = P_3 = 0$. Then the only non-zero term for the statistical tensor ρ_{2q} in this frame is $\rho_{20} = \frac{-2}{\sqrt{6}}$ (see table 1). Substitution of the statistical tensor into equation 32 leads to

$$W'(\theta,\phi) = \frac{W_0}{4\pi}\left(1+\beta P_2(\cos\theta)\right). \tag{34}$$

with the second order Legendre polynomial P_2.

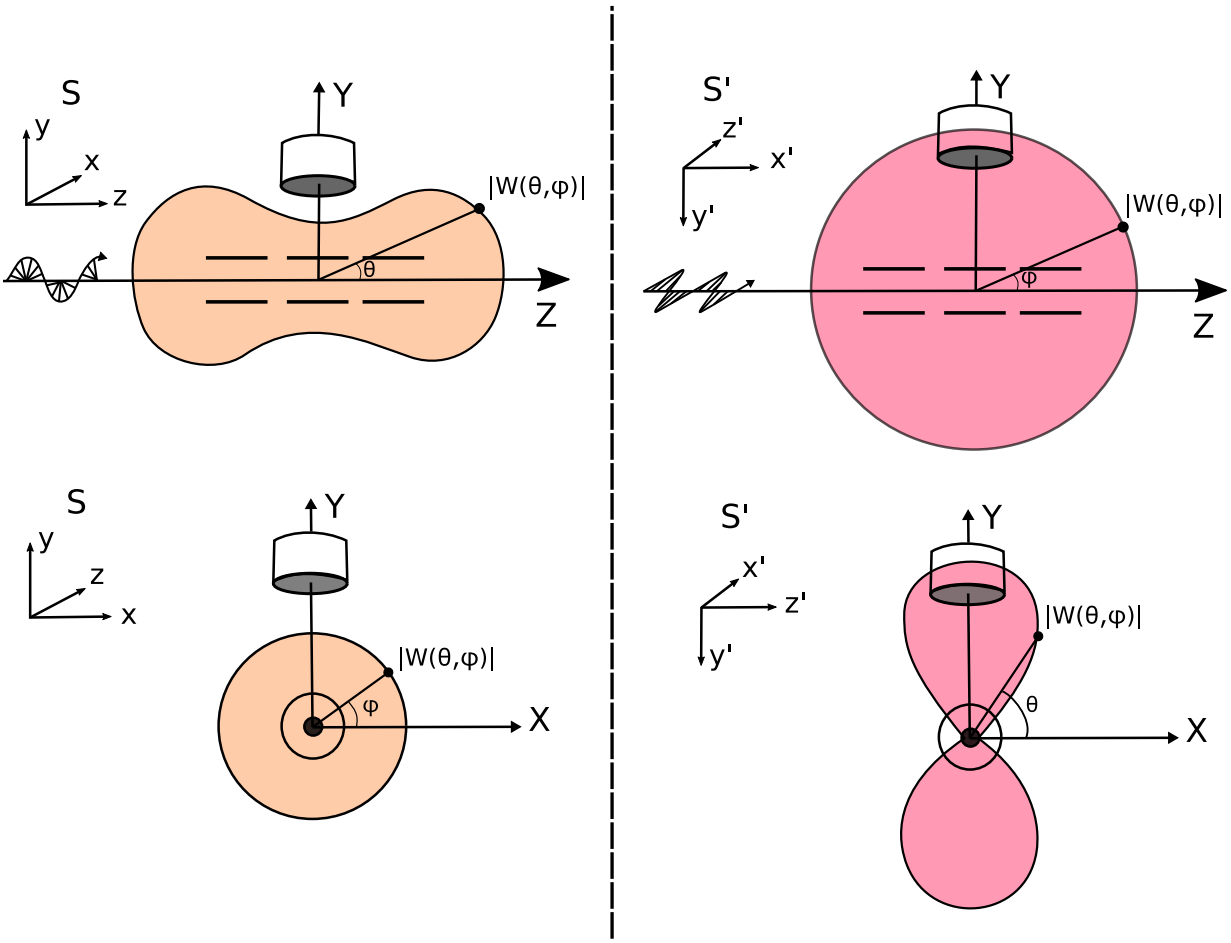

Figure 10: The modulus of angular distribution given as a function of θ and ϕ in different frames (incident polarisation). The figures on the left side correspond to circular polarisation and the figures on the right side to linear polarisation of incident photon beam.

2.6.2 Circular polarisation

For circular polarisation the Stokes parameters are given by $P_1 = P_2 = P_3 = 0, P_4 = 1$. It can be seen in table 1 that the statistical tensor is independent of P_4. The theoretical treatment is therefore the same as for unpolarized light. This time it is more convenient to work in the S (laboratory) frame. Here the sum over the statistical tensor leaves one term $\rho_{20} = \frac{1}{\sqrt{6}}$. The photon distribution can then be given as:

$$W(\theta, \phi) = \frac{W_0}{4\pi} \left(1 - \frac{\beta}{2} P_2(\cos\theta)\right) \tag{35}$$

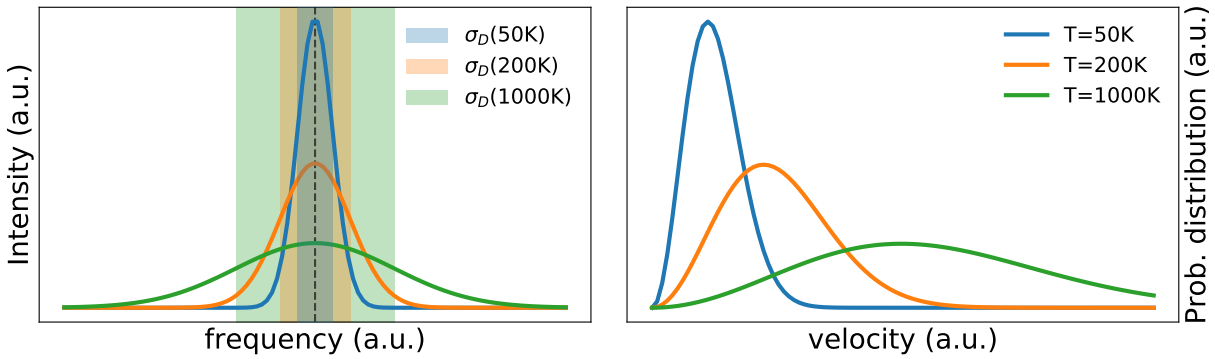

Figure 11: The effect of Doppler broadening is visualized for three different velocity distributions (right). The shaded area correspond to the width of profile in the same color.

2.6.3 The choice of frame of reference and the axis of symmetry

Choosing different frames can be helpful for the derivation of equation 34 and 35 but might lead to confusion if the formula is applied to the actual experiment. For incident circularly polarized photons the angular distribution of emitted photons shows a cylindrical symmetry with respect to the beam axis (fig. 10). However the symmetry properties for linear polarisation are different. For horizontally aligned photon polarization the laboratory frame x-axis becomes the axis of symmetry. Unlike for circular polarisation this leads to a theta dependency for the angular distribution.

2.7 Gaussian, Lorentzian and the Voigt profile

As has been discussed in chapter 2.2.3 an excited state will decay after some time due to interaction with the vacuum back to an energetically lower state. This characteristic time is called the lifetime of an excited state. By applying Heisenberg's principle

$$\Delta E \cdot \Delta \tau \geq \frac{h}{4\pi} \tag{36}$$

one can see that the lifetime $\Delta\tau$ corresponds to an energy ΔE. The natural linewidth ΔE can be observed as the width of the Lorentzian

$$L(E) = \frac{1}{\pi} \frac{\Delta E}{(E - E_0)^2 + \Delta E^2}, \tag{37}$$

for a transition energy of E_0. One has to emphasize that the natural linewidth takes all possible decay channels into account. If a given excited state decays via several

radiative transitions but also to continuum states through Auger processes the natural linewidth corresponds to the sum of all radiative and Auger rates.

$$\Gamma = \hbar \cdot \left(\sum_i A_{rad,i} + \sum_j A_{auger,j} \right) = \hbar \cdot A_{total} \tag{38}$$

Experimentally the natural linewidth often refuses to be observed directly. Several experimental factors can overshadow the natural linewidth, due to its narrow nature.

Doppler broadening. If the target consists as an ensemble of ions in a small volume, ions tend to heat up by collisions. If the system is in a thermal equilibrium the velocity v of ions follow the Maxwell-Bolzmann distribution

$$P(v)\ dv = (\frac{m}{2\pi kT})^{3/2} 4\pi v^2\ exp\left(-\frac{mv^2}{2kT}\right) dv \tag{39}$$

where m is the particle mass, k the Bolzmann constant and T the temperature in Kelvin. Any velocity component v_i is then given by a symmetric gaussian-like distribution

$$P(v_i)\ dv = \sqrt{\frac{m}{2\pi kT}}\ exp\left(-\frac{mv_i^2}{2kT}\right) dv \tag{40}$$

By introducing the first order Doppler shift $f = f_0 \cdot (1 + v/c)$ into the equation one yields the formula for the Doppler broadened profile

$$P(f)\ dv = \sqrt{\frac{m}{2\pi kT f_0^2}}\ exp\left(-\frac{mc^2(f - f_0)^2}{2kT f_0^2}\right) dv. \tag{41}$$

The distribution follows a Gaussian profile with standard deviation $\sigma_D = \sqrt{kT/mc^2} \cdot f_0$.

Instrument profile. Another important influence is given by the energy distribution of the photonbeam, which is used to excite the target ions. Even the best monochromator in the world cannot produce monochromatic light. The energy distribution is often estimated as gaussian-shaped. But in fact it depends on the entrance and exit slit width and the resolution of the spectrometer.

The recorded spectrum is then given as the convolution of the real spectrum (convolution of Lorentzian and broadening effects) and the instrumental profile. The recorded spectrum can then be modelled by a Voigt profile, which is the distribution obtained by the convolution of a Lorentzian and Gaussian profile

$$V = G * L = \frac{Re(w(z))}{\sigma\sqrt{2\pi}}, \tag{42}$$

where $w(z)$ is the Faddeeva function, evaluated for $z = (E + i\Delta E)/(\sigma\sqrt{2})$. The limiting cases, $\sigma = 0$ and $\Delta E = 0$, result in the Gaussian G and Lorentzian L, respectively.

3 Experiment

3.1 The PolarX-EBIT

The PolarX-EBIT (fig. 12) is one of the Heidelberg compact electron beam ion traps (HC-EBIT, [42]). Instead of the commonly used superconducting magnets, the magnetic field of a HC-EBIT is produced by permanent magnets and guided by soft iron pieces to the center of the trap, reaching a maximum at the center of the trap (approximately $900\,\mathrm{mT}$). The electron beam is produced by a modified pierce-type „off-axis“electron gun (see fig. 13). Unlike conventional electron guns, the off-axis gun employs a cathode displaced from the main axis by an angle of 22 degrees, which allows direct optical access to the center of the trap, where an external light source (e.g. synchrotron or laser beam) can be put through. To allow such unconventional placement of the cathode, the focus electrode as well as the anode electrode, which are used to steer and accelerate the electron beam, are split in two. The focus electrodes are used to compensate the Lorentz force, which acts on the electron beam, due to the displaced position of the cathode.
Compared to an usually employed on-axis electron gun, where the sole purpose of the anode is the acceleration of the electrons, the anode of the off-axis electron gun has the additional function of bending the electron beam to the main axis. This is accomplished by creating a 35° plane between both parts of the split anode (see fig. 13).
The central chamber of the PolarX-EBIT encloses the drift tube assembly, consisting of six individual cylindrical electrodes. The first two drift tubes are used for refocusing and guiding the electron beam through the whole assembly. The third, fourth and fifth electrodes are located in the central region of the trap. The purpose of these three drift tubes is the axial confinement of the ions produced inside the fourth drift tube. Drift tube six is used to steer the beam to the collector electrode, on which the electron beam is dumped.
The central chamber has two open ports, which can be equipped with a variety of detectors to analyze the photon emission of the ion cloud. For this experiment two silicon drift detectors where mounted. Additionally, the rear part of the EBIT is connected to an electrostatic extraction beamline, which allows the ejection of the trap content for charge state analysis. To ensure optical access through the whole setup, the extraction beamline is equipped with an electrostatic bender. Finally, a channeltron setup is used to collect the ions. A schematic depiction of the whole setup can be seen in figure 16.

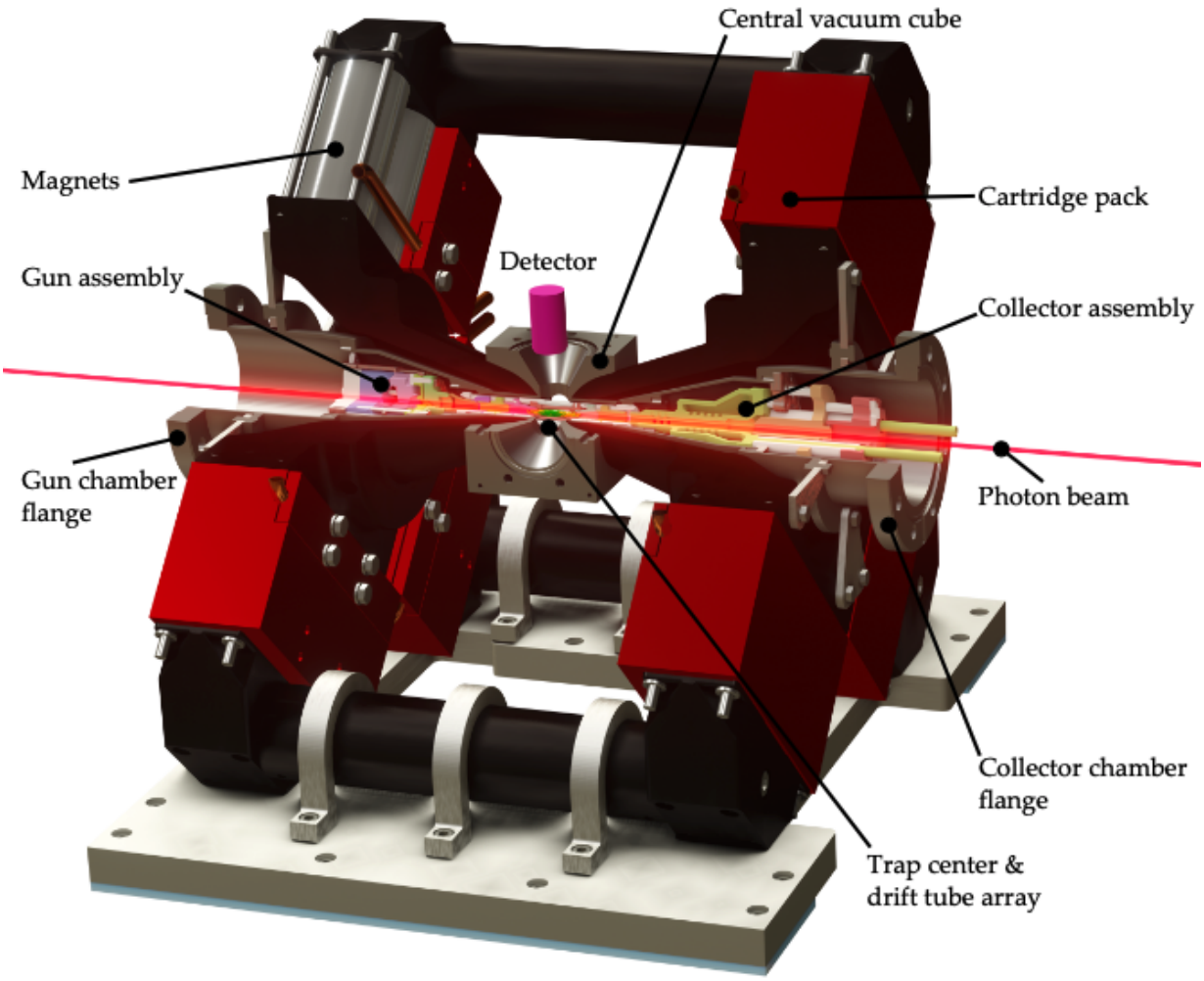

Figure 12: CAD model of the PolarX-EBIT. The magnetic field is produced by permanent magnets stacked inside cartridges. The off-axis design of the electron gun allow a photon beam to pass through the main axis of the EBIT. Figure adopted from [43].

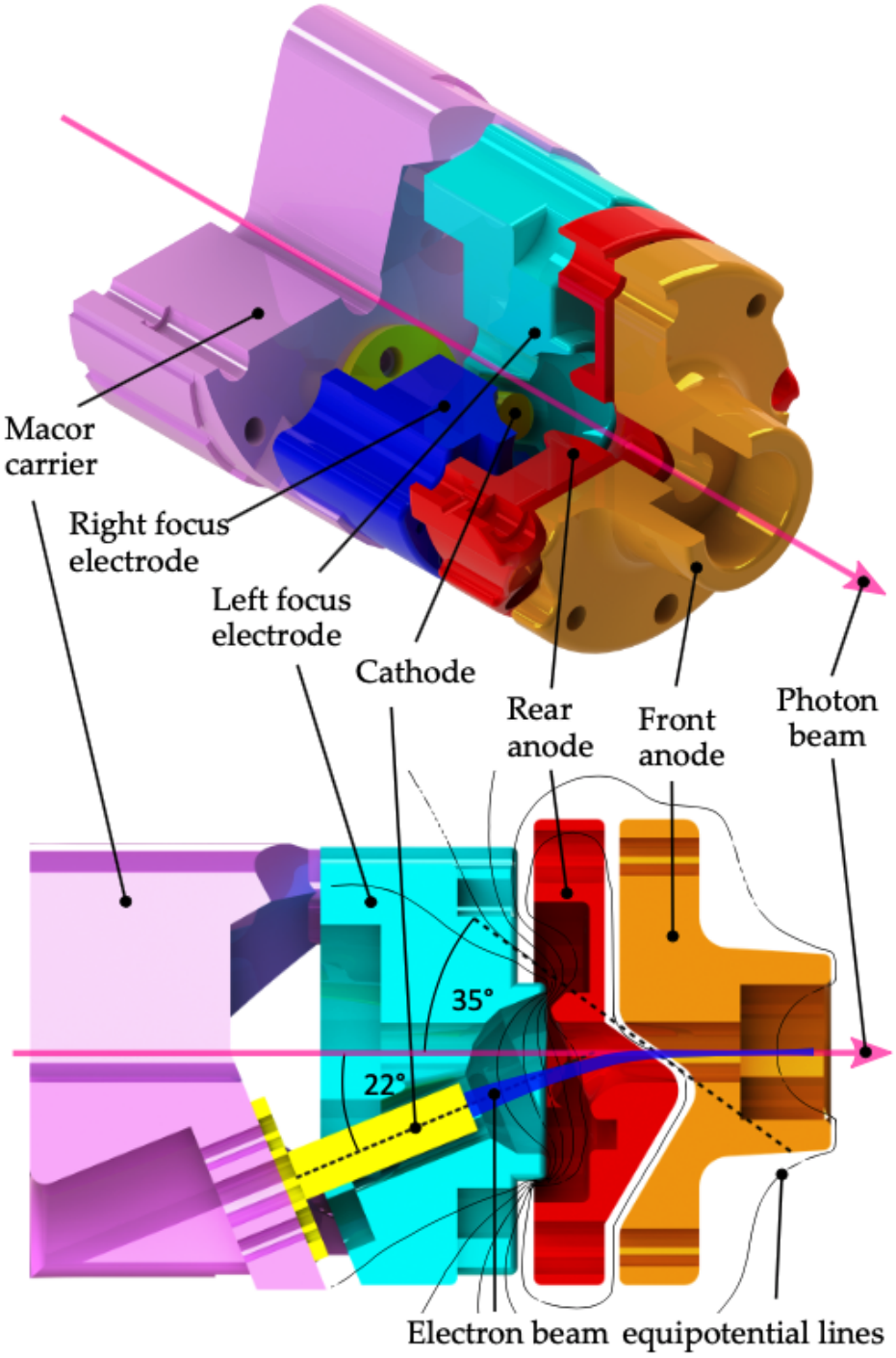

Figure 13: CAD model of the off-axis gun. The cathode (yellow) is located between the carrier and the foci. The 22° tilt of the cathode enables the photon beam to pass throught the gun. The split foci(blue) and anode(red and orange) steer the emitted electron beam towards the main axis of the electrode gun. Figure adopted from [43].

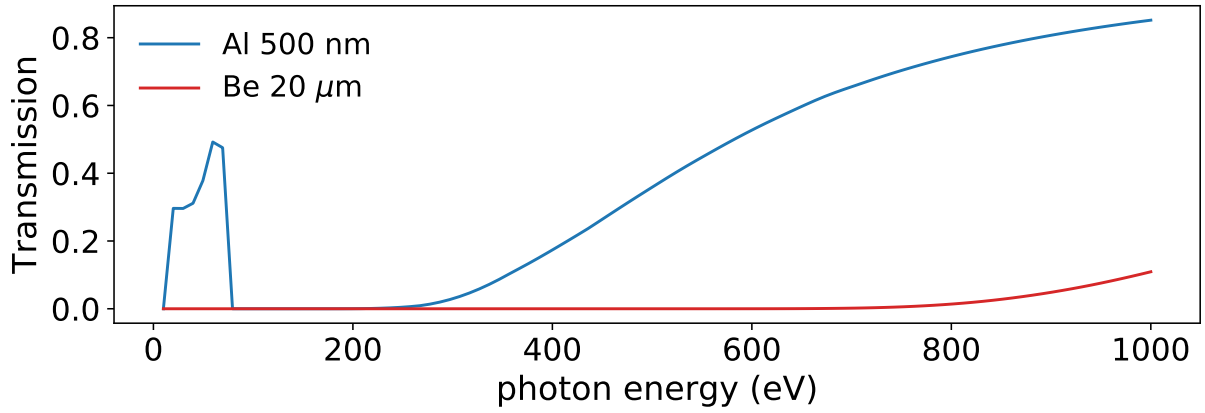

Figure 14: Transmission characteristics of a common beryllium window compared to the aluminium filter used in this work.

3.2 Data acquisition system

The main data acquisition system of the experiment is the MPA4 „Multiparameter Multichannel Analyzer“of Fast ComTec company [44]. It is a multiparameter data aquisition system, which can be used to produce histograms using up to 8 ADCs as inputs with a resolution of 16bit over a range between 0 to $10\,\mathrm{V}$. Besides the MPA4 hardware, a software called MPANT is also provided to allow live observation of one and two dimensional histograms. Since the time-information is lost in the histograms made with MPANT, the acquired data is additionally saved as a Lstfile, where each event is stored with a timestamp. Furthermore coincidence conditions can be set in between any ADC channels. While the MPA4 system is mainly used for the photon pulses and few ADC channels, a Logfile is simultaneously written during the measurement, where all relevant parameters are saved, e.g., pressure, photon energy, voltages applied on the EBIT-electrodes.

3.2.1 The 7072 Dual Timing 500ns ADC (TADC)

The TADC, whose output is fed into the MPA4 system can be operated in three different modi. Each modus is explained below.

Pulse height analysis mode (PHA). PHA is used to measure a given analogue pulse height and to digitize and store its value. If the amplitude is proportional to the energy of the initial photon or particle one can record an energy spectrum. Three important parameters exist for PHA. The ADC threshhold, lower level discriminator (LLD) and

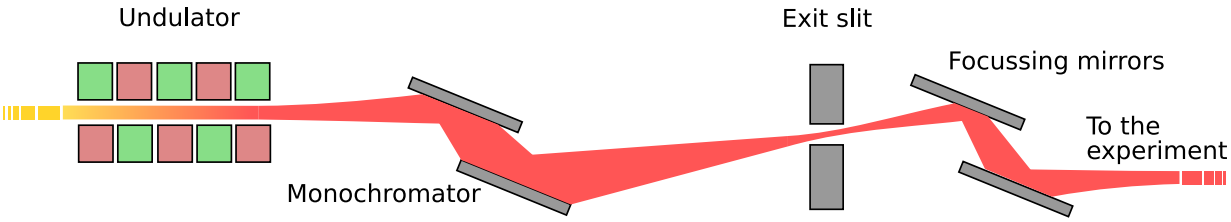

Figure 15: Simplified design of the p04 beamline. An electron beam of roughly $100\,\mathrm{mA}$ enters the undulator. The outgoing broadband synchrotron radiation is monochromatized and focused to the experimental set-up.

upper level discriminator (ULD). If an voltage higher than the ADC threshold enters the PHA device a measurement is triggered. The circuit determines the height of the amplitude and verifies whether it is within the range spread by the LLD and ULD. If true, the pulse height voltage is fed into an ADC circuit, which is used to assign the analog voltage to a digital channel. The TADC divides a $10\,\mathrm{V}$ range into 8192 channels.
Sampled voltage analysis mode. SVA can be used to digitize analog voltages between 0 and $10\,\mathrm{V}$. The voltage sampling is triggered by a TTL pulse fed into the ADC. SVA is used to monitor time dependent parameters, which usually provide an analog voltage as a measure (e.g. photon energy).
Time to digital converter. Another possible operation mode is TDC. It is used to measure the time difference of two digital pulses (START, STOP-pulses). This mode was not used in this experiment.

3.2.2 Detection of x-rays

For the energy resolved detection of photons emitted by the trapped HCIs a silicon drift detector (SDD) of the company KETEK is employed [45]. The principle of a SDD is similar to the semiconductor detector explained in section 2.4 but with a geometry optimized for maximal detection area and charge collection [46]. The SDD is welded onto a vacuum flange with its standard Be-window removed. This allows a close placement of the detector to the ion cloud, drastically increasing its solid angle. he Be-windows are usually employed to shield the detector from the intense low energy radiation, which can easily saturate the detector. The durability, which is obtained already with a few microns of beryllium, makes Be-windows a good choice for most experiments. However the poor transmission characteristics of Be-windows in the soft x-ray regime make

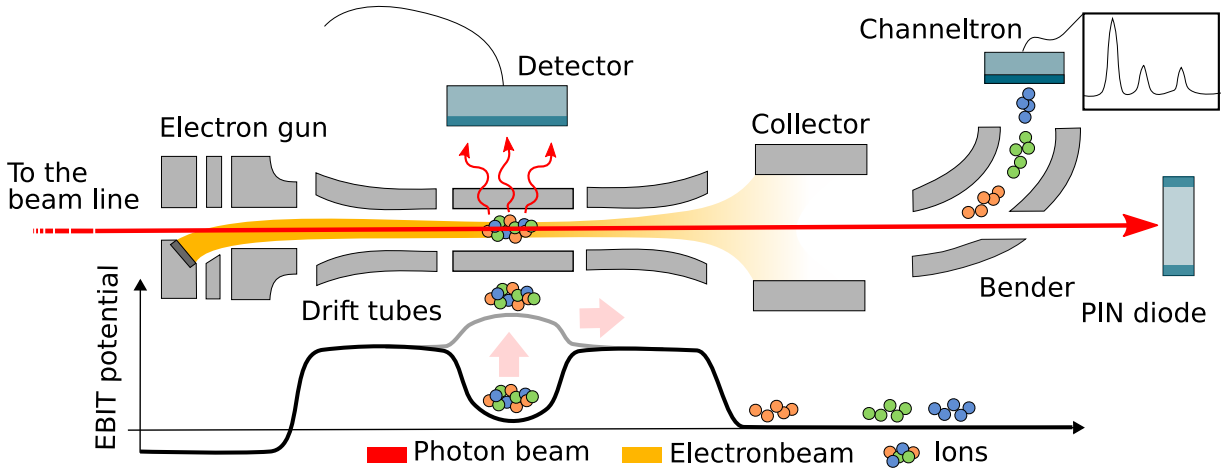

Figure 16: The measurement scheme. The photon beam is axially overlapped with electron beam. Ions guided by an electrostatic bender hit the channeltron at a q/m specific time of flight. The fluorescence is observed by an silicon drift detector.

its application not feasible for this work. Since the transmission characteristics of aluminium surpass those of the common tens of microns thick Be-windows in the soft x-ray regime, a $500\,\mathrm{nm}$ aluminium filter has been mounted in front of the SDD to block UV and visible light. A direct comparison of both transmission characteristics is visualized in figure 14.
The output of the internal preamplifier of the SDD is fed into a spectroscopy amplifier for further processing. PHA is then applied to digitize the output of the spectroscopy amplifier.

3.2.3 Detection of extracted ions

The the central drift tube (DT4, section 3.1) is connected to two high voltage power supplies. One applies an voltage $\mathrm{U_{inner}}$ to the central drift-tube to define the electron-beam energy at the interaction zone between the electron beam and the plasma. The other voltage $\mathrm{U_{kick}}$ is used to invert the trapping potential and extract the ions from the EBIT (see figure 16). Using a fast high voltage transistor switching between these voltage values in nanosecond timescales is possible [47]. To initiate a switch of the voltages, a TTL pulse produced by a function generator is fed to the input of the transistor. The acceleration voltage is then given by the difference between the voltage $\mathrm{U_{kick}}$ and the voltage applied on the extractor electrodes. After the ions transit the extraction beamline, the ion yield is measured using a channeltron. The output of the pre-amplifier, which is

connected to the channeltron, is fed directly to an oscilloscope.

3.3 PETRA III

The Positron-Elektron-Tandem-Ring-Anlage PETRA was initially constructed for particle physics research in the 1970s [48]. It is part of the german electron synchrotron facility DESY, which is located in Hamburg, Germany. PETRA was able to accelerate electrons and positrons up $19\,\mathrm{GeV}$, which also led to the discovery of the gluon in 1979 [49]. In the following decades, the PETRA accelerator was used as a pre-accelerator for HERA, a next generation particle accelerator. During that time PETRA was named PETRA II. In 2007 parts of PETRA II were reconstructed and equipped with 14 undulators, a device for efficient production of synchrotron radiation using permanent magnets. Since then PETRA III has been one of the most brilliant synchrotron radiation sources world wide.

3.3.1 P04 soft x-ray beamline

There are 25 beamlines installed at PETRA III, each beamline utilizes the high energy electron beam provided by the storage ring to produce unique photon beams, varying in energy as well as in characteristics optimized for various experiments. The P04 XUV-beamline (fig. 15), which was used for this work, offers an exceptionally high photon flux of more than 10^{12} photons per second in soft x-ray domain ($250\,\mathrm{eV} - 3000\,\mathrm{eV}$) [50]. The monochromator of P04 consists of a diffraction grating with variable line spacing (VGS) and an exit slit. The broadband photon beam, produced by the undulator, impinges on the grating at grazing incidence and is spatially dispersed. A selection of the outgoing photon-beam energy is achieved by the exit slit. Further x-ray optics of P04 allow a precise focusing of the beam to the experimentally desired position. In total a resolving power $E/\Delta E$, which is a measure for the energy distribution of the photons, of over 10000 can be obtained at P04. These parameters allow precision spectroscopy of highly charged ions of low to medium Z ions, where inter-shell transitions often lie in the provided energy spectrum.

3.4 The experimental measurement scheme

In the following section, the experimental measurement scheme is explained.
The method used to investigate individual electronic transitions of HCIs is laser spec-

troscopy. The highly monochromatic photon beam of the soft x-ray beamline P04 is used to resonantly excite HCIs produced by the PolarX-EBIT. The two fluorescence detectors record the number of photon-events for a given photon beam energy. Simultaneously the content of the trap is extracted and accelerated towards the extraction-beamline in constant time intervals. While the ions move with constant speed, the various charge states are separated according to their charge-to-mass ratio q/m. A channeltron mounted at the end of the extraction beamline is then used to measure the signal produced by the different ion charge stages (see figure 16).

4 Data analysis

4.1 Goal of the analysis

The goal of the measurement campaign was to resolve all transitions of the Fe^{13+} M-shell unresolved transition array (UTA). Due to the nature of multi-electron systems, excited levels in these systems usually exhibit significant autoionization channels comparable in strength and occasionally even dominating their competing radiative relaxation channels. The whole energy range of the Fe^{13+} M-shell UTA ($760\,eV$-$810\,eV$) has been measured in successive small energy ranges. For each scan, two data files were written by the data acquisition system: a list-file containing the fluorescence data and a log-file, which contains the data arrays of the photoionization signal.
The autoionization channel is observed as a decreasing Fe^{13+} ion yield, while simultaneously the Fe^{14+} ion yield increases. The first part of the analysis focuses on the determination of transition energies of all measured resonances. As a second part absolute autoionization and radiative transiton rates of two lines are determined, which were measured at a higher resolution. The method has been developed by René Steinbrügge during his Ph.D. thesis and was adapted for this thesis [51].

4.2 Fluorescence data

Fluorescence following the photo excitation of HCIs is detected by two SDDs. One is placed horizontally, the other is placed vertically in the plane perpendicular to the photon beam. For each monochromator energy, the SDDs record an one dimensional decay spectrum of the detected photons. That way, one obtains a two-dimensional spectrum for every scan and detector (see fig. 17). By projecting an appropriate region of interest to the x-axis, which corresponds to the monochromator energy, an one-dimensional fluorescence spectrum is obtained, in which the resonances can be characterized. Following the discussion in section 2.6, in which the emission characteristics are discussed for circularly polarized incident photons, it can be concluded that the fluorescence photons are emitted isotropically in the plane spanned by the two SDDs. Therefore, one can sum both one-dimensional spectra to increase the signal-to-noise ratio as well as the goodness of the fit.

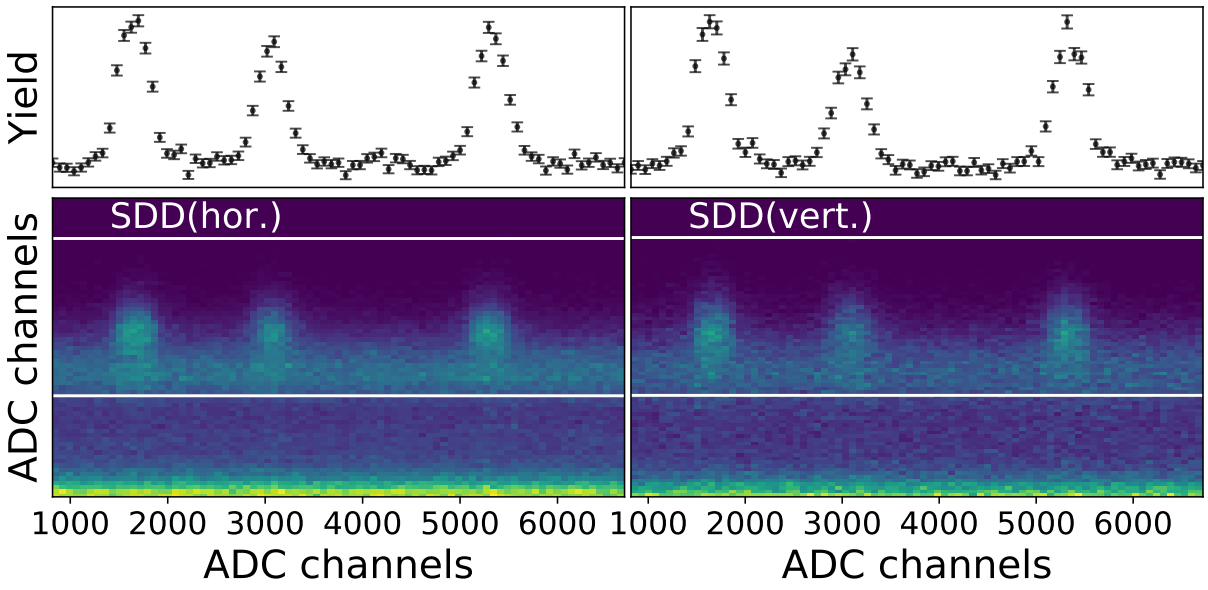

Figure 17: Comparison of two-dimensional spectra recorded with the mounted SDDs. The white lines indicate the region of interest (ROI) over which the integration takes place to obtain one dimensional projections (top).

4.3 Photoion data

After each step of the monochromator, a time-of-flight spectrum is recorded from which the charge-state distribution of ions is determined. By concatenating all spectra, a two-dimensional matrix can be formed (see fig. 19)). As has been explained in more detail in section 2.5, the arrival time of a specific ion at the ion detector depends on the chosen extraction voltage and its charge-to-mass ratio. To identify each peak one can relate the time of flight t_{tof}

$$t_{\mathrm{tof}} = \sqrt{\frac{s^2}{2U} \cdot \frac{m}{q}} + t_0 := A \cdot \sqrt{\frac{m}{q}} + t_0 \tag{43}$$

to a q/m ratio with the path length s, acceleration voltage U and the constant time-offset t_0. One can determine the parameters A and t_0 by an educated guess of two tof peaks. Equation 43 can then be used to identify other peaks in the tof spectrum (see fig. 18). If the masses of the abundant isotopes of the injected element are known, one can relate the charge-to-mass ratios directly to the charge states of the ions.

As one examines the two-dimensional tof-spectrum (figure 19), three dots with increased intensity can be seen. These occur all at the same time of flight, but for different monochro-

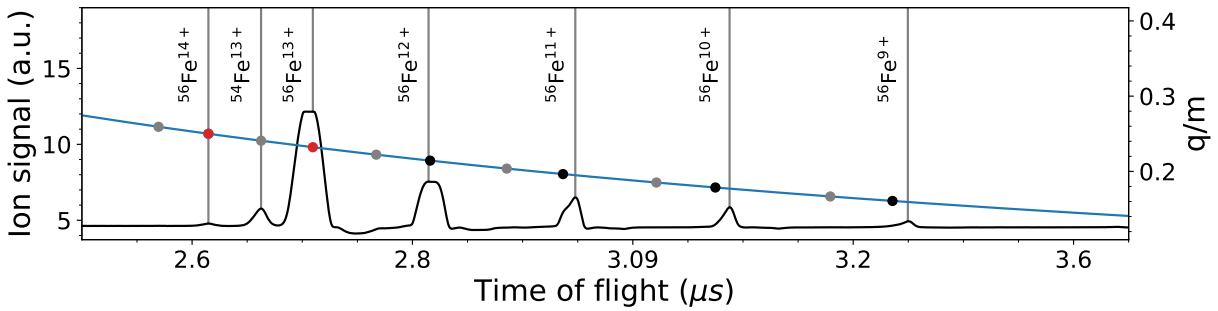

Figure 18: A time-of-flight spectrum of ions extracted from the trap. Each observed peak corresponds to a charge state of iron. The blue line depicts the charge to mass ratio as a function of the time of flight of the ions, which has been calculated using the experimental positions of the Fe^{13+} and Fe^{14+} peaks (red dots). The gray and black dots mark the position of the charge states of $^{56}\mathrm{Fe}$ and $^{54}\mathrm{Fe}$ isotopes.

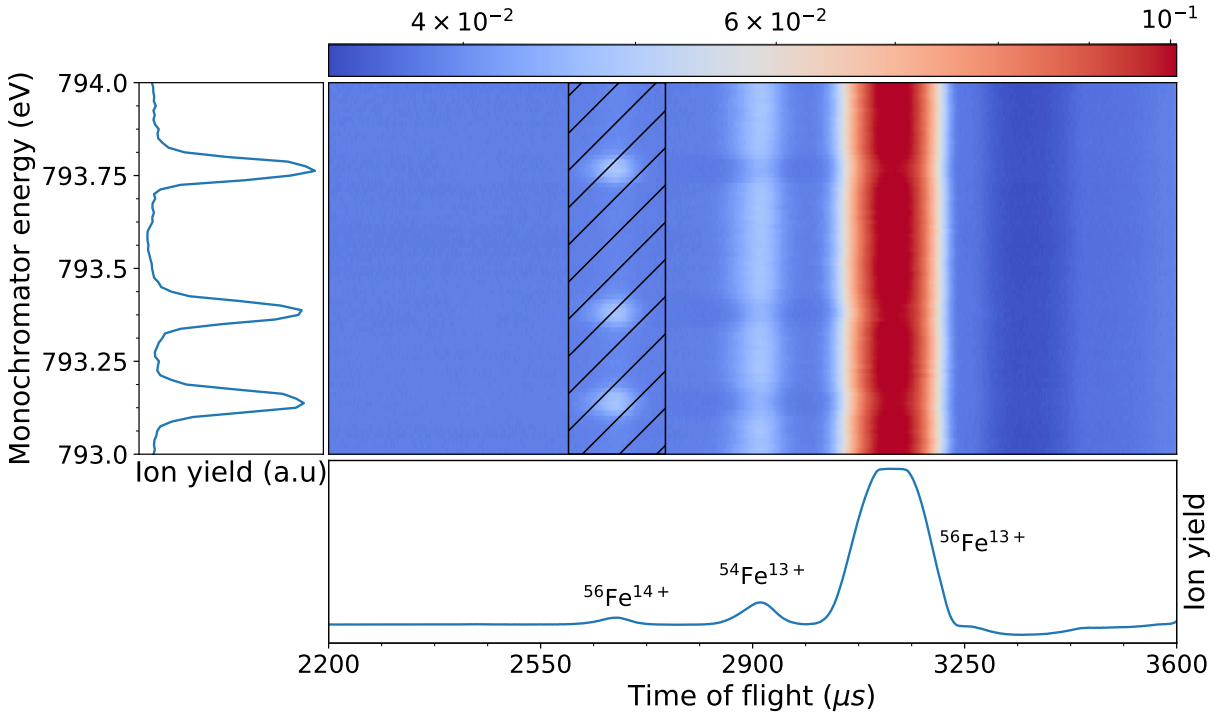

Figure 19: Center: The tof spectra which are recorded after each step of the scan are combined to one two-dimensional spectrum. The color intensity corresponds to the ion yield. The projection of the data to the x-axis yields a tof-spectrum with three distinct peaks. Each peak corresponds to a q/m value. A projection of the ROI onto the energy axis reveals three resonances.

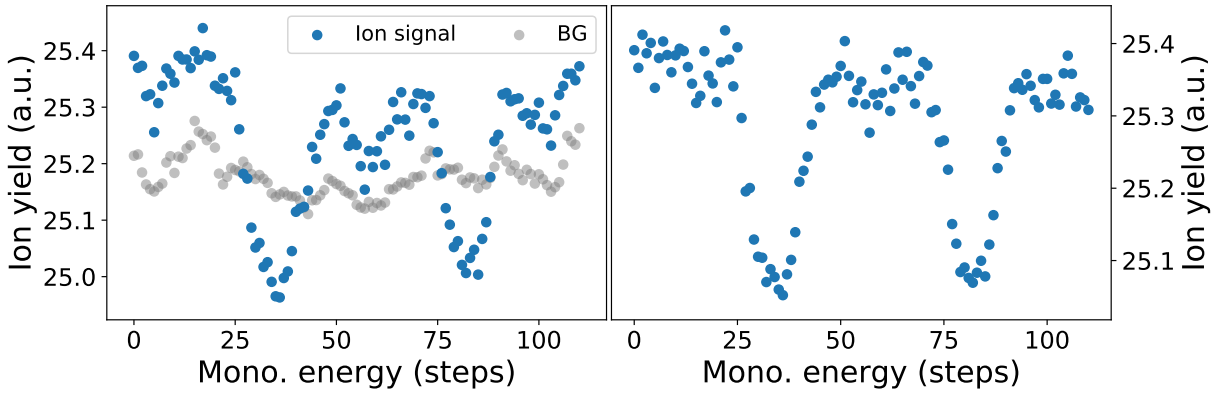

Figure 20: Ion-yield spectrum of Fe^{13+}. The raw ion signal (blue dots, left figure) is affected by the electronic noise, which can be seen on the baseline of the ToF-signal (grey). By normalizing the signal a „clean"signal is obtained (right figure).

mator energies. An one dimensional energy spectrum can be obtained by choosing a ROI (shaded rectangle in figure 19) and project its content to the monochromator-energy axis. These peaks correspond to the same resonances, which can be seen in the fluorescence spectrum but are additionally resolved in their charge state. Using equation 43, these resonances can be directly related to the Fe^{14+} charge state. What is being observed here is the increase in Fe^{14+} ions due to the Auger process, which transfers parts of the Fe^{13+} population to the Fe^{14+} population. The reason why this is only observed for specific photon energies is that Fe^{13+} must be first excited to a higher level, which happens only at specific photon energies. This assumption is strengthened by the fact that the predicted decrease in Fe^{13+} is also observable (see fig. 20 left).

During data analysis, it became clear that the off-resonance ion yield exhibited an energy dependent variation (fig. 20 grey dots). The origin of this variation of the background can be attributed to noise in the electronics, used for data acquisition. Since no significant correlation between the background spectrum and the resonances in the ion-yield spectrum could be determined, the background spectrum has been used to normalize the ion yield. The resulting spectrum is depicted in figure 20. By applying a non-linear least squares fit of multiple Gaussians, the centroids, amplitudes and the widths of the resonances can be obtained.

For the above mentioned method of extracting one-dimensional spectra, the estimation of the error on each data point is not trivial. In contrast to the fluorescence signal, where the Poisson statistics can be used to estimate the error as the square root of the number

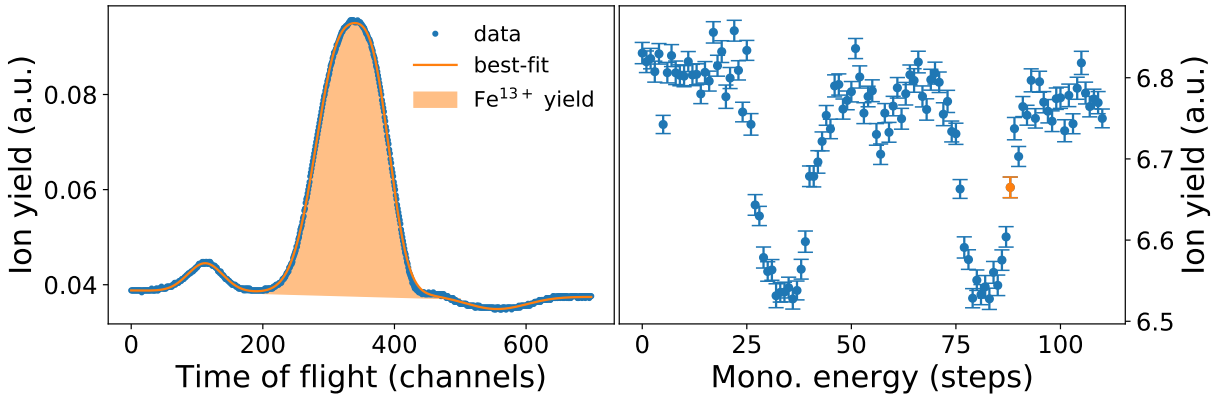

Figure 21: Left: Section of tof-spectrum. Right: Fe^{13+} ion-yield spectrum. Each data point in the right figure has been obtained by determining the area under the tof-signal the Fe^{13+} signal. The statistical uncertainty resulting from the fit is used as the error for the data point for the spectrum on the right side.

of events, this method relies on a voltage measurement, which is proportional to the number of ions. In the following, we use a different approach. Instead of choosing a ROI and projecting its content on the photon-energy axis, each tof-spectrum is modeled separately by multiple Gaussians. The area within one tof-peak and its statistical uncertainty is then used as a data point and its estimated error within the one dimensional ion-yield spectrum (fig. 21). While the initial approach showed a strong correlation between the fit-results and the choice of ROI, this method turned out to not exhibit such a systematic effect.

4.4 Calibration of the monochromator energy axis

During data acquisition, the nominal photonbeam energies, which were given by the P04 control system have been used to set the energy ranges for the measurement. But for the actual analysis these values are known to be quite inaccurate ($\pm \approx 100\,\mathrm{meV}$). To ensure proper calibration of the energy axis for the final analysis, one can use well known transitions of simpler systems, for which theory and experiments are in good agreement. For that reason several $1s \longrightarrow np$ transitions of He-like oxygen and neon and H-like oxygen have been measured besides the transition array. He-like systems are preferable due to the large abundance in the produced plasma and the high accuracy with which the transition energies are predicted by theory [52].

To facilitate a proper calibration, lines of higher order Rydberg series (K_ζ to K_κ) of

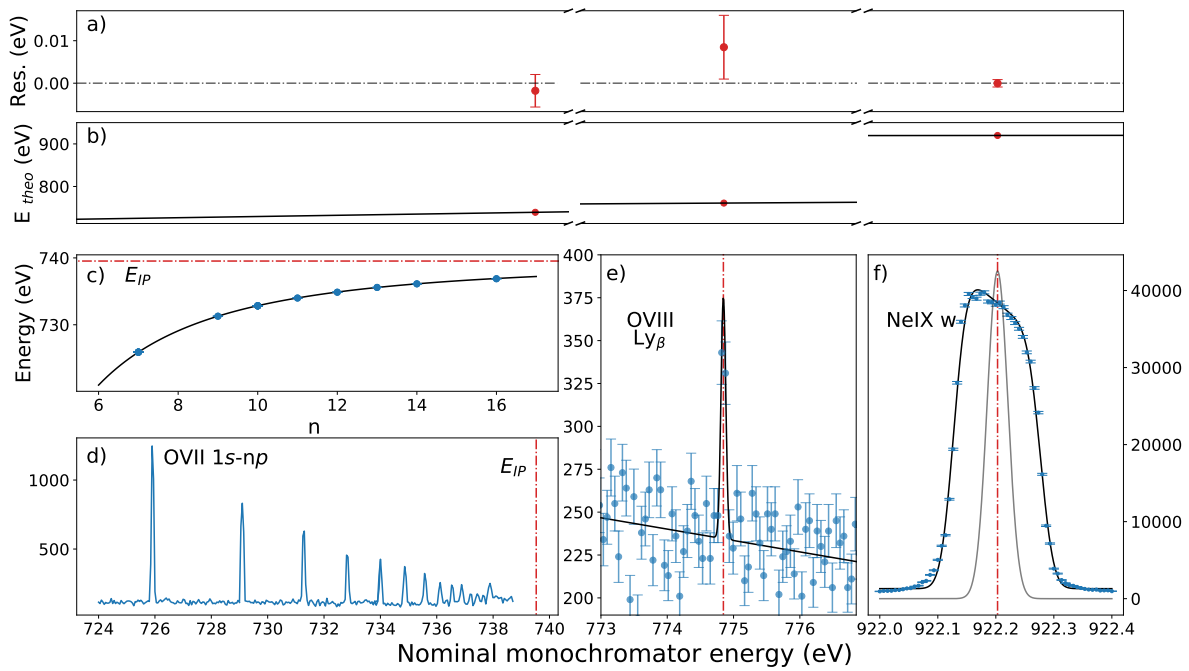

Figure 22: b) The linear calibration curve for the nominal monochromator energy. The residuals are given in a). The datapoints are extracted from the spectra below. d) Spectra of He-like oxygen Rydberg series, e) Lyβ of oxygen and f) w of He-like Neon. The Gaussian profile in f) results from the model, which was used to describe the asymmetric line shape. The w and Lyβ resonances are theoretically determined to very high accuracy and can be used to calibrate the energy axis. c) As an additional point on the calibration curve the ionization potential is determined for OVII. The experimental transition energies determined from b) are given as a function of the principal quantum number n of the upper state of the corresponding transition. The ionization potential is then extracted as the asymptote.

He-like oxygen, Lyβ of H-like oxygen and $1s \longrightarrow 2p$ (w) of He-like Neon have been measured (see fig. 22). Due to the high countrate, one can see that the measured line shape of Ne w is asymmetric. It can be assumed that the large exit-slit, chosen for this single measurement, lead to a misalignment of the photonbeam to the center of the slit. Resulting in a not uniformly illuminated exit-slit. This could explain the observed asymmetric instrument profile. As a consequence the usual approximation of a Gaussian profile does not hold. To obtain the centroid of the measured signal the observed profile has been modeled by a skewed slit function convoluted with Gaussian profile.

The transition energy, which corresponds to the centroid of the convoluted Gaussian, has been determined as $E(\mathrm{Ne_w}) = 922.2030(9)\,\mathrm{eV}$.
Theoretical values for the measured high-order Rydberg series transitions (figure 22 d) are not available. To realize a comparison with theory, the ionization potential has been determined using the available measurements. As can be seen in figure 22 c) the experimentally determined nominal transition energies are plotted over the principal quantum number of the excited state. Using these data points, it is possible to determine the ionization potential of He-like O. A quantum-defect model based on the Rydberg formula is used, with the Rydberg energy E_R, the effective nuclear charge Z_eff and the quantum defect $\delta_{n,l}$ for principal n and orbital quantum number l, respectively:

$$\begin{aligned} E_n &= Z_\mathrm{eff}^2 E_\mathrm{R} \left[(1-\delta_{1,s})^{-2} - (n-\delta_{n,l})^{-2}\right] \\ &= E_\mathrm{IP} - Z_\mathrm{eff}^2 E_\mathrm{R} (n-\delta_{n,l})^{-2}. \end{aligned} \tag{44}$$

To reduce uncertainty, results of a previous measurement done in 2019 will be included in the following analysis. During that beamtime a dedicated measurement of the He-like oxygen rydberg series has been conducted. Z_eff and $\delta_{n,l}$ have been fixed by implementing the results of that measurement [52]. Using this model, the ionization potential has been determined as $E_\mathrm{IP} = 739.5298(38)\,\mathrm{eV}$.
Another data point on the calibration curve has been obtained by the measurement of the Neon Lyβ line at approximately $775\,\mathrm{eV}$. Usually the observation of fluorescence of photoexcited H-like ions in an EBIT is difficult. Since the electron beam energy, necessary to produce H-like ions is larger than the energy of the photon beam, the observed signal is dominated by background produced by direct electron-impact excitation. To circumvent this problem a method has been applied, which allows background-reduced measurement of such systems by implementing a two-part measurement process. During a „breeding time“, a significant amount of H-like ions are produced. After accumulation of H-like ions the electron beam energy is switched instantly down to a value below the ionization threshold. The following „detection time“is then used to record the fluorescence [43].
Such a measurement procedure has been used to record a signal of the $\mathrm{Ly}\beta$ transition of H-like oxygen (see figure 22 e)). Due to limited time, only a weak signal could be observed. However the present statistics allowed a determination of the line centroid with a reasonable accuracy of $E(\mathrm{Ly}\beta) = 774.8469(75)\,\mathrm{eV}$.
By comparing the nominal experimental transition energies with their theoretical coun-

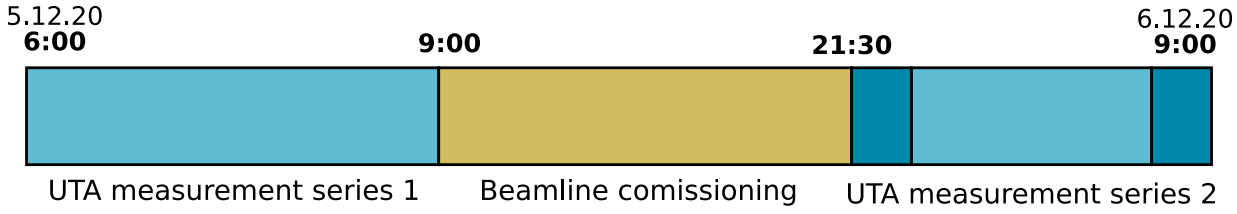

Figure 23: Time schedule of the whole UTA measurement campaign. UTA lines were measured in two measurement series (blue) interrupted by a day of beamline comissioning (yellow). During the second measurement series calibration lines (dark blue) but also several UTA lines were measured.

terpart a calibration curve can be obtained (figure 22 a), b)). The linear fit revealed a constant offset of nominal energies by $214(22)\,\mathrm{meV}$ with a slope of $0.99998(2)$.

Additionally to the calibration curve, an analysis of possible systematic errors must be conducted.

Energy drifts in time. The UTA measurement series was split into two parts conducted over two days (see fig. 23). The two measurement series were interrupted by half a day of beamline commissioning. Although the hutches of the photon beamline are temperature stabilized, slight shifts in temperature over the day can lead to measurable drifts of the nominal energy. Since 12 hours passed in between both UTA measurement series, but also a lot of beamline-parameter changes happened during commissioning, it was not unlikely that significant changes in the nominal energies occurred.

To investigate this assumption, the transition energies of UTA lines, which were scanned during both UTA measurement series are subtracted and plotted in figure 24. The weighted average of

$$\Delta E_{\mathrm{mean}} = 0.0006(26)\,\mathrm{eV}. \tag{45}$$

has been determined. Considering that this value is compatible to a value of zero, it is neglected in further analysis.

It can be also concluded, that the calibration lines obtained during UTA measurement series 2 can in fact be used to calibrate the nominal photon energies of the day before, if the error of ΔE_{mean} is included in the final error budget.

Encoder interpolation error. Another known source of uncertainty arises from the encoder of the P04 monochromator. In principle any requested photon energy corre-

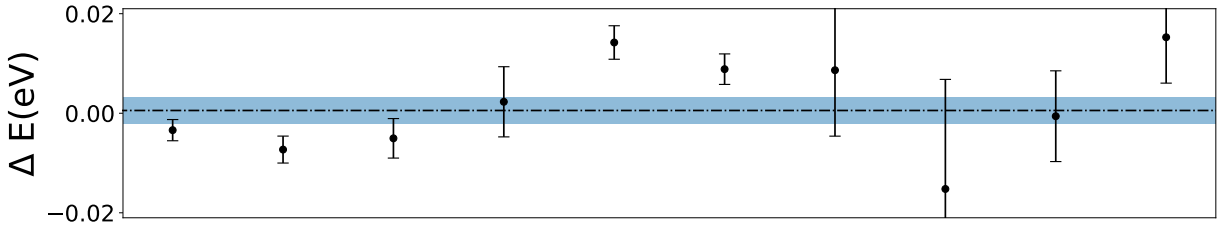

Figure 24: The difference of nominal transition energies of same lines acquired during measurement series 1 and measurement series 2 after approximately 12 hours is plotted. The weighted average (blue line) and its 1-sigma uncertainty(shaded) has been determined to test if nominal energies have changed. The weighted average has been determined by applying a linear fit with a fixed slope of zero.

sponds to an angle of the mirrors and grating placed inside the monochromator of the P04 beamline. If changes in energy are required, the necessary change in the involved angles are calculated and set accordingly. However this process has practical limits. A requested change of e.g. $10\,\mathrm{meV}$ (as in this experiment) would correspond to a rotation in the order of 10^{-5} degrees, which is significantly less than the reference marks on the angular encoder. Interpolation functions are used to set such small changes in angles. Previous experiments have shown that these interpolation functions are highly unreliable, resulting in fluctuations in the energy for given nominal values [43].
As a result, the relatively large error of ΔE_{mean} might be caused by the encoder. However a definitive answer can not be given within the framework of this thesis.

4.5 Line identification

To proceed further, one has to identify the experimentally observed lines, i.e. which initial and excited electronic levels correspond to each resonance. This assignment was done by comparing the experimental spectra with simulated spectra. For that purpose, we use relativistic MBPT calculations of Ming Feng Gu for the transition energies and rates [53]. A comprehensive list of all theoretical lines can be found in appendix 6.2. The theoretical spectrum can be produced by summing multiple Gaussian profiles, where the center is determined by the theoretical transition energy and its amplitude by the radiative transition rate, weighted by the branching ratio, $A_\gamma \cdot B_i$. The index i determines the decay channel (radiative, auger). The width of the Gaussian is tuned to match the

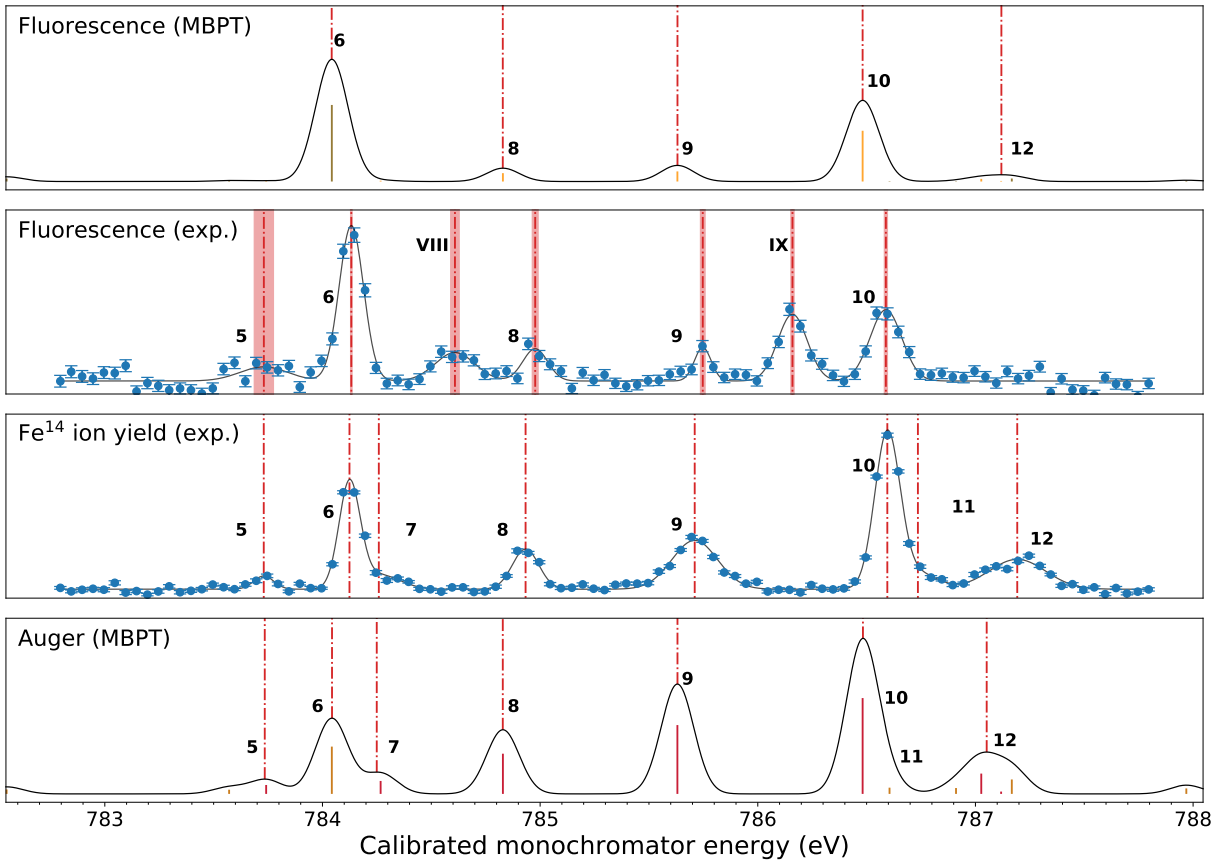

Figure 25: Comparison of experimental and theoretical spectra. Experimental and theoretical transition energies are given as red lines. The shaded area mark the 1 sigma uncertainty. Theoretical lines are convoluted with gaussian profiles to simulate the experimental resolution.

experimental observation. Figure 25 depicts such theoretical spectra and experimental spectra for a small part of the UTA. In order to save space, only part of the UTA is shown in detail. Further close-up spectra are listed in the appendix (chapter 6.1). Any line observed in the ion-yield spectra can be directly associated to the UTA of Fe^{13+}. Since most resonances in the UTA are expected to have an auger-decay channel comparable or stronger than the respective radiative channel, the ion-yield spectra are used to assign the experimentally observed lines to their theoretical counterparts. One can see that most measured transitions can be associated with a single line in the theoretical spectra. This enables us to determine the coupling structure for each identified line. The results are given in table 2. For highly blended lines, where multiple resonances are

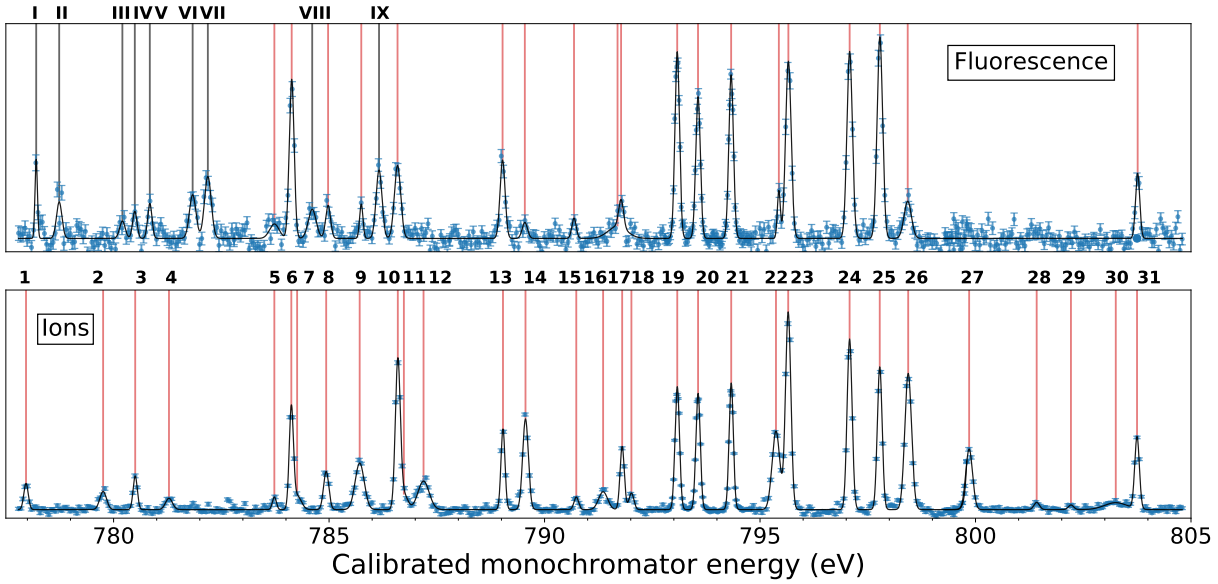

Figure 26: Overview of all experimentally determined lines. Top: Fluorescence spectrum. Bottom: Ion-yield spectrum. Lines observed in the ion-yield spectrum can be directly related to the Fe^{13+} UTA. Each identified line is labelled with a number (same as in table 2). Several lines, which were observed in the fluorescence spectrum, can be excluded from the Fe^{13+} UTA (labeled with roman numerals), since no corresponding signal could be observed in the ion-yield spectrum.

merged into one structure (e.g. line 12), a comparison is done with the maximum of the theoretical spectrum. These values are given in table 2 under the column „Blend“.

As can be seen in figure 25, some lines observed in the fluorescence spectrum cannot be associated with a line in the theoretical spectrum. One can reason that these lines are not part of the UTA produced by Fe^{13+} ion. Since these unidentified lines are mostly located in the lower energy part of the spectrum (fig. 26), it can be assumed that they are produced by a lower charge state of iron (i.e. Fe^{12+}, Fe^{11+}). Due to the lack of high precision theoretical calculations, it has not been possible to verify this assumption yet.

A comparison of the calculated to the experimental energies is shown in figure 27. To quantify the experimental result, the calibrated theoretical transition energies are subtracted from the experimental energies to determine the residual for all measured UTA lines. A weighted average of

$$E_{\text{res}} = 79.6(67)\,\text{meV}. \tag{46}$$

was found. There are two possible explanations for this deviation. An unknown sys-

Table 2: Comparison of experimentally determined transition energies of the Fe^{13+} M-shell UTA. Each idetified line is labelled with a number given in column one. The next two columns contain the centroid values and the corresponding statistical uncertainty. Column three contains the peak position of the theoretical spectrum. These values are more suitable for the comparison of highly blended lines. The remaining columns give the theoretical energies, the groundstate (GRD: $^2P_{1/2}$, META: $^2P_{3/2}$) and the excited level structure (column four and five). The energies are given in eV.

No.	Exp. (eV)	Error (eV)	Blend (eV)	Theory (eV)	Init	Term	J
1	777.968	0.006	777.9037	777.9037	META	$((2p^5 3s^2 3p)^3D\ 3d)\ ^4D$	5/2
2	779.757	0.009	779.7430	779.7486	GRD	$((2p^5 3s^2 3p)^3D\ 3d)\ ^4F$	3/2
3	780.502	0.003	780.3400	780.3996	META	$((2p^5 3s^2 3p)^3P\ 3d)\ ^4D$	5/2
4	781.285	0.015	781.1981	781.1507	GRD	$(((2p^5 3s)^3P\ 3p^3)\ ^4S_3)\ ^4P$	1/2
				781.2329	META	$((2p^5 3s^2 3p)\ ^3S\ 3d)\ ^2D$	3/2
5	783.730	0.016	783.7364	783.5711	GRD	$((2p^5 3s^2 3p)\ ^3S\ 3d)\ ^2D$	3/2
				783.7413	META	$((2p^5 3s^2 3p)\ ^3P\ 3d)\ ^4P$	1/2
6	784.124	0.003	784.0439	784.0430	GRD	$((2p^5 3s^2 3p)\ ^1D\ 3d)\ ^2P$	1/2
7	784.259	0.097	784.2614	784.2672	META	$(((2p^5 3s)\ ^3P\ 3p^3)\ ^2P_1)\ 2D$	3/2
8	784.933	0.005	784.8285	784.8290	META	$(((2p^5 3s)\ 3P\ 3p^3)\ ^2D3)\ ^2D$	3/2
9	785.710	0.006	785.6311	785.6307	META	$(((2p^5 3s)\ 3P\ 3p^3)\ ^4S3)\ ^2P$	3/2
10	786.595	0.005	786.4832	786.4817	META	$((2p^5 3s^2 3p)\ ^1P\ 3d)\ ^2D$	5/2
11	787.192	0.011		786.6053	GRD	$(((2p^5 3s)\ ^3P\ 3p^3)\ ^2P1)\ ^2D$	3/2
12	787.192	0.011	787.0457	786.9108	GRD	$(((2p^5 3s)\ ^3P\ 3p^3)\ ^4S3)\ ^2P$	1/2
				787.0268	META	$((2p^5 3s^2 3p)\ ^3P\ 3d)\ ^4P$	1/2
				787.1671	GRD	$(((2p^5 3s)\ ^3P\ 3p^3)\ ^2D3)\ ^2D$	3/2
13	789.036	0.002	788.9195	788.9197	META	$((2p^5 3s^2 3p)\ ^3P\ 3d)\ ^2D$	5/2
14	789.558	0.002	789.4640	789.4561	GRD	$((2p^5 3s^2 3p)\ ^3D\ 3d)\ ^4F$	3/2
				789.4922	META	$(((2p^5 3s)\ ^3P\ 3p^3)^2P_1)\ ^2S$	1/2

Table 3: cont.

No.	Exp.	Error	Blend	Theory	Init.	Term	J
15	790.736	0.013	790.7331	790.7438	META	$((2p^5 3s^2 3p)\ ^1D\ 3d)\ ^2F$	5/2
16	791.359	0.012	791.2957	791.2951	GRD	$((2p^5 3s^2 3p)\ ^3D\ 3d)\ ^4D$	3/2
17	791.801	0.003	791.7637	791.7580	META	$((2p^5 3s^2 3p)\ ^3P\ 3d)\ ^4P$	5/2
18	792.015	0.011	791.9363	791.9431	GRD	$((2p^5 3s^2 3p)\ ^1P\ 3d)\ ^2P$	3/2
19	793.079	0.001	793.0176	792.8987	META	$((2p^5 3s^2 3p)\ ^3D\ 3d)\ ^2D$	3/2
				793.0194	GRD	$((2p^5 3s^2 3p)\ ^3P\ 3d)\ ^2D$	3/2
20	793.562	0.001	793.4833	793.4835	META	$((2p^5 3s^2 3p)\ ^1D\ 3d)\ ^2D$	5/2
21	794.331	0.001	794.2693	794.2692	GRD	$((2p^5 3s^2 3p)\ ^3D\ 3d)\ ^4F$	3/2
22	795.370	0.005	795.2370	795.2368	GRD	$((2p^5 3s^2 3p)\ ^3D\ 3d)\ ^2D$	3/2
23	795.654	0.002	795.5415	795.5416	META	$((2p^5 3s^2 3p)\ ^1D\ 3d)\ ^2P$	3/2
24	797.078	0.002	796.9937	796.9935	GRD	$((2p^5 3s^2 3p)\ ^1P\ 3d)\ ^2P$	1/2
25	797.778	0.002	797.6282	797.6275	META	$((2p^5 3s^2 3p)\ ^3D\ 3d)\ ^2S$	1/2
26	798.438	0.002	798.3693	798.3686	META	$((2p^5 3s^2 3p)\ ^1S\ 3d)\ ^2D$	5/2
27	799.852	0.002	799.7929	799.7928	META	$((2p^5 3s^2 3p)\ ^3P\ 3d)\ ^2D$	3/2
28	801.419	0.014	801.3430	801.3434	META	$((2p^5 3s^2 3p)\ ^3D\ 3d)\ ^2P$	1/2
29	802.214	0.022	802.1305	802.1310	META	$((2p^5 3s^2 3p)\ ^3P\ 3d)\ ^2D$	3/2
30	803.255	0.034	803.2466	803.2460	META	$((2p^5 3s^2 3p)\ ^1S\ 3d)\ ^2D$	5/2
31	803.748	0.001	803.6822	803.6815	GRD	$((2p^5 3s^2 3p)\ ^3D\ 3d)\ ^2P$	1/2

Table 4: cont.

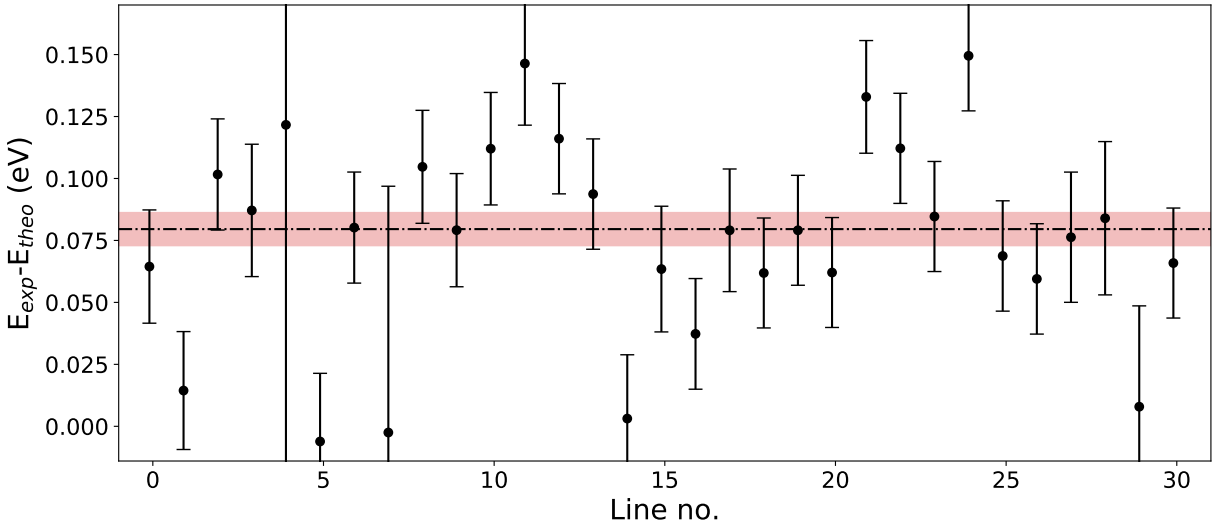

Figure 27: The theoretical transition energies are subtracted from their corresponding experimental values. The systematic errors and the statistical error are added in quadrature and used as weights for the data points. The horizontal line indicate the weighted average and the shaded area its statistical uncertainty.

tematic effect in the experiment or an offset in theoretically calculated transition energies. Since the experimental transition energies were calibrated using theory, one must again assume an offset in theory. Since the three theoretical values, which are used for the calibration are benchmarked to experiments, or stem from simple systems, where high deviations are unlikely, one can conclude that the $79.6(67)\,\mathrm{meV}$ deviation comes from the theory. A simple answer to the cause of the deviation in the calculated transition energies is difficult to provide, but one explanation could be a systematically lower groundstate energy, possibly due to insufficient amount of input-configurations.

4.6 High-resolution scan

During the campaign most scans were measured with an exit slit of $100\,\mu\mathrm{m}$. The resulting energy resolution is not sufficient to resolve the natural linewidths of the UTA lines, which are in the order of $\approx 10\,\mathrm{meV}$. However one part of the transition array containing the lines 19 and 20 (tab:2) was measured with a higher resolution, employing an exit slit of $25\,\mu\mathrm{m}$. The increased resolution allows a determination of the natural linewidth. In the following section, we will utilize this single spectrum to obtain the absolute radiative and autoionization rates of the two observed lines. The method has been developed

Table 5: The coupling structure (in jj-notation) and statistical weights of the two lines, analysed in this chapter 4.6.

No	Label	Initial	Excited	g (circ. pol)
19	Line 1	$3p_{1/2}$	$[[2p_{1/2}3p_{3/2}]_1 3d_{3/2}]_{3/2}$	2
20	Line 2	$3p_{3/2}$	$[[2p_{1/2}3p_{3/2}]_2 3d_{5/2}]_{5/2}$	4

by René Steinbrügge [51][54] and has been adapted for this work.

4.6.1 Extraction of absolute transition rates

There are multiple unknown variables (number of ions, detection efficiency, overlap factor of photon beam with ions, etc.) involved in this measurement so that absolute values are challenging to determine and one usually has to rely on theoretical values. The idea of this procedure is to gain four independent equations out of which the four transition rates $A_{\gamma,1}, A_{\gamma,2}, A_{A,1}, A_{A,2}$, can be calculated. The two lines, from now on referred to as „line 1"and „line 2", are both $2p \longrightarrow 3d$ transitions within the Fe^{13+} M-shell UTA. The following sections illustrate how absolute transition rates can be determined from ratios of experimental values and the natural linewidth of line 1 and line 2.

4.6.2 The parameter c; the ratio of yields

The (baseline subtracted) signal yields (fluorescence: Y_γ, Ions: Y_A) that are observed with the detectors are proportional to the initial rate of excitation $\sigma N_{ion} N_\gamma$, the branching ratio B, the number of photons in the photon beam and the detector specific detection efficiency P. For both detection methods we can formulate equations for the experimental yields

$$Y_\gamma = B_\gamma \sigma N_{ion} N_\gamma P_\gamma, \tag{47}$$

$$Y_A = B_A \sigma N_{ion} N_\gamma P_A. \tag{48}$$

A value independent of the initial excitation process can be gained, by taking the ratio of both yields for the same transition

$$c' := \frac{Y_\gamma}{Y_A} = \frac{B_\gamma}{B_A} \cdot \frac{P_\gamma}{P_A}. \tag{49}$$

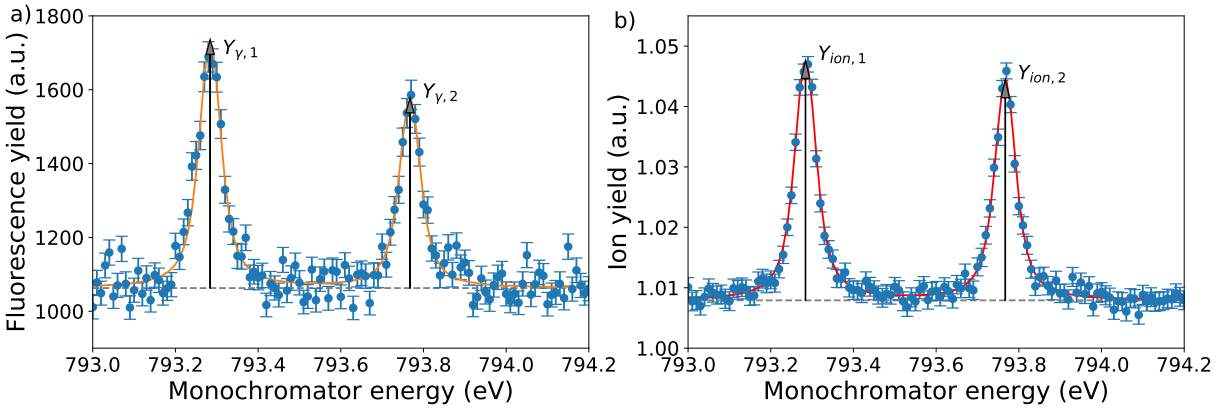

Figure 28: The photon yield and the ion yield of the two transitions can be determined by modeling a Voigt profile to the data. a): Fluorescence, b): Ions.

Additionally the detection efficiencies P_γ and P_A are in general unknown factors, which contribute to a large systematic uncertainty. So instead of determining these values directly we define a parameter c as the ratio of c' for two different transitions of the same charge state. This parameter is then independent of the detection efficiencies:

$$c := \frac{c'_1}{c'_2} = \frac{B_{\gamma,1} \cdot B_{A,2}}{B_{\gamma,2} \cdot B_{A,1}} = \frac{A_{\gamma,1} \cdot A_{A,2}}{A_{\gamma,2} \cdot A_{A,1}} \tag{50}$$

By measuring the four experimental yields $Y_{\gamma,1}, Y_{\gamma,2}, Y_{A,1}, Y_{A,2}$, a value purely dependent on the Einstein coefficients can be gained. The yields can be determined by modelling the experimental spectrum with Voigt profiles (fig. 28). Inserting the values from the fit into equation 70 we end up with

$$c = 1.203 \pm 0.095. \tag{51}$$

4.6.3 The parameter d; linestrength ratio

Another parameter, which can be extracted from the same spectra is the line strength. Experimentally it corresponds to the integral over the normalized signal:

$$S_{exp} = \int \frac{Y(E)}{N_\gamma(E) \cdot N_{Ion}(E)} dE = B \cdot P \int \sigma(E) dE = B \cdot P \cdot S = B \cdot P \cdot \frac{g_2}{g_1} \frac{hc^2}{8\pi\nu^2} \cdot A. \tag{52}$$

Since the line strength can be determined for both the fluorescence spectrum and the ion spectrum, the indices have been omitted from the above equation. As can be seen in equation 52 the yield has to be normalized by the photon flux and the number of ions.

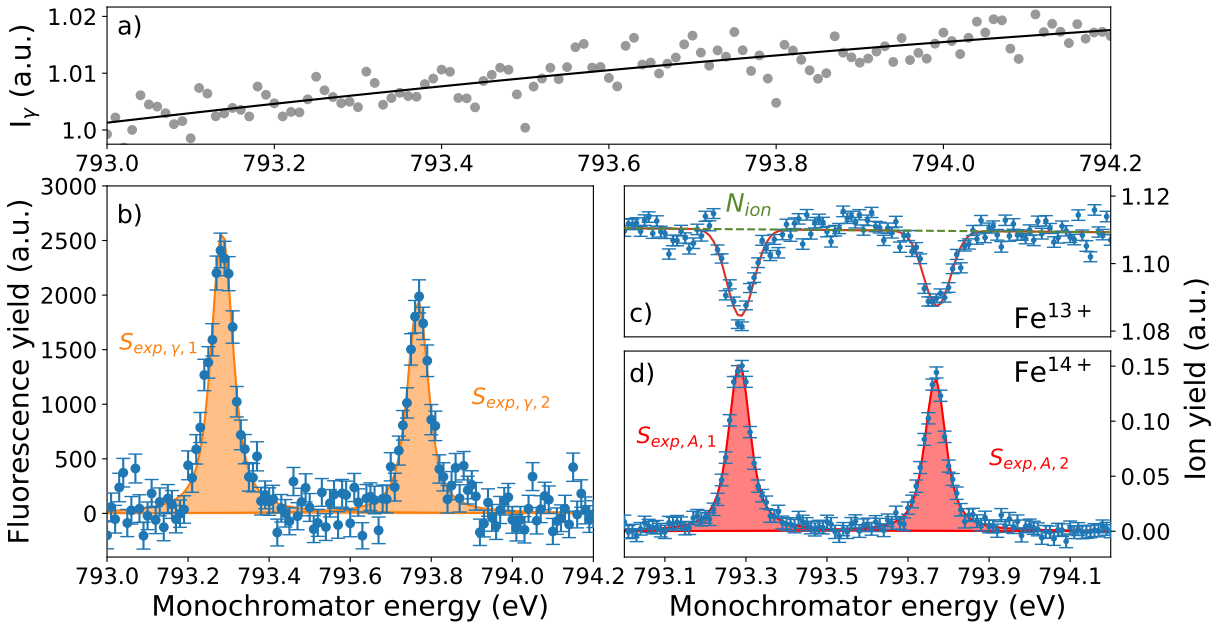

Figure 29: The experimental data must be normalized by the photon current (a) and the ion yield (c) before linestrength is extracted from the data. b): Fluorescence, d): Ions.

To determine the photon flux the experiment is set up with a diode down stream of the experiment, where the photon beam intensity is converted to a measurable electrical current. Since this diode current I_γ is proportional to the photon flux N_γ, one can use it for normalization (see fig. 29a). The number of ions depend for the most part on the electron beam energy and electron beam current. Since the electron beam current can be affected easily by environmental variables like pressure and vibrations, it is known to have fluctuations over time and therefore it depends also on the photon energy. Here we estimate N_{ion} as the baseline of the Fe^{13+} ion yield (see fig.29c). To get rid of the detection specific efficiency P in equation 52, the ratio of experimental line strength of both lines is determined:

$$d_\gamma = \frac{S_{exp,\gamma,1}}{S_{exp,\gamma,2}} = \frac{A^2_{\gamma,1}}{A^2_{\gamma,2}} \cdot \frac{A_{tot,2}}{A_{tot,1}} \cdot \frac{E_2^2}{E_1^2} \cdot \frac{g_{22}}{g_{21}}, \tag{53}$$

$$d_A = \frac{S_{exp,A,1}}{S_{exp,A,2}} = \frac{A_{\gamma,1}A_{A,1}}{A_{\gamma,2}A_{A,2}} \cdot \frac{A_{tot,2}}{A_{tot,1}} \cdot \frac{E_2^2}{E_1^2} \cdot \frac{g_{22}}{g_{21}} \tag{54}$$

with the transition energy E_i, and statistical weight for the initial state $g_{i,1}$ and the excited state $g_{i,2}$. After the fluorescence and ion yields have been normalized, the fit results

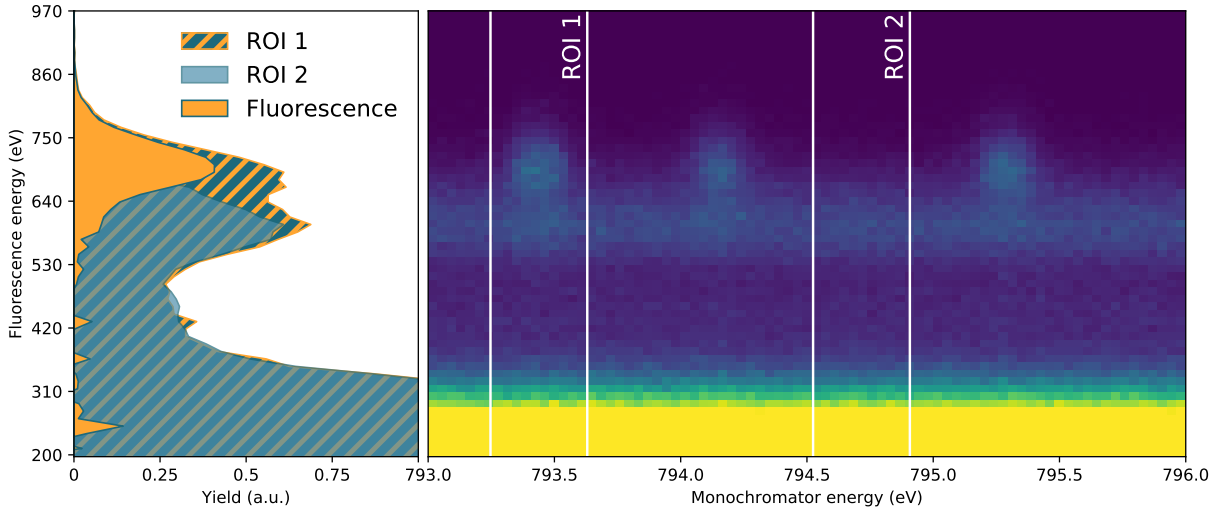

Figure 30: Extraction of decay spectra. ROI 1 (fluorescence signal) and ROI2 (background) are projected individually on the fluorescence energy axis. By subtracting the projected spectra from each other one obtains the decay spectrum.

can be inserted in above equations to obtain the two d parameters:

$$d_\gamma = 1.367 \pm 0.068,\ d_A = 1.136 \pm 0.041. \tag{55}$$

4.6.4 The natural linewidth

The natural linewidth γ can be determined from the same fit as in fig. 29. All four resonances have been fitted as a single data set, sharing the Gaussian width for all lines. As a result, the natural linewidths γ_1 and γ_2 have been determined as

$$\gamma_1 = 23.12\,\mathrm{meV} \pm 1.59\,\mathrm{meV},\ \gamma_2 = 22.07\,\mathrm{meV} \pm 1.67\,\mathrm{meV}. \tag{56}$$

The theoretical linewidths calculated by Gu et al are given for comparison below.

$$\gamma_{1,\mathrm{theo}} = 57.022\,\mathrm{meV},\ \gamma_{2,\mathrm{theo}} = 82.88\,\mathrm{meV}. \tag{57}$$

The natural linewidth is in direct relation with the total transition rate

$$A_{tot} = \sum_i (A_{\gamma i} + A_{Ai}) = \frac{\gamma}{\hbar}, \tag{58}$$

which includes all radiative and non-radiative channels. Therefore the natural linewidth is an essential parameter, which will be used to determine the total radiative and autoionization rates A_γ and A_A.

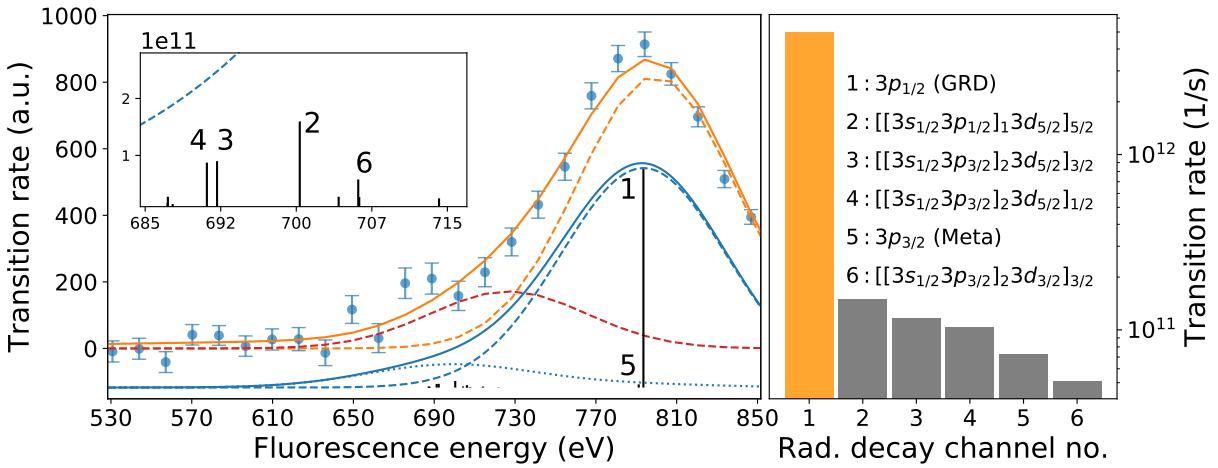

Figure 31: Result of the radiative BR analysis for line 1. Left: The various radiative decay channels for the excited state are shown in an artificial spectrum (blue and black lines) The experimental decay spectrum has been fitted to determine the subsidiary decay cluster (red dotted line). The theoretical spectrum is shifted vertically. Right: Theoretical radiative transition rates are plotted in a bar diagram for the most prominent decay channels.

4.6.5 The influence of other decay channels

So far it has been assumed that there is only one radiative and one non-radiative decay channel for the excited state. Which means that the branching ratios to the groundstate

$$B_\gamma^0 = \frac{A_\gamma^0}{\sum_j A_\gamma^j}, \; B_A^0 = \frac{A_A^0}{\sum_j A_A^j} \tag{59}$$

are both equal to one. In general there are other states to which the excited state can decay. This leads to a possible underestimation of the experimental yield and linestrength. To determine the influence of other radiative decay channels, the decay spectra of the investigated lines have to be analysed. As can be seen in fig. 30, the pure fluorescence signal can be extracted by choosing two ROIs. One contains the fluorescence signal (ROI 1) and the other contains only the background signal (ROI 2). By subtracting ROI 1 from ROI 2 one is left with a pure decay spectrum produced by fluorescence photons. Due to the insufficient resolution of the SDD ($60\,\mathrm{eV}$ FWHM), the subsidiary decay channels appear as a single unresolved feature. To determine the relative strength of the main decay channel, the spectrum has been fitted by a model consisting of two Gaussians (fig. 31 orange and red dashed lines) and a Sigmoid. The dominant Gaussian

profile corresponds to the main decay channel. All other subsidiary decay channels have been included in the smaller Gaussian profile. The Sigmoid is used to model the response function of the detector. As a result one can estimate the branching ratios to the groundstate as:

$$B^0_{\gamma,1,exp} = 0.8266\,(7),\ B^0_{\gamma,2,exp} = 0.8254\,(6). \tag{60}$$

This parameter shows that approximately $83\,\%$ of the whole integrated signal corresponds to photons of transitions to the groundstate.
To check if this simple model can be reproduced by theory an artificial decay spectrum has been modeled for comparison (fig. 31 blue). For both transitions of interest we determine all theoretical radiative decay channels. Decay channels with non-negligible transition rates are to excited levels of the ground state configuration. As can be seen in figure 31 most of them lie approximately $100\,\mathrm{eV}$ below the main decay channel. The theoretical branching ratios have been determined to be

$$B^0_{\gamma,1,theo} = 0.892,\ B^0_{\gamma,2,theo} = 0.910. \tag{61}$$

Other transition branching ratios have been tabulated in table 6. Since the experimentally determined radiative branching ratio is in fact the unperturbed branching ratio weighted by the corresponding photon distributions, which explains the apparent deviation between $B^0_{\gamma,theo}$ and $B^0_{\gamma,exp}$. For further analysis the theoretical values for the branching ratio will be used. This result has to be included into the d parameter. The actual experimental line strength is then given by

$$S'_{exp,\gamma} = S_{exp,\gamma} \cdot B^0_\gamma, \tag{62}$$

$$S'_{exp,A} = S_{exp,A} \cdot B^0_\gamma. \tag{63}$$

The above modification of the linestrength introduces the radiative branching ratio into the parameter d_γ and d_A:

$$d_\gamma = \frac{S'_{exp,\gamma,1}}{S'_{exp,\gamma,2}} \cdot \frac{B^0_{\gamma,2}}{B^0_{\gamma,1}}, \tag{64}$$

$$d_A = \frac{S'_{exp,A,1}}{S'_{exp,A,2}} \cdot \frac{B^0_{\gamma,2}}{B^0_{\gamma,1}}. \tag{65}$$

As mentioned above, the radiative transitions to states other than the ground state could not be resolved in the experimental spectrum, determining d_γ and d_A with only experimental data is for that reason not possible.

Table 6: For the two lines of interest the involved angular momenta, anisotropy parameter β, theoretical transitions rate and the radiative branching ratio are tabulated for the six most significant decay channels.

	Line 1						Line 2					
No.	J_0	J_i	J_f	β	$A_{\gamma,FAC}$	B_γ	J_0	J_i	J_f	β	$A_{\gamma,FAC}$	B_γ
1	1/2	3/2	1/2	-1/2	5.3e12	0.892	3/2	5/2	3/2	-7/25	6.8e12	0.910
2			5/2	-1/10	1.6e11	0.027			3/2	-7/25	1.5e11	0.020
3			3/2	2/5	9.0e10	0.015			5/2	8/25	1.2e11	0.016
4			1/2	-1/2	8.7e10	0.015			7/2	-1/10	1.0e11	0.013
5			3/2	2/5	7.6e10	0.013			7/2	-1/10	7.3e10	0.010
6			3/2	2/5	5.8e10	0.010			3/2	8/25	5.1e10	0.007

4.6.6 The influence of the angular distribution of emitted photons

Another factor, which has to be analysed in detail is the angular distribution of photons. The effect of polarisation on the observed signal strength can be strong, since it can even lead to complete cancellation if the detector is placed at a „wrong"position. In this experiment the incoming photons were circularly polarized. Therefore the angular distribution is isotropic in the plane perpendicular to the photon beam axis. This allows the summation of both detector signals into one spectrum. While the enhanced signal leads to a more accurate determination of all involved fit-parameters, it has a disadvantage that one cannot access the information regarding the angular momenta of the subsidiary decay channels. Since the excited states decay to states with various total angular momenta, the angular distribution for the various channels have to be superimposed

$$W(\theta,\phi) = \sum_i B_\gamma^i W^i(\theta,\phi). \tag{66}$$

The above equation can then be calculated using the values in table 6 and equation 35. Since for circular polarisation the photons are emitted isotropically for given angle θ, the above equation reduces to a single number for each line:

$$W_1 = 0.8626,\ W_2 = 0.9122. \tag{67}$$

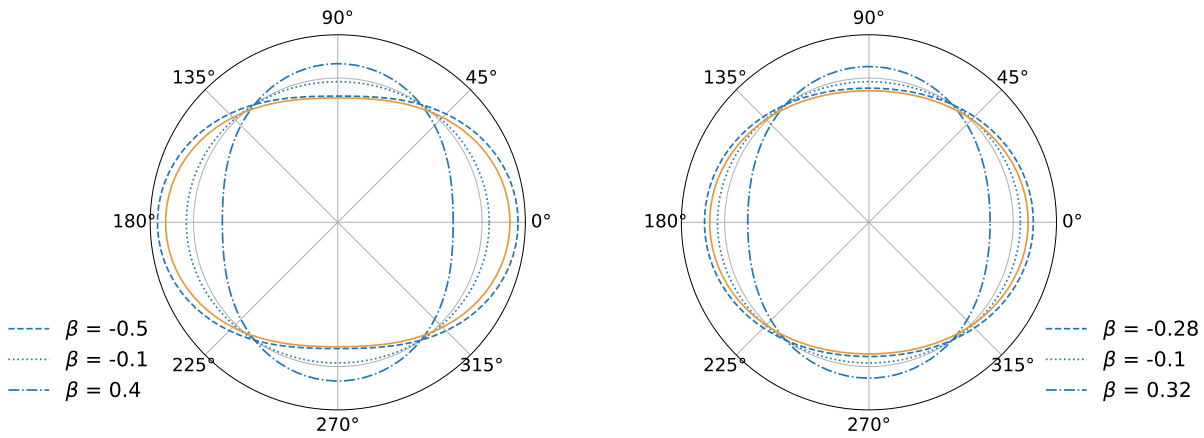

Figure 32: Modulus of the angular distribution in a polar representation. For both lines of interest the theoretical angular distribution for all major decay channels have been visualized (blue lines). Including the theoretical branching ratios, a weighted sum has been calculated (yellow).

The effect of the superimposed angular distributions is visualized in figure 32. Since each transition has a different angular distribution, the detection efficiency of the fluorescence detector is transition dependent.

$$P'_{\gamma,1} = P_\gamma \cdot W_1 \tag{68}$$

$$P'_{\gamma,2} = P_\gamma \cdot W_2. \tag{69}$$

As a result the c and d parameters must be modified correspondingly

$$c = \frac{Y_{\gamma,1} \cdot Y_{A,2}}{Y_{A,1} \cdot Y_{\gamma,2}} \cdot \frac{W_2}{W_1} \tag{70}$$

$$d_\gamma = \frac{S'_{exp,\gamma,1}}{S'_{exp,\gamma,2}} \cdot \frac{B^0_{\gamma,2}}{B^0_{\gamma,1}} \cdot \frac{W_2}{W_1} \tag{71}$$

$$d_A = \frac{S'_{exp,A,1}}{S'_{exp,A,2}} \cdot \frac{B^0_{\gamma,2}}{B^0_{\gamma,1}}. \tag{72}$$

By inserting the $B^0_{\gamma,1}$, $B^0_{\gamma,2}$,W_1,W_2 into the equations above, the corrected values for the c and d parameters can be gained:

$$c = 1.139 \pm 0.090,\ d_\gamma = 1.295 \pm 0.039,\ d_A = 1.136 \pm 0.041. \tag{73}$$

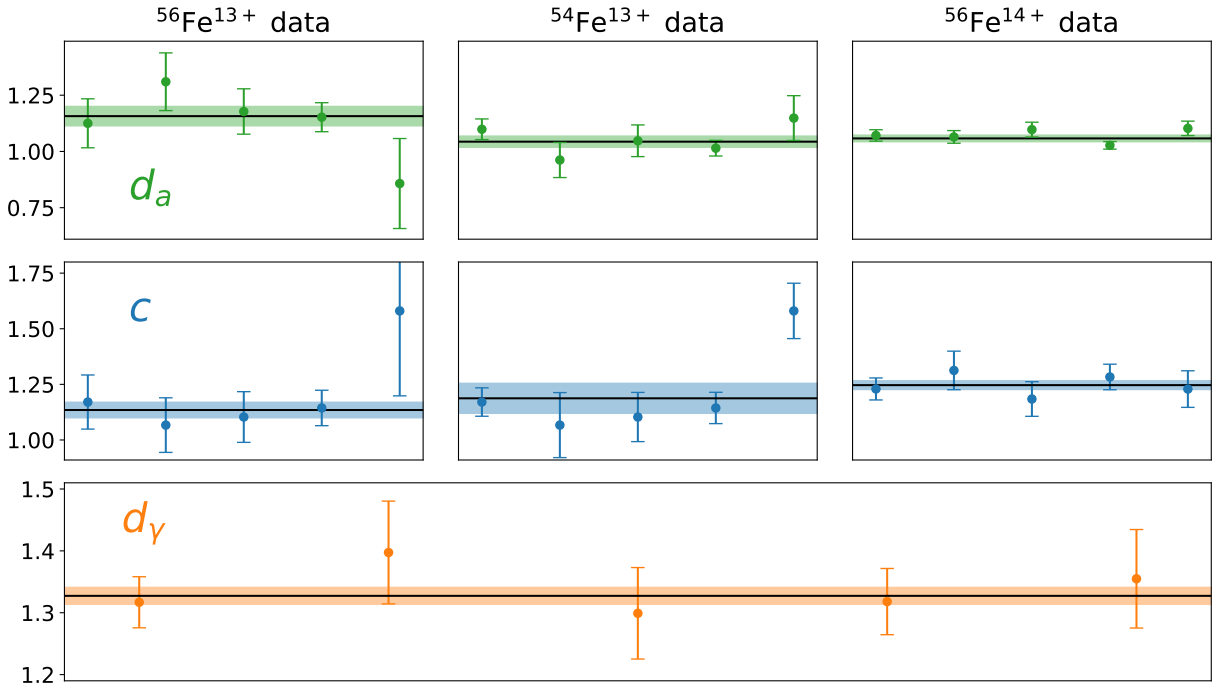

Figure 33: Four additional measurements of the same lines have been used to decrease uncertainty of the parameters c, d_A and d_γ. Furthermore the ion yield spectra of $^{56}\mathrm{Fe}^{13+}$ and $^{54}\mathrm{Fe}^{13+}$ are added. A weighted average has been determined for each data set. The results are condensed in table 7.

4.6.7 Putting everything together

While only one scan has been conducted with enhanced resolution to obtain the natural linewidth, one can use other „low“resolution scans of the lines 1 and 2 to decrease the uncertainty of c, d_γ and d_A. Additionally to the $^{56}\mathrm{Fe}^{14+}$ ion yield spectra, the ion yield spectra produced by $^{56}\mathrm{Fe}^{13+}$ and $^{54}\mathrm{Fe}^{13+}$ have been used. For each set of data the d_A and c parameters have been calculated and a weighted average determined (see figure 33 and table 7). Since the datasets are independent a weighted average could be calculated. Now that the parameters c, d_γ ,d_A and γ_1, γ_2 are available, it is possible to derive the four transition rates $A_{\gamma,1}, A_{\gamma,2}, A_{A,1}, A_{A,2}$. Before the rates are determined, a. quick discussion of the nature of this equation system will be done.
There are five experimentally determined equations and four rates to determine. It can be shown that $\{d_\gamma, d_A, c\}$ are not independent of each other, since by taking the ratio of

Table 7: The weighted averages and their errors for the three parameters c, d_A and d_γ (see fig. 33). The weighted average over all data sets is given in the bottom row.

	d_A	c	d_γ
$Fe^{13+}(Z=56)$	1.157(43)	1.135(35)	-
$Fe^{13+}(Z=54)$	1.043(25)	1.187(68)	-
$Fe^{14+}(Z=56)$	1.058(15)	1.247(20)	-
Average:	1.060(12)	1.210(25)	1.327(14)

d_γ and d_A the parameter c is gained.

$$\frac{d_\gamma}{d_A} = \frac{A_{\gamma,2}A_{A,2}}{A_{\gamma,1}A_{A,1}} \cdot \frac{A_{\gamma,1}^2}{A_{\gamma,2}^2} = \frac{A_{\gamma,1}A_{A,2}}{A_{\gamma,2}A_{A,1}} = c \tag{74}$$

Only four independent parameters are necessary to determine all transition rates, therefore three different sets of experimental parameters can be used to calculate the rates. Which are: $\{d_\gamma, c, A_{tot,1}, A_{tot,2}\}$, $\{d_A, c, A_{tot,1}, A_{tot,2}\}$, $\{d_\gamma, d_A, A_{tot,1}, A_{tot,2}\}$. It will be shown that the choice of the parameter set has an effect on the rates and especially on their uncertainties.

4.6.8 Parameter set 1: $\{d_\gamma, c, A_{tot,1}, A_{tot,2}\}$

By combining equations for d_γ (eq.71), c (eq.70) and the two total transition rates $A_{tot,1}$, $A_{tot,2}$ (eq.58) the four transition rates of interest can be determined.

$$A_{A,1} = A_{tot,1} - A_{\gamma,1} \tag{75}$$

$$A_{A,2} = A_{tot,2} - A_{\gamma,2} \tag{76}$$

$$A_{\gamma,1} = \left(c \cdot A_{tot,1} - \sqrt{A_{tot,1}A_{tot,2}\frac{g_{2,2}}{g_{2,1}}\frac{g_{1,1}}{g_{1,2}} \cdot d_\gamma} \cdot \frac{E_1}{E_2} \right) / (c-1) \tag{77}$$

$$A_{\gamma,2} = A_{\gamma,1}\frac{E_2}{E_1} / \sqrt{\frac{A_{tot,1}}{A_{tot,2}}\frac{g_{2,2}}{g_{2,1}}\frac{g_{1,1}}{g_{1,2}}d_\gamma} \tag{78}$$

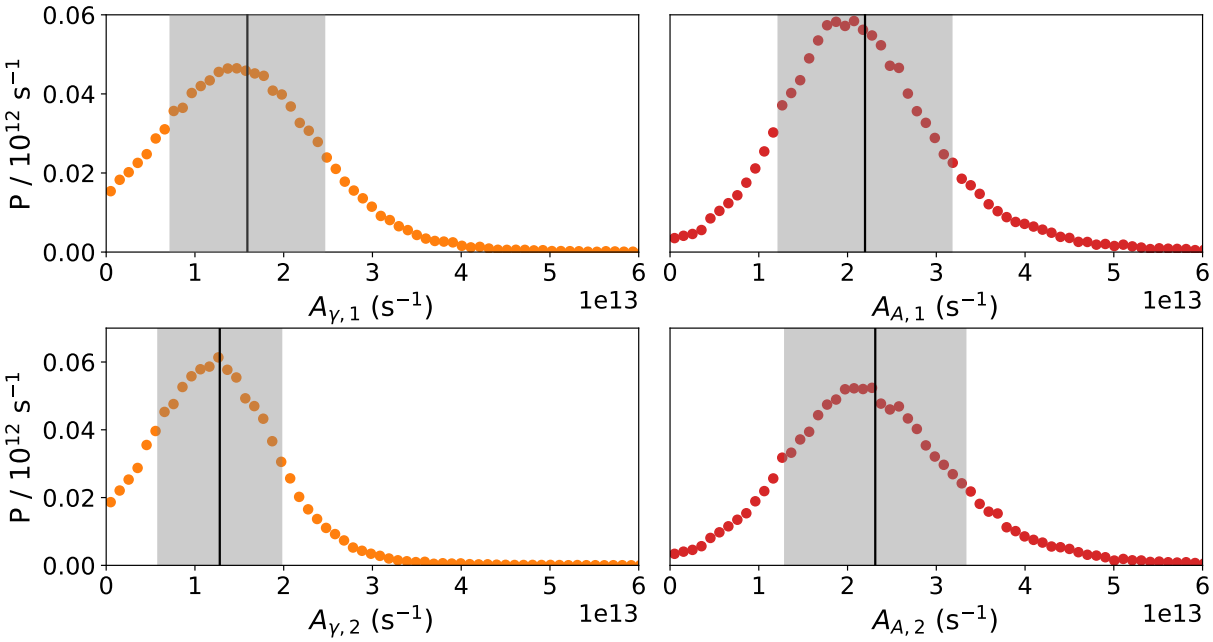

Figure 34: **Parameter set 1:**. Probability distribution for the four transition rates. The black line indicates the expectation value, the grey shaded area the 1-sigma interval.

A Monte-Carlo-like procedure is used to determine the probability distribution of the transition rates. For example to determine the distribution for A_γ, we produce a set of input parameters $\{ c', d', A'_{tot,1}, A'_{tot,2}, E'_1, E'_2 \}$. Each dashed parameter x' is an element of $\{ x - 3 \cdot x_{err}, ..., x + 3 \cdot x_{err} \}$. The probability that x' is drawn is normally distributed with the sigma given as x_{err}. Now for a large enough number of times A_γ is calculated with randomly chosen sets of parameters. Since negative values for the transition rates are physically impossible, an additional condition is set to prevent the calculation of such. The result is then visualized as a histogram (figure 34). The expectation value and the corresponding 1-sigma interval are marked by the black lines and shaded area, respectively.

However taking equation 74 into account, one can expect a strong correlation between the d parameters and c. A common way to quantify the strength of correlation is by using the Pearson correlation coefficient. It is given by the covariance of two parameters divided by the product of their standard deviations, resulting in a number between $[-1, 1]$. A more visual interpretation of the correlation between two variables can be gained by plotting a set of points e.g. (d'_γ,c'), with d'_γ and c' being an element of a normally distributed set with sigma given by $d'_{\gamma err}$ and c'_{err}. In such a depiction, the

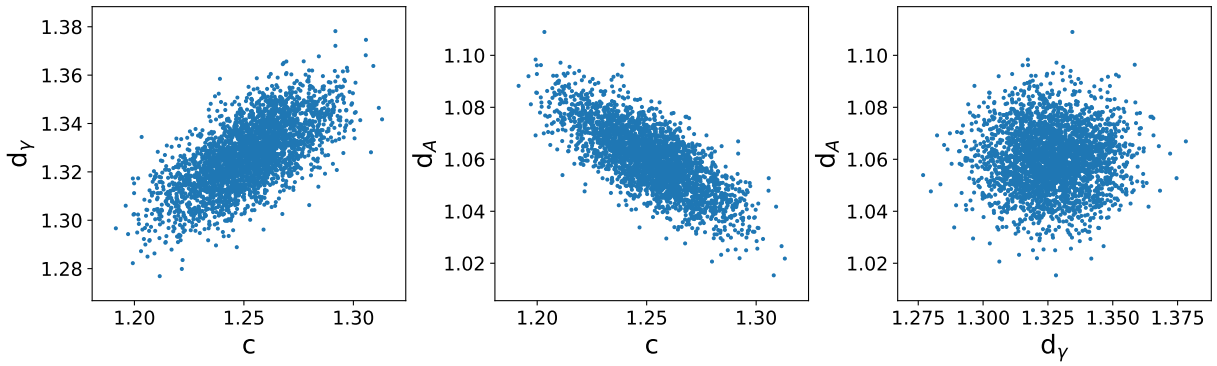

Figure 35: The strength of correlation is depicted for the three possible combinations of the parameters d_γ, d_A and c. Due to the relation between the d and c parameters a strong correlation can be observed in the first two figures. The statistical independence of d_γ and d_A can be seen in the last figure.

correlation can be estimated on the basis of the shape of the data. A correlation of zero corresponds to a cicle, strong correlation is depicted by a thin line at an angle of 45 degrees. The plotted data is visualized in figure 35. It can be seen, that the parameters d_γ and d_A are statistically independent. For that reason, a significantly lower uncertainty is expected for the third parameter set. This assumption will be tested in the following sections.

4.6.9 Parameter set 2: $\{d_A, c, A_{tot,1}, A_{tot,2}\}$

Instead of d_γ the linestrength ratio of the ion yields d_A is used to determine the four rates:

$$A_{\gamma,1} = A_{tot,1} - A_{A,1} \tag{79}$$

$$A_{\gamma,2} = A_{tot,2} - A_{A,2} \tag{80}$$

$$A_{A,2} = \left(cA_{tot,2} - \sqrt{A_{tot,1}A_{tot,2}\frac{g_{2,1}}{g_{2,2}}\frac{g_{1,2}}{g_{1,1}}\cdot\frac{c}{d_A}}\cdot\frac{E_2}{E_1}\right)/(c-1) \tag{81}$$

$$A_{A,1} = A_{A,2}\cdot\frac{E_1}{E_2}\cdot\sqrt{\frac{d_A}{c}\frac{A_{tot,1}}{A_{tot,2}}\frac{g_{2,2}}{g_{2,1}}\frac{g_{1,1}}{g_{1,2}}} \tag{82}$$

Utilizing the same procedure, as described in section 4.6.8, the probability distributions are calculated (see figure 36).

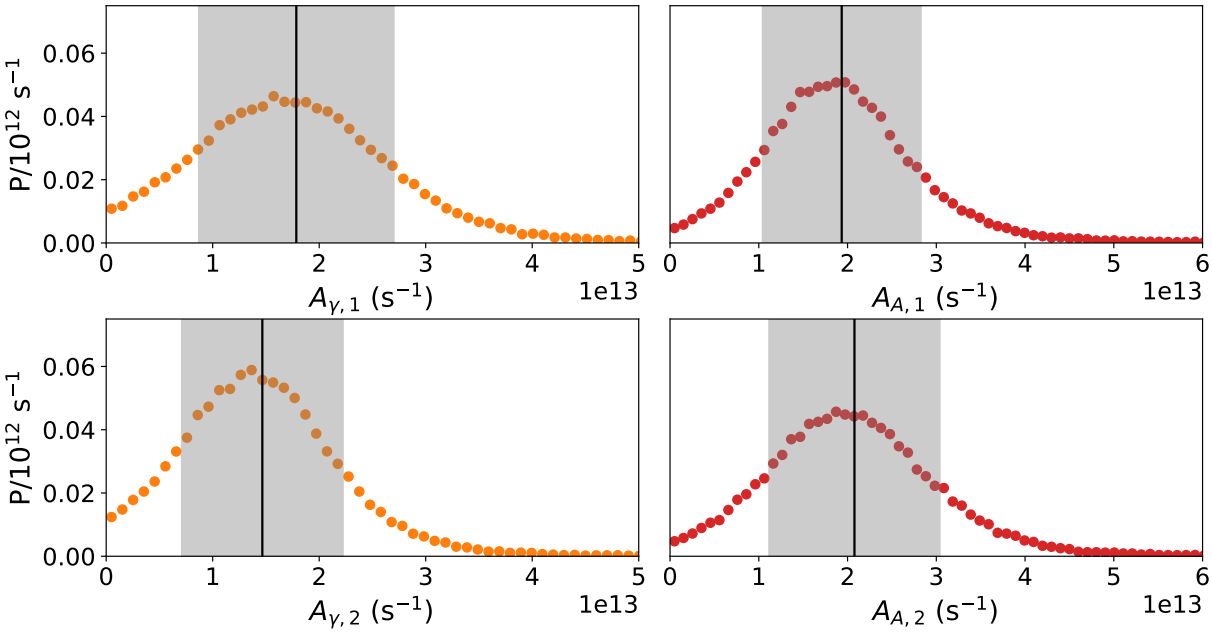

Figure 36: **Parameter set 2:** Probability distribution for the four transition rates. The black line indicates the expectation value, the grey shaded area the 1-sigma interval.

4.6.10 Parameter set 3: $\{d_A, d_\gamma, A_{tot,1}, A_{tot,2}\}$

By using equation 74 we can replace the c parameter with the ratio of d_γ and d_A. The equation system of section 4.6.8 is used to determine the probability distributions (figure 37)).

The four transition rates obtained from three different parameter sets have been summarized in table 8. While all results are in agreement with each other, a gradual decrease in uncertainty can be observed with the choice of parameter set. As expected, due to the low correlation between the d parameters, parameter set 3 exhibits a low relative uncertainty of approximately 30% (figure 37). As already mentioned, the calculations of Gu [53] predict natural linewidths of $57.0\,\mathrm{meV}$ and $82.9\,\mathrm{meV}$ for the lines 1 and line 2. The radiative branching ratios are also given as $B_{rad,1} = 0.123$ and $B_{rad,2} = 0.082$, leading to the rates given by $A_i^{\mathrm{theo}} = \frac{\Gamma}{\hbar} \cdot B_i$. The resulting theoretical rates are summarized in table 8.

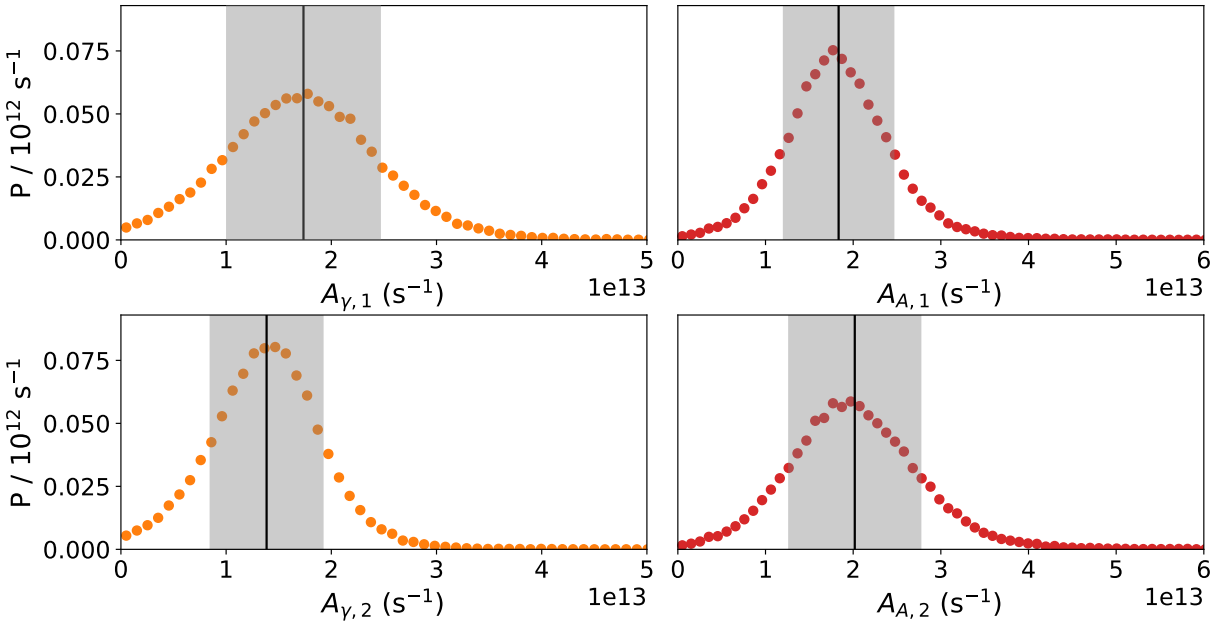

Figure 37: **Parameter set 3:** Probability distribution for the four transition rates. The black line indicates the expectation value, the grey shaded area the 1-sigma interval.

4.6.11 Observed natural linewidth: Beamline contribution

A central part of the above analysis focused on the determination of the natural linewidth. A Voigt model given by

$$Y(E) = \int L_{ion}(\tau)\, G(E-\tau)\, d\tau \tag{83}$$

has been used to extract the natural linewidth from the de-convoluted Lorentzian L_{ion} profile. All broadening effects as well the instrument profile, which has been assumed as gaussian-shaped, has been combined into one Gaussian model G. However, it has been shown in the dissertation of Steffen Kühn [43] that the energy profile of the photons of

Table 8: The four transition rates, obtained from the three parameter sets and their respective theoretical prediction are compared. The rates are given in $10^{12}\frac{1}{s}$.

	$A_{\gamma,1}$	$A^{theo}_{\gamma,1}$	$A_{\gamma,2}$	$A^{theo}_{\gamma,2}$	$A_{A,1}$	$A^{theo}_{A,1}$	$A_{A,2}$	$A^{theo}_{A,2}$
Set 1	16.0(8.7)	-	12.8(6.9)	-	21.9(9.8)	-	23.0(10.2)	-
Set 2	17.8(9.1)	-	14.7(7.5)	-	19.3(8.9)	-	20.8(9.6)	-
Set 3	17.3(7.3)	10.7	13.8(5.3)	10.3	18.3(6.2)	75.9	20.2(7.5)	115.6

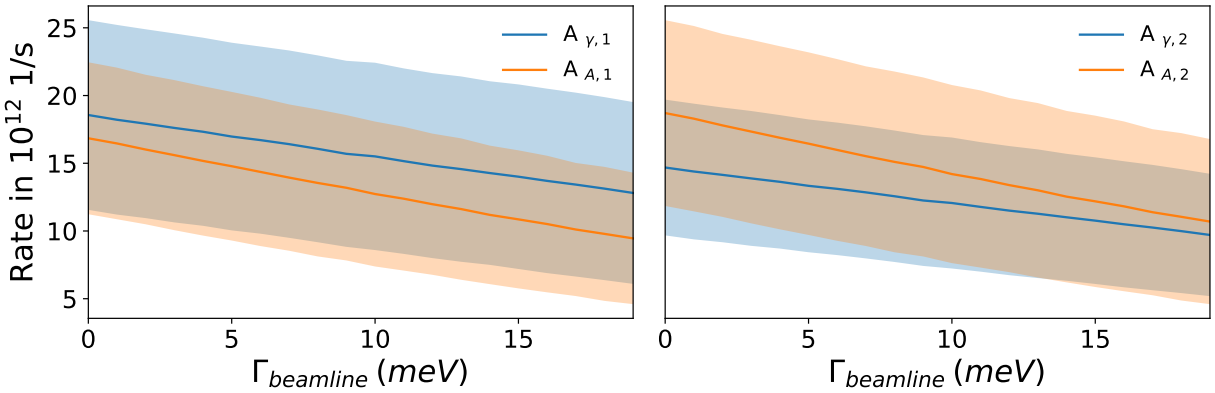

Figure 38: The four absolute transition rates of the two lines of interest have been calculated for varying $\Gamma_{beamline}$.The shaded area indicate the area of 1 sigma uncertainty.

the soft x-ray beamline P04 can be partially modeled by an Lorentzian profile. Following that assumption, equation 84 must be rewritten as

$$Y(E) = \int L_{ion}(\tau) \left(\int L_{beamline}(\tau')\, G(E-\tau')\, d\tau' \right) (E-\tau)\, d\tau, \tag{84}$$

$$Y(E) = \int L_{ion+beamline}(\tau)\, G(E-\tau)\, d\tau. \tag{85}$$

As can be seen, the invariance of Lorentzian profiles under convolution leads to a misassignment of the natural linewidth Γ_{nat} to the experimentally determined linewidth Γ_{exp}, which is in fact given by

$$\Gamma_{exp} = \Gamma_{nat} + \Gamma_{beamline}. \tag{86}$$

One has to conclude, that it is not possible to extract the unbiased natural linewidth Γ_{nat} from the available data. However, the expected impact of $\Gamma_{beamline}$ can be estimated for the four experimentally determined rates.
For that purpose the four rates have been re-calculated for varying $\Gamma_{beamline}$ (see figure 38). While one can see for all four rates a trend changing with $\Gamma_{beamline}$, due to the comparably large uncertainty, this effect can be considered as negligible.

5 Discussion and Outlook

The primary goal of this thesis was the investigation of the M-shell transition array of iron. While few works exist for high charge states of iron with few K and L-shell electrons [20, 54], large scale measurements of iron in medium charge states were hitherto missing. With increasing number of electrons, energy levels start to become more dense, which makes high resolution x-ray sources like the P04 beamline necessary to experimentally resolve all involved lines. Similar difficulties arise in the theoretical treatment. The sheer number of electrons introduce strong electron correlation and thus high sensitivity to the number of configurations included in the calculation.
Despite all difficulties, the iron M-shell UTA is used as diagnostic tool for various astrophysical plasma. The plasma models used for the analysis heavily rely on the results of modern atomic structure codes like HULLAC, which is known to be accurate to few tens of $\mathrm{m\AA}$ in the 10-20 Å regime ([32],[55]) (approx. $1\,\mathrm{eV}$ at $800\,\mathrm{eV}$). To exacerbate the situation even more, only few laboratory measurements of M-shell iron ions exist [56].
In order to systematically benchmark theory, an experimentally unexplored charge state of iron, Fe^{13+}, has been chosen for this work. Using the PETRA III synchrotron radiation, 31 transitions of the M-shell UTA have been resonantly excited and observed in both the radiative and autoionization channels. The transition energies of most identified lines have been determined with a statistical uncertainty of few meV already within a few hours of measurement time and are dominated by systematic uncertainties of $\approx 30\,\mathrm{meV}$, caused by the calibration error and the encoder interpolation.
However, a detailed comparison with state-of-the-art atomic structure theory [53] showed a significant constant deviation of approximately $80\,\mathrm{meV}$. Even larger deviations have been observed in the works of Simon et al.[56], where three prominent lines of the UTA complex of Fe^{+14} exhibited deviations of in the order of $100\,\mathrm{meV}$.
Further analysis has been done to determine the absolute transition rates of two resonances (line 19 and 20, see tab 2). These two lines have been recorded with increased photon beam energy resolution, which enabled the determination of their natural linewidths. The natural linewidth for line 19 deviated more than $30\,\mathrm{meV}$, line 20 even more with approximately $60\,\mathrm{meV}$ from their corresponding theoretical prediction. Including the beamline contribution $\Gamma_{\mathrm{beamline}}$ to the observed linewidth would enhance the apparent disparity even more. Since the natural linewidth is directly related to the total transition rate, these significant deviations foreshadow an inaccuracy in the calculated rates.

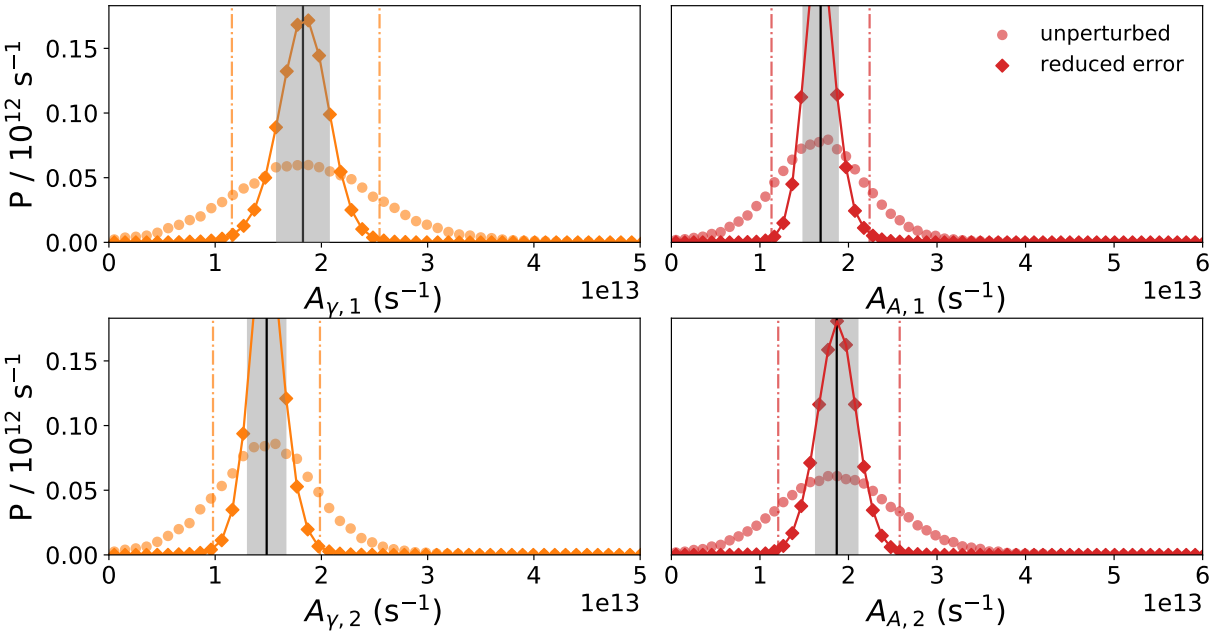

Figure 39: The probability distribution of the four rates $A_{\gamma,1}$, $A_{\gamma,2}$, $A_{A,1}$, $A_{A,2}$ is determined for total transition rates with three-fold decreased errors. For comparison, the probability distributions with unperturbed error are given. The vertical line indicates the expectation value, the shaded area the 1-sigma uncertainty.

To determine absolute rates in this work, it was necessary to use theoretical calculations for the radiative branching ratios. The radiative relaxation of an excited state can occur to various energetically lower states with differing angular momenta and therefore angular distributions. To determine the absolute rates independently of theory, it is necessary to resolve all radiative channels, which was not possible in this work. The error of the radiative branching ratios have been estimated as 5%. The four transition rates have been determined with a approximately 30% to 40% uncertainty. An error analysis showed that the uncertainty of the total transition rates are most influential parameters. The result of a potential three-fold reduction is visualized in figure 39. A reduction of the uncertainties of parameter c and d did not show such strong influence on the final uncertainty. A comparison with the calculations of Gu [53] exhibit a good agreement in the radiative rates, however a significant deviation can be observed in the autoionization rates (see table 8). The calculations of Gu predict autoionization rates deviating more than 10 times the experimental uncertainty. This apparent disparity leads to the assumption that the autoionization channel might be posing a difficulty in the atomic

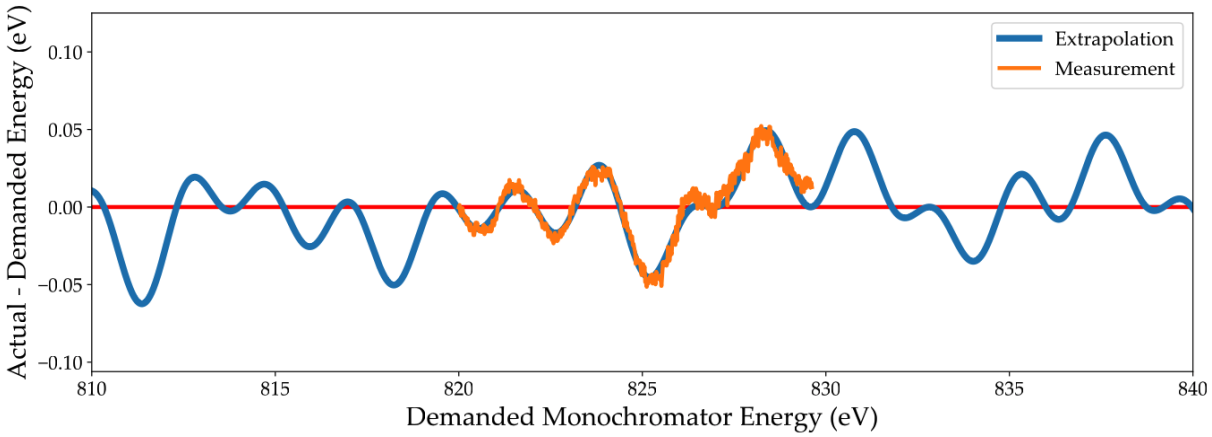

Figure 40: ASPHERE is used to trace the energy difference between the actual and the demanded monochromator energy (orange). By modeling the raw data (orange), an extrapolation (blue) can be acquired. Figure adopted from [43].

structure calculations.

In this work three well known transitions have been used to calibrate the monochromator energy. Since it was expected that the relative calibration of the P04 beamline is linear across the energy range between $700\,\mathrm{eV}$ and $900\,\mathrm{eV}$, a linear calibration curve was applied. For further reduction of uncertainty due to calibration, adding more lines of simple systems (H-like and He-like ions) in the range of $800\,\mathrm{eV}$ is necessary. Suitable transitions are Ly$\alpha_{1,2}$ and w of fluorine at 827.2, 827.5 and $737.3\,\mathrm{eV}$ respectively. By measuring these calibration lines regularly in between UTA measurements, it can be expected that the uncertainty due to the energy calibration is significantly reduced and only dominated by the interpolation error of the encoder. It has been shown that the encoder interpolation error can be traced using a photoelectron spectrometer like ASPHERE[57]. The PolarX-EBIT allows such a set-up to be installed in series due to its transparent main-axis design. With such a simultaneous operation of EBIT and ASPHERE, relative changes in photon energy can be recorded by the photoelectron spectrometer while HCIs, produced and stored in the EBIT, offer an unique absolute calibration in the order of $dE/E = 10^{-7}$. Such a dedicated measurement campaign for more precise determination of UTA transition energies of several iron charge states would certainly be an important contribution to the astrophysics and atomic structure theory community.

Regarding the absolute transition rates, the accuracy of the determined rates were lim-

ited by statistics. As can be seen in figure 39, a decreased uncertainty of the natural linewidth can lead to a major improvement in the final accuracy of the rates. For future measurement campaigns, one has to gain control of the Lorentzian contribution to the instrumental profile. This can be utilized by measuring the above mentioned calibration lines with the same settings as the UTA lines. Since the natural linewidth is few orders of magnitude smaller for these system due to the missing Auger-decay channel, they can be used to model the instrument profile of the photon beamline. Another limiting factor is the radiative branching ratio. In principle, the radiative branching ratio can be determined from observing the photon distribution [51]. However this approach necessitates a linear polarisation of the incident photons, which is not available at the P04 beamline. The radiative branching ratio can be also obtained by resolving the different energies of the fluorescence photons with a high resolution x-ray detector, e.g. a microcalorimeter.

There are new proposals for synchrotron experiments, as well as EBIT equipped with microcalorimeter experiments planned to investigate and deepen our understanding of the astrophysically relevant M-shell UTA.

6 Appendix

6.1 Line identification

In order to save space in the main text (section 4.5), the remaining spectra are provided in this section.

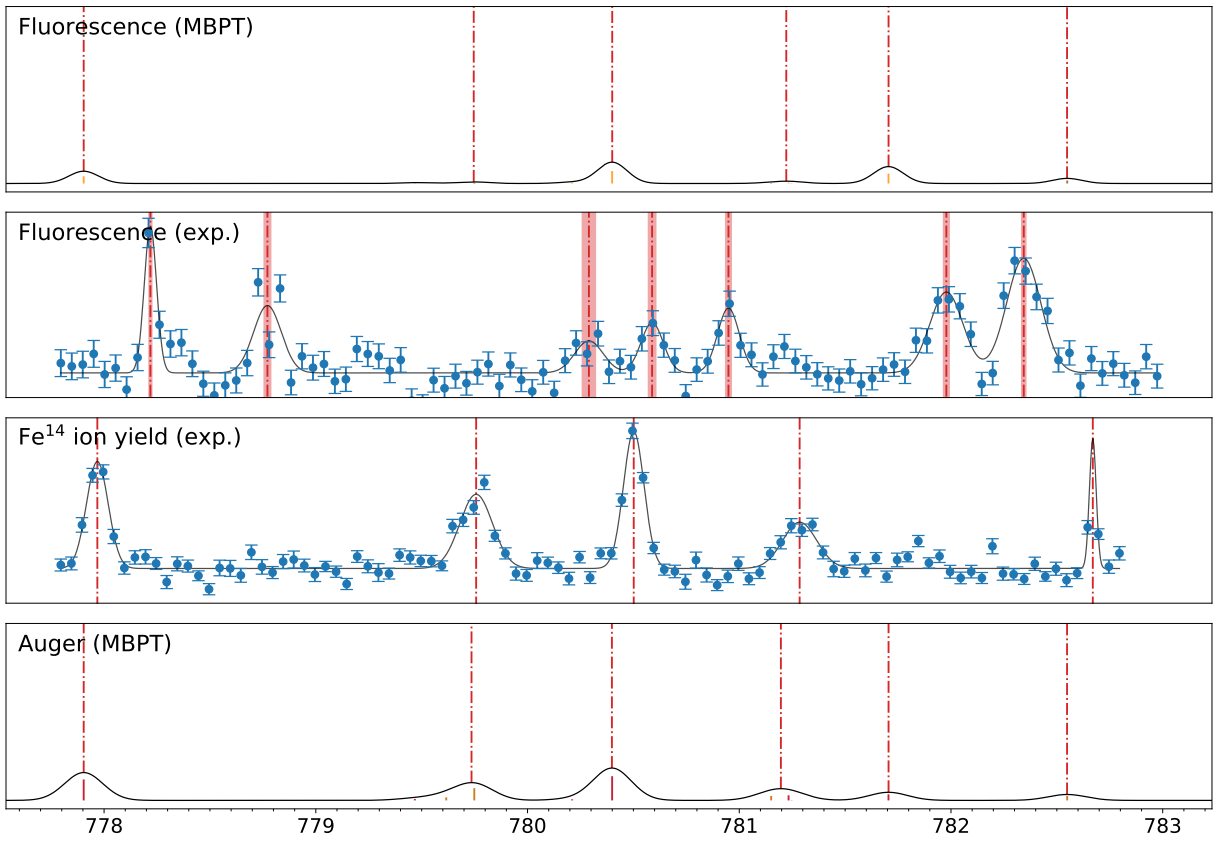

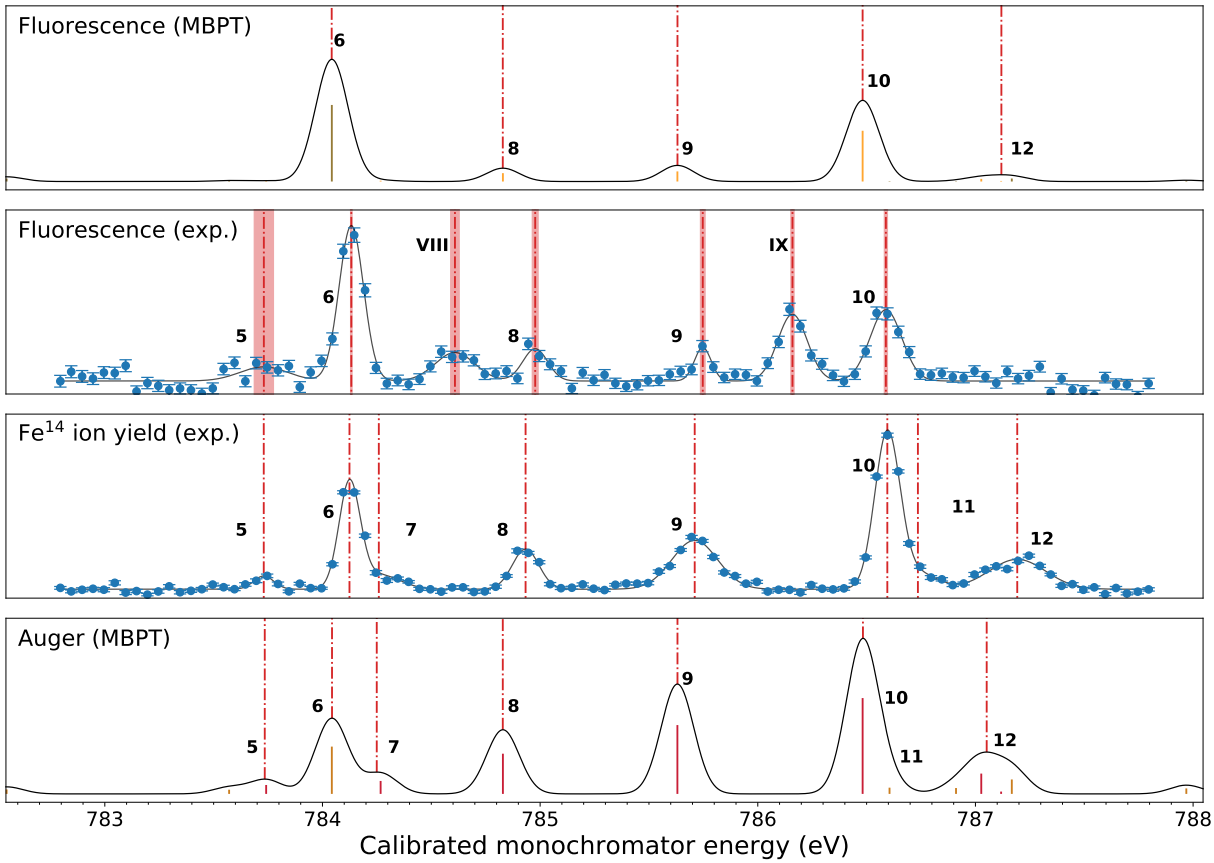
Fluorescence (MBPT)
6
8
9
10
12
Fluorescence (exp.)
5
6
VIII
8
9
IX
10
Fe14 ion yield (exp.)
5
6
7
8
9
10
11
12
Auger (MBPT)
5
6
7
8
9
10
11
12
783
784
785
786
787
788
Calibrated monochromator energy (eV)

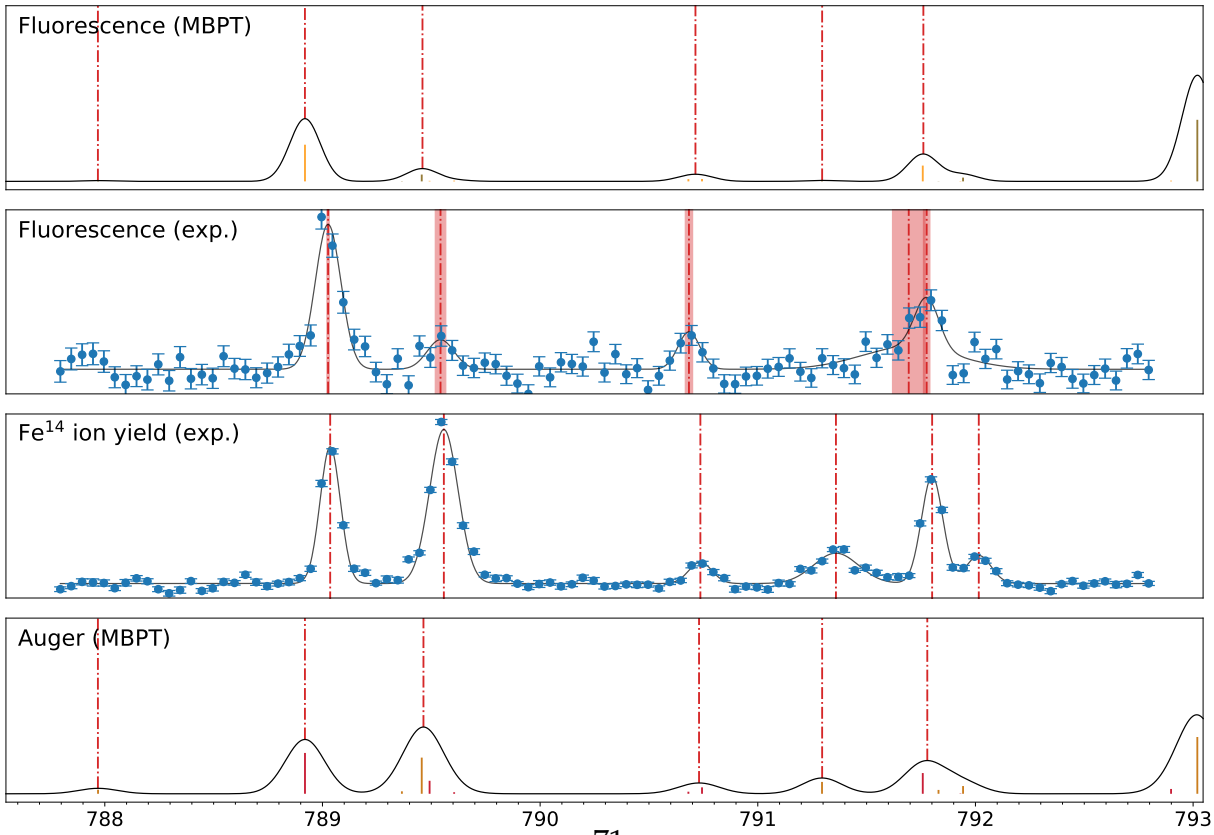
Fluorescence (MBPT)
Fluorescence (exp.)
Fe14 ion yield (exp.)
Auger (MBPT)
788
789
790
791
792
793

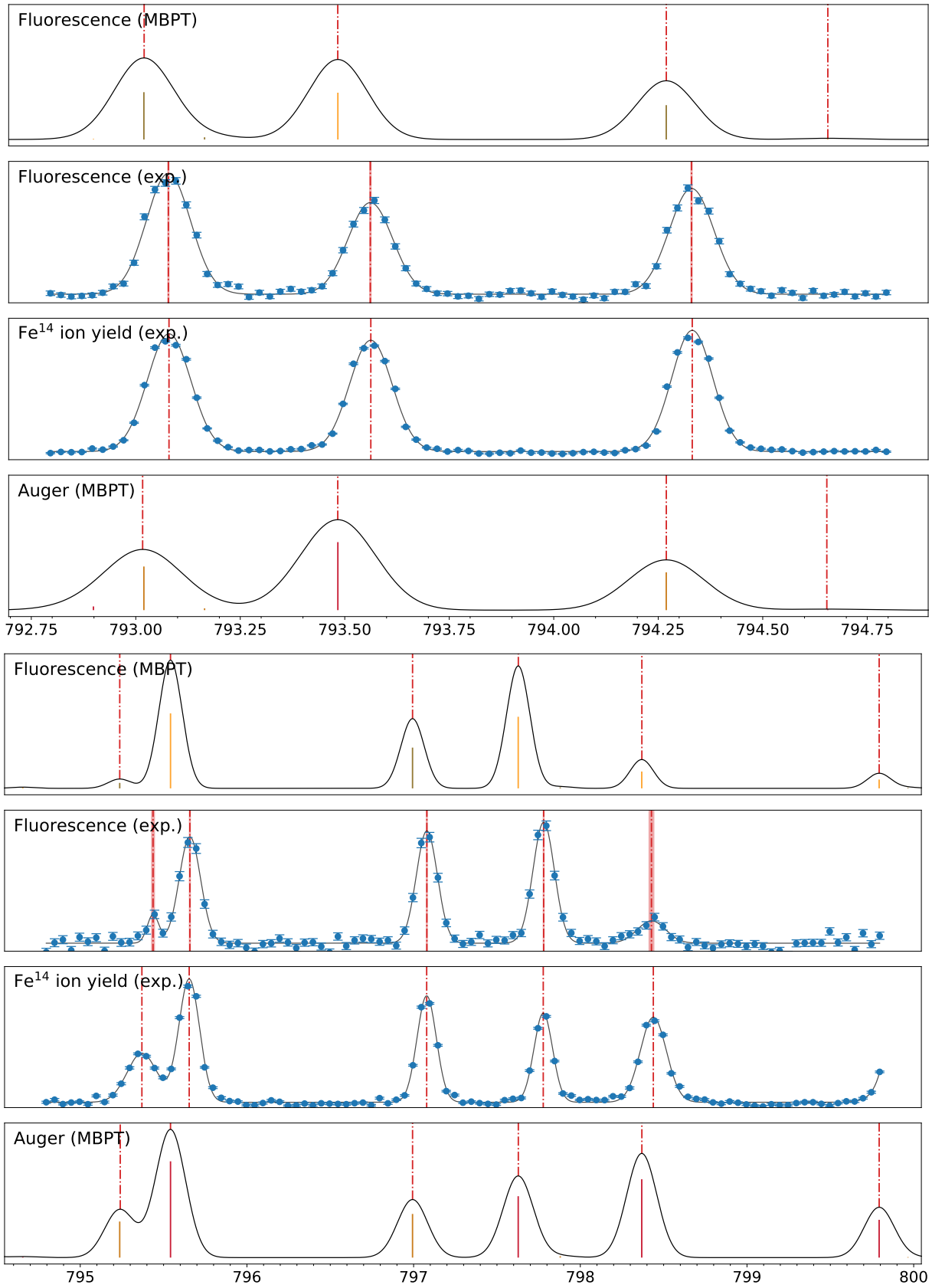
Fluorescence (MBPT)
Fluorescence (exp.)
Fe14 ion yield (exp.)
Auger (MBPT)
792.75
793.00
793.25
793.50
793.75
794.00
794.25
794.50
794.75
Fluorescence (MBPT)
Fluorescence (exp.)
Fe14 ion yield (exp.)
Auger (MBPT)
795
796
797
798
799
800

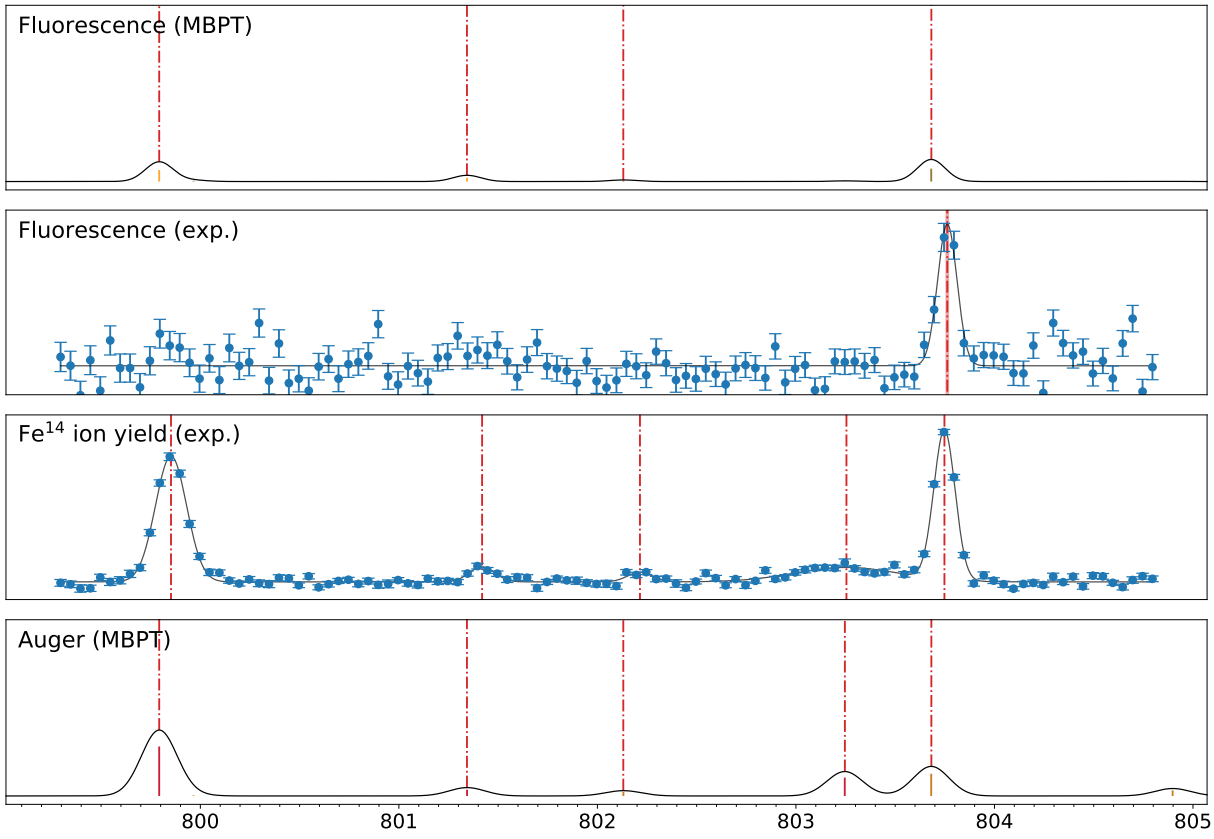
Fluorescence (MBPT)
Fluorescence (exp.)
Fe^{14} ion yield (exp.)
Auger (MBPT)
800
801
802
803
804
805

6.2 Theory

The results of the relativistic many-body-perturbation calculations of Gu [53] are tabulated below. The columns are as follows:
$\mathbf{i_0}$: lower level index
(GRD: $3s^2\ 3p\ \ ^2P_{1/2}$, META: $3s^2\ 3p\ \ ^2P_{3/2}$),
$\mathbf{i_1}$: upper level index,
$\mathbf{s_1}$: upper level label in LS coupling,
$\mathbf{p_1}$: upper level parity,
$\mathbf{j_1}$: $2 \cdot \mathrm{J}$ of the upper level,
E: transition energy in eV,
W: HWHM of the line in eV,
gf: weighted oscillator strength of the transition,
$\mathbf{B_{rad}}$: radiative branching ratio.

i_0	s_1	p_1	j_1	E	S	W	gf	B_{rad}
GRD	2s(2).2p(5)_2P.3s_3P.3p(3)2D3_4D	1	1	7.532958E+02	4.2784E-05	2.0450E-02	7.0975E-03	1.2056E-02
GRD	2s(2).2p(5)_2P.3s_1P.3p(3)2D3_2D	1	3	7.566789E+02	4.3402E-05	2.2099E-02	6.2870E-03	1.3807E-02
GRD	2s(2).2p(5)_2P.3s_3P.3p(3)2P1_4D	1	3	7.604409E+02	6.4795E-05	1.9355E-02	7.5295E-03	1.7211E-02
GRD	2s(2).2p(5)_2P.3s_3P.3p(3)2D3_2P	1	1	7.639885E+02	1.3970E-04	5.8428E-02	3.0212E-02	9.2479E-03
GRD	2s(2).2p(5)_2P.3s_3P.3p(3)2P1_4P	1	1	7.660293E+02	4.7087E-05	7.1823E-02	8.9980E-03	1.0466E-02
GRD	2s(2).2p(5)_2P.3s_1P.3p(3)2D3_2D	1	3	7.723709E+02	8.5214E-05	1.2822E-01	4.0802E-02	4.1770E-03
GRD	2s(2).2p(5)_2P.3s_1P.3p(3)2P1_2S	1	1	7.738536E+02	5.6204E-05	4.9314E-02	1.0230E-02	1.0988E-02
GRD	2s(2).2p(5)_2P.3s_3P.3p(3)4S3_2P	1	1	7.756633E+02	6.3722E-05	7.1876E-02	1.8820E-02	6.7719E-03
GRD	2s(2).2p(5)_2P.3s(2).3p_3P.3d_4F	1	3	7.763307E+02	2.8839E-03	3.7138E-02	1.6054E-01	3.5927E-02
GRD	2s(2).2p(5)_2P.3s(2).3p_1D.3d_2S	1	1	7.796160E+02	4.6598E-05	1.7830E-01	2.2156E-02	4.2063E-03
GRD	2s(2).2p(5)_2P.3s(2).3p_3D.3d_4F	1	3	7.797486E+02	3.3215E-04	1.1587E-01	8.9520E-02	7.4208E-03
GRD	2s(2).2p(5)_2P.3s_3P.3p(3)4S3_4P	1	1	7.811507E+02	1.4910E-04	6.9409E-02	3.2787E-02	9.0952E-03
GRD	2s(2).2p(5)_2P.3s(2).3p_1D.3d_2D	1	3	7.825488E+02	1.0973E-03	9.5459E-03	3.4567E-02	6.3485E-02
GRD	2s(2).2p(5)_2P.3s(2).3p_3S.3d_2D	1	3	7.835711E+02	2.3193E-04	4.7295E-02	3.1067E-02	1.4931E-02
GRD	2s(2).2p(5)_2P.3s(2).3p_1D.3d_2P	1	1	7.840430E+02	2.8318E-02	3.1697E-02	4.0296E-01	1.4055E-01
GRD	2s(2).2p(5)_2P.3s_3P.3p(3)2P1_2D	1	3	7.866053E+02	1.4344E-04	1.4567E-01	4.5932E-02	6.2457E-03
GRD	2s(2).2p(5)_2P.3s_3P.3p(3)4S3_2P	1	1	7.869108E+02	1.2549E-04	1.4890E-01	4.3303E-02	5.7959E-03
GRD	2s(2).2p(5)_2P.3s_3P.3p(3)2D3_2D	1	3	7.871671E+02	1.1090E-03	1.0505E-01	1.0793E-01	2.0549E-02
GRD	2s(2).2p(5)_2P.3s_3P.3p(3)4S3_2P	1	3	7.879689E+02	2.9683E-04	1.9191E-01	4.0656E-02	1.4602E-02
GRD	2s(2).2p(5)_2P.3s(2).3p_3P.3d_4P	1	1	7.893650E+02	1.5676E-04	1.5804E-01	2.4186E-02	1.2963E-02
GRD	2s(2).2p(5)_2P.3s(2).3p_3D.3d_4F	1	3	7.894561E+02	4.3153E-03	9.0887E-02	3.6129E-01	2.3888E-02
GRD	2s(2).2p(5)_2P.3s(2).3p_3D.3d_4D	1	3	7.912951E+02	3.6095E-04	1.7494E-01	1.1642E-01	6.2010E-03
GRD	2s(2).2p(5)_2P.3s_3P.3p(3)2P1_2S	1	1	7.918303E+02	1.0177E-04	3.2465E-01	3.7771E-02	5.3887E-03
GRD	2s(2).2p(5)_2P.3s(2).3p_1P.3d_2P	1	3	7.919431E+02	2.3866E-03	1.6179E-02	8.0166E-02	5.9540E-02
GRD	2s(2).2p(5)_2P.3s(2).3p_3P.3d_2D	1	3	7.930194E+02	3.8938E-02	2.8511E-02	6.3139E-01	1.2334E-01

i_0	s_1	p_1	j_1	E	S	W	gf	B_{rad}
GRD	2s(2).2p(5)_2P.3s(2).3p_3P.3d_4D	1	1	7.931646E+02	1.8317E-03	6.0056E-03	2.6253E-02	1.3954E-01
GRD	2s(2).2p(5)_2P.3s(2).3p_3D.3d_4F	1	3	7.942692E+02	2.8276E-02	2.8778E-02	5.3619E-01	1.0547E-01
GRD	2s(2).2p(5)_2P.3s(2).3p_3D.3d_2D	1	3	7.952368E+02	4.5115E-03	1.4982E-01	4.6780E-01	1.9288E-02
GRD	2s(2).2p(5)_2P.3s(2).3p_1P.3d_2P	1	1	7.969935E+02	3.3642E-02	5.8917E-02	6.2271E-01	1.0805E-01
GRD	2s(2).2p(5)_2P.3s(2).3p_1D.3d_2P	1	3	7.978797E+02	8.8154E-04	7.5165E-02	1.9214E-02	9.1759E-02
GRD	2s(2).2p(5)_2P.3s(2).3p_3D.3d_2S	1	1	7.999656E+02	4.7814E-04	6.7883E-02	7.2759E-03	1.3143E-01
GRD	2s(2).2p(5)_2P.3s(2).3p_3P.3d_2D	1	3	8.021310E+02	5.8705E-04	1.0675E-01	3.9942E-02	2.9395E-02
GRD	2s(2).2p(5)_2P.3s(2).3p_3D.3d_2P	1	1	8.036815E+02	8.1340E-03	4.8272E-02	2.3232E-01	7.0025E-02
GRD	2s(2).2p(5)_2P.3s(2).3p_1S.3d_2D	1	3	8.048976E+02	6.3356E-05	4.4536E-01	5.4650E-02	2.3186E-03
GRD	2s_2S.2p(6).3s(2).3p(2)3P2_2P	1	1	8.626888E+02	1.9973E-03	1.3921E-01	1.7509E-01	2.2815E-02
GRD	2s(2).2p(5)_2P.3s_1P.3p_2D.3d(2)3P2_4D	1	1	8.631339E+02	6.3163E-04	4.2139E-02	1.9241E-02	6.5656E-02
GRD	2s(2).2p(5)_2P.3s_1P.3p_2P.3d(2)3F2_4F	1	3	8.632129E+02	1.3203E-04	6.1368E-02	1.2531E-02	2.1072E-02
GRD	2s_2S.2p(6).3s(2).3p(2)1D2_2D	1	3	8.634425E+02	1.5090E-03	1.2623E-01	1.8806E-01	1.6048E-02
GRD	2s(2).2p(5)_2P.3s_3P.3p_2D.3d(2)3P2_4P	1	3	8.636350E+02	7.4644E-05	8.0835E-02	7.3807E-03	2.0227E-02
GRD	2s_2S.2p(6).3s(2).3p(2)3P2_2P	1	3	8.655779E+02	9.6784E-05	1.4007E-01	1.1421E-02	1.6949E-02
GRD	2s_2S.2p(6).3s(2).3p(2)1S0_2S	1	1	8.703815E+02	4.2409E-05	1.3784E-01	9.2305E-03	9.1889E-03
META	2s(2).2p(5)_2P.3s_3P.3p(3)2P1_4D	1	5	7.577898E+02	6.8994E-05	8.7716E-03	8.7511E-03	3.1536E-02
META	2s(2).2p(5)_2P.3s_3P.3p(3)2D3_4F	1	3	7.625098E+02	6.0734E-05	6.1682E-02	3.2222E-02	7.5395E-03
META	2s(2).2p(5)_2P.3s_3P.3p(3)2P1_4P	1	1	7.636912E+02	9.3192E-05	7.1823E-02	3.5617E-02	1.0466E-02
META	2s(2).2p(5)_2P.3s(2).3p_3S.3d_4D	1	5	7.671377E+02	1.3336E-04	1.3384E-02	1.7401E-02	3.0655E-02
META	2s(2).2p(5)_2P.3s(2).3p_3D.3d_4G	1	5	7.704656E+02	8.4902E-05	6.3884E-03	5.3516E-03	6.3459E-02
META	2s(2).2p(5)_2P.3s_3P.3p(3)2P1_2D	1	5	7.735902E+02	1.9543E-04	1.2245E-01	1.3788E-01	5.6695E-03
META	2s(2).2p(5)_2P.3s_3P.3p(3)2D3_2F	1	5	7.739884E+02	3.2964E-04	1.6156E-02	4.4477E-02	2.9646E-02
META	2s(2).2p(5)_2P.3s(2).3p_3P.3d_4F	1	3	7.739925E+02	3.6077E-04	3.7138E-02	4.0167E-02	3.5927E-02
META	2s(2).2p(5)_2P.3s(2).3p_3D.3d_4S	1	3	7.755056E+02	9.5112E-05	3.1872E-02	2.5728E-02	1.4787E-02

i_0	s_1	p_1	j_1	E	S	W	gf	B_{rad}
META	2s(2).2p(5)_2P.3s(2).3p_3P.3d_4D	1	5	7.762844E+02	3.9938E-04	1.9733E-02	5.6926E-02	2.8063E-02
META	2s(2).2p(5)_2P.3s(2).3p_3D.3d_4D	1	5	7.779037E+02	1.3196E-03	2.7740E-02	1.5752E-01	3.3509E-02
META	2s(2).2p(5)_2P.3s(2).3p_1D.3d_2F	1	5	7.794676E+02	9.3798E-05	1.1202E-02	1.0671E-02	3.5159E-02
META	2s(2).2p(5)_2P.3s(2).3p_1D.3d_2D	1	3	7.802107E+02	1.3925E-04	9.5459E-03	8.7737E-03	6.3485E-02
META	2s(2).2p(5)_2P.3s(2).3p_3P.3d_4D	1	5	7.803996E+02	2.2867E-03	2.0768E-02	1.8515E-01	4.9402E-02
META	2s(2).2p(5)_2P.3s(2).3p_3S.3d_2D	1	3	7.812329E+02	1.4074E-04	4.7295E-02	3.7705E-02	1.4931E-02
META	2s(2).2p(5)_2P.3s(2).3p_3D.3d_4G	1	5	7.812472E+02	7.0611E-05	4.0583E-03	1.8895E-03	1.4948E-01
META	2s(2).2p(5)_2P.3s(2).3p_1D.3d_2P	1	1	7.817048E+02	1.8142E-03	3.1697E-02	5.1632E-02	1.4055E-01
META	2s(2).2p(5)_2P.3s(2).3p_3P.3d_4P	1	1	7.837413E+02	8.4647E-05	2.0056E-01	6.5576E-02	5.1633E-03
META	2s(2).2p(5)_2P.3s_3P.3p(3)2P1_2D	1	3	7.842672E+02	1.4900E-04	1.4567E-01	9.5427E-02	6.2457E-03
META	2s(2).2p(5)_2P.3s_3P.3p(3)2D3_2D	1	3	7.848290E+02	1.5439E-03	1.0505E-01	3.0053E-01	2.0549E-02
META	2s(2).2p(5)_2P.3s_3P.3p(3)4S3_2P	1	3	7.856307E+02	1.8668E-03	1.9191E-01	5.1139E-01	1.4602E-02
META	2s(2).2p(5)_2P.3s(2).3p_1P.3d_2D	1	5	7.864817E+02	9.3861E-03	5.1337E-02	7.3921E-01	5.0790E-02
META	2s(2).2p(5)_2P.3s(2).3p_3P.3d_4P	1	1	7.870268E+02	4.8837E-04	1.5804E-01	1.5070E-01	1.2963E-02
META	2s(2).2p(5)_2P.3s(2).3p_3D.3d_4F	1	3	7.871180E+02	1.0396E-04	9.0887E-02	1.7408E-02	2.3888E-02
META	2s(2).2p(5)_2P.3s(2).3p_3P.3d_2D	1	5	7.889197E+02	1.1599E-02	1.7540E-02	4.4457E-01	1.0436E-01
META	2s(2).2p(5)_2P.3s_3P.3p(3)2P1_2S	1	1	7.894922E+02	1.7164E-04	3.2465E-01	1.2741E-01	5.3887E-03
META	2s(2).2p(5)_2P.3s(2).3p_1P.3d_2P	1	3	7.896050E+02	2.3757E-04	1.6179E-02	1.5960E-02	5.9540E-02
META	2s(2).2p(5)_2P.3s(2).3p_3P.3d_2D	1	3	7.906812E+02	7.1215E-04	2.8511E-02	2.3095E-02	1.2334E-01
META	2s(2).2p(5)_2P.3s(2).3p_1D.3d_2F	1	5	7.907438E+02	7.4810E-04	1.5549E-02	6.5558E-02	4.5645E-02
META	2s(2).2p(5)_2P.3s(2).3p_3P.3d_4P	1	5	7.917580E+02	4.9947E-03	1.3973E-02	2.2208E-01	8.9961E-02
META	2s(2).2p(5)_2P.3s(2).3p_3D.3d_4F	1	3	7.919310E+02	9.5612E-05	2.8778E-02	3.6261E-03	1.0547E-01
META	2s(2).2p(5)_2P.3s(2).3p_3D.3d_2D	1	3	7.928987E+02	2.3132E-04	1.4982E-01	4.7972E-02	1.9288E-02
META	2s(2).2p(5)_2P.3s(2).3p_1D.3d_2D	1	5	7.934835E+02	1.9255E-02	4.1441E-02	9.3979E-01	8.1956E-02
META	2s(2).2p(5)_2P.3s(2).3p_1P.3d_2P	1	1	7.946554E+02	2.9796E-04	5.8917E-02	1.1031E-02	1.0805E-01

i_0	s_1	p_1	j_1	E	S	W	gf	B_{rad}
META	.2s(2).2p(5)_2P.3s(2).3p_1D.3d_2P	1	3	7.955416E+02	3.0940E-02	7.5165E-02	1.3488E+00	9.1759E-02
META	2s(2).2p(5)_2P.3s(2).3p_3D.3d_2S	1	1	7.976275E+02	2.9545E-02	6.7883E-02	8.9918E-01	1.3143E-01
META	2s(2).2p(5)_2P.3s(2).3p_1S.3d_2D	1	5	7.983686E+02	6.9523E-03	1.3768E-01	1.0246E+00	2.7143E-02
META	2s(2).2p(5)_2P.3s(2).3p_3P.3d_2D	1	3	7.997928E+02	3.6389E-03	1.0675E-01	4.9517E-01	2.9395E-02
META	2s(2).2p(5)_2P.3s(2).3p_3D.3d_2P	1	1	8.013434E+02	1.1501E-03	4.8272E-02	6.5698E-02	7.0025E-02
META	2s(2).2p(5)_2P.3s(2).3p_1S.3d_2D	1	5	8.032460E+02	1.2761E-04	4.9102E-01	1.7894E-01	2.8526E-03
META	2s_2S.2p(6).3s(2).3p(2)3P2_2P	1	1	8.603507E+02	3.5711E-04	1.3921E-01	6.2609E-02	2.2815E-02
META	2s(2).2p(5)_2P.3s_1P.3p_2D.3d(2)3P2_4D	1	1	8.607957E+02	9.1718E-05	4.2139E-02	5.5878E-03	6.5656E-02
META	2s(2).2p(5)_2P.3s_1P.3p_2P.3d(2)3F2_4F	1	3	8.608747E+02	5.1112E-05	6.1368E-02	9.7024E-03	2.1072E-02
META	2s_2S.2p(6).3s(2).3p(2)1D2_2D	1	3	8.611044E+02	4.2278E-04	1.2623E-01	1.0538E-01	1.6048E-02
META	2s_2S.2p(6).3s(2).3p(2)1D2_2D	1	5	8.623848E+02	1.1816E-03	1.2604E-01	3.7490E-01	1.2607E-02
META	2s_2S.2p(6).3s(2).3p(2)3P2_2P	1	3	8.632397E+02	1.5965E-03	1.4007E-01	3.7677E-01	1.6949E-02
META	2s_2S.2p(6).3s(2).3p(2)1S0_2S	1	1	8.680434E+02	1.7296E-04	1.3784E-01	7.5292E-02	9.1889E-03

References

[1] Joseph Fraunhofer. Bestimmung des brechungs-und des farbenzerstreungs-vermögens verschiedener glasarten, in bezug auf die vervollkommnung achromatischer fernröhre. *Annalen der Physik*, 56(7):264–313, 1817.

[2] G Kirchhoff and R Bunsen. Xlii. chemical analysis by spectrum-observations.—second memoir. *The London, Edinburgh, and Dublin Philosophical Magazine and Journal of Science*, 22(148):329–349, 1861.

[3] J D Gillaspy. Highly charged ions. *Journal of Physics B: Atomic, Molecular and Optical Physics*, 34(19):R93–R130, sep 2001.

[4] Jansen, F., Lumb, D., Altieri, B., Clavel, J., Ehle, M., Erd, C., Gabriel, C., Guainazzi, M., Gondoin, P., Much, R., Munoz, R., Santos, M., Schartel, N., Texier, D., and Vacanti, G. Xmm-newton observatory* - i. the spacecraft and operations. *A&A*, 365(1):L1–L6, 2001.

[5] Frederik B.S. Paerels and Steven M. Kahn. High-resolution x-ray spectroscopy with chandra and xmm-newton. *Annual Review of Astronomy and Astrophysics*, 41(1):291–342, 2003.

[6] Martin C. Weisskopf, Harvey D. Tananbaum, Leon P. Van Speybroeck, and Stephen L. O'Dell. Chandra X-ray Observatory (CXO): overview. In Joachim E. Truemper and Bernd Aschenbach, editors, *X-Ray Optics, Instruments, and Missions III*, volume 4012, pages 2 – 16. International Society for Optics and Photonics, SPIE, 2000.

[7] AJ Blustin, G Branduardi-Raymont, E Behar, JS Kaastra, SM Kahn, MJ Page, M Sako, and KC Steenbrugge. Multi-wavelength study of the seyfert 1 galaxy ngc 3783 with xmm-newton. *Astronomy & Astrophysics*, 392(2):453–467, 2002.

[8] María H. Sarmiento, María Arévalo, Christophe Arviset, Deborah Baines, Elena Colomo, Nora Loiseau, Bruno Merin, and Jesús Salgado. XMM-Newton Science Archive (XSA). In Marco Molinaro, Keith Shortridge, and Fabio Pasian, editors, *Astronomical Data Analysis Software and Systems XXVI*, volume 521 of *Astronomical Society of the Pacific Conference Series*, page 104, October 2019.

[9] David Heiserman. *Exploring chemical elements and their compounds*. McGraw-Hill, 1991.

[10] J. D. Gillaspy, T. Lin, L. Tedesco, J. N. Tan, J. M. Pomeroy, J. M. Laming, N. Brickhouse, G.-X. Chen, and E. Silver. Fe XVII x-RAY LINE RATIOS FOR ACCURATE ASTROPHYSICAL PLASMA DIAGNOSTICS. *The Astrophysical Journal*, 728(2):132, jan 2011.

[11] S. Bernitt, G. V. Brown, J. K. Rudolph, R. Steinbrügge, A. Graf, M. Leutenegger, S. W. Epp, S. Eberle, K. Kubiček, V. Mäckel, M. C. Simon, E. Träbert, E. W. Magee, C. Beilmann, N. Hell, S. Schippers, A. Müller, S. M. Kahn, A. Surzhykov, Z. Harman, C. H. Keitel, J. Clementson, F. S. Porter, W. Schlotter, J. J. Turner, J. Ullrich, P. Beiersdorfer, and J. R. Crespo López-Urrutia. An unexpectedly low oscillator strength as the origin of the fe xvii emission problem. *Nature*, 492(7428):225–228, 2012.

[12] Steffen Kühn, Chintan Shah, José R. Crespo López-Urrutia, Keisuke Fujii, René Steinbrügge, Jakob Stierhof, Moto Togawa, Zoltán Harman, Natalia S. Oreshkina, Charles Cheung, Mikhail G. Kozlov, Sergey G. Porsev, Marianna S. Safronova, Julian C. Berengut, Michael Rosner, Matthias Bissinger, Ralf Ballhausen, Natalie Hell, SungNam Park, Moses Chung, Moritz Hoesch, Jörn Seltmann, Andrey S. Surzhykov, Vladimir A. Yerokhin, Jörn Wilms, F. Scott Porter, Thomas Stöhlker, Christoph H. Keitel, Thomas Pfeifer, Gregory V. Brown, Maurice A. Leutenegger, and Sven Bernitt. High resolution photoexcitation measurements exacerbate the long-standing fe xvii oscillator strength problem. *Phys. Rev. Lett.*, 124:225001, Jun 2020.

[13] Ehud Behar, Masao Sako, and Steven M. Kahn. Soft X-Ray Absorption by Fe^{0+} to Fe^{15+} in Active Galactic Nuclei. , 563(2):497–504, December 2001.

[14] Sako, M., Kahn, S. M., Behar, E., Kaastra, J. S., Brinkman, A. C., Boller, Th., Puchnarewicz, E. M., Starling, R., Liedahl, D. A., Clavel, J., and Santos-Lleo, M. Complex resonance absorption structure in the x-ray spectrum of iras 13349+2438 *. *A&A*, 365(1):L168–L173, 2001.

[15] Tomer Holczer, Ehud Behar, and Shai Kaspi. Absorption measure distribution of

the outflow in IRAS 133492438: Direct observation of thermal instability? *The Astrophysical Journal*, 663(2):799–807, jul 2007.

[16] Ming F. Gu, Tomer Holczer, Ehud Behar, and Steven M. Kahn. Inner-shell absorption lines of fevi–fexvi: A many-body perturbation theory approach. *The Astrophysical Journal*, 641(2):1227–1232, apr 2006.

[17] Ming F. Gu. Inner-shell absorption lines of fe vi–fe xvi: A many-body perturbation theory approach.

[18] Natalie Hell, Peter Beiersdorfer, Gregory V Brown, Megan E Eckart, Richard L Kelley, Caroline A Kilbourne, Maurice A Leutenegger, Thomas E Lockard, F Scott Porter, and Jörn Wilms. Highly charged ions in a new era of high resolution x-ray astrophysics. *X-Ray Spectrometry*, 49(1):218–233, 2020.

[19] S. W. Epp, J. R. Crespo López-Urrutia, G. Brenner, V. Mäckel, P. H. Mokler, R. Treusch, M. Kuhlmann, M. V. Yurkov, J. Feldhaus, J. R. Schneider, M. Wellhöfer, M. Martins, W. Wurth, and J. Ullrich. Soft x-ray laser spectroscopy on trapped highly charged ions at flash. *Phys. Rev. Lett.*, 98:183001, May 2007.

[20] J. K. Rudolph, S. Bernitt, S. W. Epp, R. Steinbrügge, C. Beilmann, G. V. Brown, S. Eberle, A. Graf, Z. Harman, N. Hell, M. Leutenegger, A. Müller, K. Schlage, H.-C. Wille, H. Yavaş, J. Ullrich, and J. R. Crespo López-Urrutia. X-ray resonant photoexcitation: Linewidths and energies of $k\alpha$ transitions in highly charged fe ions. *Phys. Rev. Lett.*, 111:103002, Sep 2013.

[21] I. Martinson and L. J. Curtis. Spectroscopic studies of the structure of highly ionised atoms. *Contemporary Physics*, 30(3):173–185, 1989.

[22] Albert Einstein. Strahlungs-Emission und Absorption nach der Quantentheorie. *Deutsche Physikalische Gesellschaft*, 18:318–323, January 1916.

[23] P Auger. The auger effect. *Surface Science*, 48(1):1–8, 1975.

[24] A Zigler, M Givon, E Yarkoni, M Kishinevsky, E Goldberg, B Arad, and M Klapisch. Use of unresolved transition arrays for plasma diagnostics. *Physical Review A*, 35(1):280, 1987.

[25] C Bauche-Arnoult, E Luc-Koenig, J-F Wyart, J-P Geindre, P Audebert, P Monier, J-C Gauthier, and C Chenais-Popovics. Interpretation of the spectra of a laser-irradiated au plasma in the 3.0–4.0-Å range. *Physical Review A*, 33(1):791, 1986.

[26] JF Wyart, C Bauche-Arnoult, E Luc-Koenig, TFR Group, et al. Identification of highly-ionized xenon spectra (xe xxvi through xxxi) excited in the plasma of the tfr tokamak. *Physica Scripta*, 32(2):103, 1985.

[27] P. G. Burkhalter, U. Feldman, and Robert D. Cowan. Transitions in highly ionized sn spectra from a laser-produced plasma∗. *J. Opt. Soc. Am.*, 64(8):1058–1062, Aug 1974.

[28] C. Bauche-Arnoult, J. Bauche, and M. Klapisch. Mean wavelength and spectral width of transition arrays in x-uv atomic spectra. *J. Opt. Soc. Am.*, 68(8):1136–1139, Aug 1978.

[29] J Bauche, C Bauche-Arnoult, and M Klapisch. Unresolved transition arrays. *Physica Scripta*, 37(5):659–663, may 1988.

[30] E. Behar1 J. S. Kaastra2 A. C. Brinkman2 Th. Boller3 E. M. Puchnarewicz4 R. Starling4 D. A. Liedahl5 J. Clavel6 M. Sako1, S. M. Kahn1 and M. Santos-Lleo6. Complex resonance absorption structure in the x-ray spectrum of iras 13349+2438. *Astronomy Astrophysics*, 365(1):L168–L173, january 2001.

[31] A Bar-Shalom, M Klapisch, and J Oreg. Hullac, an integrated computer package for atomic processes in plasmas. *Journal of Quantitative Spectroscopy and Radiative Transfer*, 71(2-6):169–188, 2001.

[32] G. V. Brown, P. Beiersdorfer, D. A. Liedahl, K. Widmann, S. M. Kahn, and E. J. Clothiaux. Laboratory measurements and identification of the fe xviii – xxiv l-shell x-ray line emission. *The Astrophysical Journal Supplement Series*, 140(2):589–607, jun 2002.

[33] Morton A Levine, R E Marrs, J R Henderson, D A Knapp, and Marilyn B Schneider. The electron beam ion trap: A new instrument for atomic physics measurements. *Physica Scripta*, T22:157–163, jan 1988.

[34] Shunsuke Ohtani. The tokyo-ebit 2000. In *AIP Conference Proceedings*, volume 572, pages 84–93. American Institute of Physics, 2001.

[35] ortec. Review of the physics of semiconductor detectors. https://www.ortec-online.com/-/media/ametekortec/other/review_of_the_physics_of_semiconductor_detectors.pdf. Accessed: 2021-05-5.

[36] S. Croft and D.S. Bond. A determination of the fano factor for germanium at 77.4 k from measurements of the energy resolution of a 113 cm3 hpge gamma-ray spectrometer taken over the energy range from 14 to 6129 kev. *International Journal of Radiation Applications and Instrumentation. Part A. Applied Radiation and Isotopes*, 42(11):1009–1014, 1991.

[37] U. Fano. Ionization yield of radiations. ii. the fluctuations of the number of ions. *Phys. Rev.*, 72:26–29, Jul 1947.

[38] U. Fano. On the theory of ionization yield of radiations in different substances. *Phys. Rev.*, 70:44–52, Jul 1946.

[39] Wolfgang Demtröder. *Atoms, molecules and photons*, volume 3. Springer, 2010.

[40] Vsevolod V Balashov, Alexei N Grum-Grzhimailo, and Nikolai M Kabachnik. *Polarization and correlation phenomena in atomic collisions: a practical theory course*. Springer Science & Business Media, 2013.

[41] Anthony Stone. Wigner coefficient calculator. http://www-stone.ch.cam.ac.uk/wigner.shtml.

[42] Patrick Micke, S Kühn, L Buchauer, JR Harries, Thore Mainart Bücking, K Blaum, A Cieluch, A Egl, Daniel Hollain, S Kraemer, et al. The heidelberg compact electron beam ion traps. *Review of Scientific Instruments*, 89(6):063109, 2018.

[43] *High precision soft x-ray transition measurement of neon-like mid-Z ions using ultra monochromatic synchrotron radiation*. PhD thesis.

[44] FastComTec GmbH. Mpa4: Multiparameter multichannel analyzer.

[45] KETEK. Axas-m.

[46] P. Lechner, C. Fiorini, R. Hartmann, J. Kemmer, N. Krause, P. Leutenegger, A. Longoni, H. Soltau, D. Stötter, R. Stötter, L. Strüder, and U. Weber. Silicon drift detectors for high count rate x-ray spectroscopy at room temperature. *Nuclear Instruments and Methods in Physics Research Section A: Accelerators, Spectrometers, Detectors*

and Associated Equipment, 458(1):281–287, 2001. Proc. 11th Inbt. Workshop on Room Temperature Semiconductor X- and Gamma-Ray Detectors and Associated Electronics.

[47] BEHLKE. Fast solid-state switch.

[48] Erich Lohrmann and Paul Söding. *Von schnellen Teilchen und hellem Licht*. John Wiley & Sons, 2009.

[49] R Brandelik, W Braunschweig, K Gather, V Kadansky, K Lübelsmeyer, P Mättig, H-U Martyn, G Peise, J Rimkus, HG Sander, et al. Evidence for planar events in e+ e- annihilation at high energies. *Physics Letters B*, 86(2):243–249, 1979.

[50] Jens Viefhaus, Frank Scholz, Sascha Deinert, Leif Glaser, Markus Ilchen, Jörn Seltmann, Peter Walter, and Frank Siewert. The variable polarization xuv beamline p04 at petra iii: Optics, mechanics and their performance. *Nuclear Instruments and Methods in Physics Research Section A: Accelerators, Spectrometers, Detectors and Associated Equipment*, 710:151–154, 2013. The 4th international workshop on Metrology for X-ray Optics, Mirror Design, and Fabrication.

[51] René Friedrich Steinbrügge. *Bestimmung von absoluten Auger-und radiativen Zerfallsraten K-Schalen-angeregter hochgeladener Eisenionen*. PhD thesis, Ruprecht-Karls-Universität Heidelberg, 2015.

[52] Moto Togawa, Steffen Kühn, Chintan Shah, Pedro Amaro, René Steinbrügge, Jakob Stierhof, Natalie Hell, Marieke Rosner, Keisuke Fujii, Matthias Bissinger, et al. Observation of strong two-electron–one-photon transitions in few-electron ions. *Physical Review A*, 102(5):052831, 2020.

[53] Ming F. Gu. personal communication.

[54] R. Steinbrügge, S. Bernitt, S. W. Epp, J. K. Rudolph, C. Beilmann, H. Bekker, S. Eberle, A. Müller, O. O. Versolato, H.-C. Wille, H. Yavaş, J. Ullrich, and J. R. Crespo López-Urrutia. Absolute measurement of radiative and auger rates of $k-$shell$-$vacancy states in highly charged fe ions. *Phys. Rev. A*, 91:032502, Mar 2015.

[55] M. F. Gu. Wavelengths of 2l→3l′ transitions in l-shell ions of iron and nickel: A combined configuration interaction and many-body perturbation theory approach. *The Astrophysical Journal Supplement Series*, 156(1):105–110, jan 2005.

[56] M. C. Simon, J. R. Crespo López-Urrutia, C. Beilmann, M. Schwarz, Z. Harman, S. W. Epp, B. L. Schmitt, T. M. Baumann, E. Behar, S. Bernitt, R. Follath, R. Ginzel, C. H. Keitel, R. Klawitter, K. Kubiček, V. Mäckel, P. H. Mokler, G. Reichardt, O. Schwarzkopf, and J. Ullrich. Resonant and near-threshold photoionization cross sections of fe^{14+}. *Phys. Rev. Lett.*, 105:183001, Oct 2010.

[57] K Rossnagel, L Kipp, M Skibowski, and S Harm. A high performance angle-resolving electron spectrometer. *Nuclear Instruments and Methods in Physics Research Section A: Accelerators, Spectrometers, Detectors and Associated Equipment*, 467:1485–1488, 2001.

Erklärung

Ich versichere, dass ich diese Arbeit selbstständig verfasst und keine anderen als die angegebenen Quellen und Hilfsmittel benutzt habe.

Heidelberg, den 18. August 2021

Moto Togawa